THÈSE / UNIVERSITÉ DE BRETAGNE OCCIDENTALE
sous le sceau de l'Université Bretagne Loire

pour obtenir le titre de
DOCTEUR DE L'UNIVERSITÉ DE BRETAGNE OCCIDENTALE
Mention : Biologie Santé
École Doctorale SICMA

présentée par

Konstantinos A. Mountris

Préparée au Laboratoire de Traitement de l'Information Médicale, INSERM UMR 1101

Introduction of Monte Carlo Dosimetry and Edema in Inverse Treatment Planning of Prostate Brachytherapy

Thèse soutenue le 5 septembre 2017
devant le jury composé de :

David SARRUT
Directeur de recherche, CREATIS CNRS UMR 5220 / *Rapporteur*

George KAGADIS
Professeur d'université, Université de Patras (Grèce) / *Rapporteur*

Jocelyne TROCCAZ
Directrice de recherche, TIMC-IMAG CNRS UMR 5525 / *Présidente du jury, Examinatrice*

Miguel A. GONZÁLEZ BALLESTER
ICREA Professeur de recherche, SIMBIOsys Université de Pompeu Fabra (Espagne) / *Examinateur*

Dimitris VISVIKIS
Directeur de recherche, LaTIM INSERM UMR 1101 / *Directeur de thèse, Invité*

Julien BERT
Ingénieur de recherche, LaTIM INSERM UMR 1101, CHRU Brest / *Encadrant, Invité*

This page is intentionally left blank

CONTENTS

Page

Abstract **1**

Resumé **3**

1 Background **7**
1.1 The prostate gland . . . 8
1.1.1 Transition zone . . . 8
1.1.2 Central zone . . . 9
1.1.3 Peripheral zone . . . 9
1.1.4 Anterior fibromuscular stroma . . . 9
1.2 Prostate cancer . . . 10
1.2.1 Risk factors . . . 10
1.2.2 Classification . . . 10
1.2.3 Screening and early detection . . . 11
1.2.4 Staging . . . 11
1.3 Prostate cancer treatment . . . 12
1.3.1 Active surveillance . . . 12
1.3.2 Radical prostatectomy . . . 13
1.3.3 Androgen deprivation therapy . . . 13
1.3.4 Chemotherapy . . . 13
1.3.5 External beam radiotherapy . . . 14
1.3.6 Transperineal LDR/HDR brachytherapy . . . 15
1.3.7 Focusing on LDR brachytherapy . . . 18
1.4 LDR brachytherapy limitations . . . 18
1.4.1 TG-43 dose calculation formalism . . . 19
1.4.2 Edema during brachytherapy . . . 21
1.4.3 Inverse treatment planning . . . 22
1.5 Thesis objective statement . . . 25
1.6 Objective de thèse . . . 26

2 Monte Carlo inverse treatment planning algorithm **29**
2.1 Inverse treatment planning algorithm overview . . . 30
2.1.1 GPU-accelerated Monte Carlo dosimetry . . . 31
2.1.2 Brachytherapy seed model in the proposed MC-ITPA . . . 34
2.1.3 Fast simulated annealing in LDR brachytherapy . . . 35
2.2 MC-ITPA development . . . 37
2.2.1 MC-based seed dose map generation . . . 37
2.2.2 Statistical uncertainty effect in MC-ITPA dosimetry . . . 40
2.2.3 Material composition effect in MC-ITPA dosimetry . . . 41
2.2.4 Optimization process . . . 42
2.3 MC-ITPA validation process . . . 50
2.3.1 Patients database for MC-ITPA validation . . . 50
2.3.2 MC-ITPA evaluation . . . 50
2.4 DVH-based inverse planning . . . 60
2.5 MC-Inverse treatment planning algorithm summary . . . 64

3 Edema Biomechanical Modeling **65**
3.1 Edema effect on dosimetry . . . 66
3.2 Inflammation . . . 67
3.2.1 Underlying inflammation mechanism . . . 67
3.2.2 Starling equation . . . 70
3.3 Continuum mechanics . . . 72
3.3.1 Rigid body deformations . . . 73
3.3.2 Elastic body deformations . . . 74
3.3.3 Biphasic mixture theory . . . 76
3.4 Modeling techniques . . . 77
3.4.1 Finite elements method . . . 78
3.4.2 Mesh generation . . . 79
3.5 Proposed model development . . . 81
3.5.1 Patient database . . . 81
3.5.2 Male pelvic region mesh . . . 82
3.5.3 Edema evolution modeling . . . 83
3.5.4 Model validation . . . 86
3.6 Prostate mechanical parameters effect on edema . . . 88
3.6.1 Preliminary test . . . 89
3.6.2 Young modulus effect test . . . 90
3.6.3 Excessive fluid pressure effect test . . . 91
3.7 Edema biomechanical model summary . . . 91

4 Dynamic Monte Carlo dosimetry **93**
4.1 Voxelized image deformation . . . 94
4.1.1 Rasterization . . . 94
4.1.2 Barycentric interpolation . . . 96
4.1.3 Volumetric model resampling . . . 98
4.1.4 CT image resampling . . . 99
4.1.5 Seeds displacement . . . 101

4.2 Dynamic dosimetry scheme . . . 102
4.2.1 MC dose to real dose conversion . . . 102
4.2.2 Dynamic vs Conventional dosimetry . . . 104
4.2.3 Dynamic dosimetry improvements . . . 107
4.3 Adaptive treatment planning . . . 109
4.4 Dynamic Monte Carlo dosimetry summary . . . 111

Discussion **112**

Dissemination **118**

Funding **119**

A ORACLE **121**

B FSA optimization pseudo-code **128**

C Individual patients' dosimetry report **129**

Bibliography **133**

Index **144**

Acronyms **147**

LIST OF FIGURES

1.1 The male reproductive system's anatomy . . . 8
1.2 The prostatic zones . . . 9
1.3 IMRT and VMAT radiotherapy . . . 14
1.4 TRUS template guide . . . 15
1.5 Seeds placement . . . 16
1.6 HDR applicators insertion . . . 17
1.7 HDR after-loader . . . 18
1.8 TG-43 Coordinate system . . . 19
1.9 Energy (cost) function with several minima . . . 24

2.1 GPU architecture . . . 32
2.2 `STM1251` seed model . . . 34
2.3 Pouliot et al., 1996 cost function objectives . . . 36
2.4 Possible seed positions . . . 38
2.5 US image conversion to computational phantom . . . 39
2.6 Cost function objectives . . . 46
2.7 Initial seeds' configuration's cost . . . 48
2.8 Implant cost update by seed swapping . . . 48
2.9 Prostate contour-dose-prescription variation . . . 53
2.10 Prostate uniformity-dose-prescription variation . . . 53
2.11 Urethra contour-dose-prescription variation . . . 54
2.12 Rectum contour-dose-prescription variation . . . 54
2.13 FSA convergence dependence on temperature . . . 55
2.14 FSA convergence dependence on cooling rate . . . 56
2.15 DVH comparison of clinical and MC-ITPA plans. . . . 58
2.16 DVH comparison of DVH-MC-ITPA and standard MC-ITPA plans. . . . 63

3.1 Inflammation mechanism . . . 67
3.2 Exudate formation . . . 68
3.3 Chronic inflammation recursion . . . 70
3.4 Volumetric fluid flux increase . . . 71

3.5 Capillary filtration equilibrium . . . 72
3.6 Deformation map . . . 73
3.7 Rigid motion . . . 74
3.8 Internal body forces . . . 75
3.9 Cauchy stress tensor . . . 75
3.10 Finite elements approximation . . . 79
3.11 Mesh elements . . . 80
3.12 Mesh type . . . 80
3.13 Male pelvic region mesh . . . 82
3.14 Stress-strain diagram . . . 85
3.15 Poisson effect . . . 85
3.16 Edema mean resorption pattern . . . 88
3.17 Poisson's ratio effect . . . 89
3.18 Young modulus effect . . . 89
3.19 Prostate stiffness effect . . . 90
3.20 Excessive fluid pressure effect . . . 91

4.1 Edge function division. . . . 95
4.2 Polygon rasterization . . . 96
4.3 Barycentric coordinates . . . 97
4.4 VMR algorithm preprocessing pipeline . . . 99
4.5 VMR algorithm 3D rasterization . . . 99
4.6 VMR sharp features preservation . . . 100
4.7 Seeds movement during deformation . . . 101
4.8 Isodoses distribution in conventional and dynamic dosimetry . . . 107
4.9 DVH conventional and dynamic dosimetry . . . 108
4.10 Edema prediction in treatment planning . . . 109

A.1 ORACLE data loading . . . 123
A.2 ORACLE template guide setting . . . 124
A.3 ORACLE seeds' and particles' number calculation . . . 124
A.4 ORACLE single-seed dose maps generation . . . 125
A.5 ORACLE Optimization . . . 125
A.6 ORACLE Results evaluation . . . 126

LIST OF TABLES

1.1 International Society of Urological Pathology 2014 grade groups 11
1.2 American Joint Committee on Cancer (AJCC) TNM staging system 12

2.1 Material composition of the various materials present in the heterogeneous computational phantoms 39
2.2 Comparison of the statistical uncertainty in the prostate between the total implant dose map generated by a complete MC simulation and generated by single-seed dose maps accumulation 40
2.3 Simulated particles number effect on the dose metrics. 41
2.4 Effect of the materials' composition on the dose metrics. 42
2.5 AAPM TG-137 planning criteria for prescribed dose (D_{presc}) 145 Gy. 51
2.6 Cost function parameters set-up to achieve the `AAPM TG-137` planning criteria for one patient. 52
2.7 Dosimetric results of a treatment plan generated with cost function parameters as given in Table 2.6 52
2.8 Dose metrics comparison between clinical plans (simulated with MC) and MC-ITPA generated plans. 57
2.9 Dose metrics overestimation by TG43 dosimetric formalism. 59
2.10 Impoved treatment planning with DVH-MC-ITPA. 62
2.11 Used planning schedule for treatment planning with DVH-MC-ITPA. 63

3.1 Average mesh quality criteria for the given patients dataset. 83
3.2 Material properties assigned on the pubic organs of interest. 86
3.3 Prostate elastic properties after model assessment. 87

4.1 Mean relative difference for the dose metrics of interest for the 15 patients dataset between Day1 and conventional/dynamic Day30 dosimetry for the different cases of the Young modulus effect experiment. 105
4.2 Mean relative difference for the dose metrics of interest for the 15 patients dataset between Day1 and conventional/dynamic Day30 dosimetry for the different cases of the Excessive fluid pressure effect experiment. 106

4.3 Adaptation of treatment planning to edema. 110
D.1 Thesis contributions in LDR treatment planning summary. 115

C.1 Dose metrics for the individual plans generated by the standard MC-ITPA for the given patients dataset. 130
C.2 Dose metrics for individual patient treatment plans, generated with the DVH-MC-ITPA. 131

This page is intentionally left blank

Acknowledgments

Preparing a thesis is maybe the most challenging, but almost the most valuable task in the early career of a young researcher. When you decide to start a thesis you are given the chance to explore an immature or even previously unexplored scientific topic of high interest. This creates great excitement but also requires great effort and sacrifice.

You see, as anything new and unexplored in life, a thesis is hard. Is hard to understand, hard to approach, and hard to solve. But you should not be scared of hard. You should fall in love with hard and devote yourself to your purpose and your dream. Through devotion, persistence, and passion you will overcome all the obstacles and misfortunes. You will succeed! And when the journey of your thesis finish, the skills, the knowledge, the experience, and the virtues that you will have acquired will be the proof that hard is beautiful.

Fortunately in this journey, one will not be alone. Me personally, I was lucky to be supported by many brilliant people and I deeply express my gratitude to them for being next to me in this process. First of all I want to thank my supervisors Dr. Julien Bert and Prof. Dimitris Visvikis for the opportunity to work on such an interesting topic and the guidance they provided me by sharing their expertise.

Dr. Bert was always available to discuss my ideas, make helpful suggestions, and guide my progress. Without his expertise and his great support it would not be feasible to complete the amount of the work produced in this thesis.

Prof. Visvikis had a significant role on my progress, too. Other than sharing his expertise and guiding me in this thesis, he also was a mentor to me. He trusted my potential and supported me in my academic choices. Furthermore, he cared to support me in acquiring extra academic skills that are essential for my future career and for this I express to him my gratitude.

Moreover, I had the chance to work in this thesis under the co-direction of Dr. Emmanuel Promayon and Prof. Jocelyne Troccaz. I am grateful to both of them for their support in my work. Even from distance, we always had the chance to discuss my results through tele-conferences and they always provided me with important feedback and guidance. I feel deeply grateful for this collaboration and I can't expect nothing else other than more fruitful collaborations like this one.

My gratitude also goes to Dr. Jérôme Noailly and Prof. Miguel Angel Gonzalez Ballester for accepting me as Visiting Researcher for a period of three months in SIMBIOsys. The skills I acquired next to them assisted me towards achieving my thesis objectives. Their warm welcoming and their tutoring in biomechanics helped me greatly in advancing my work.

I could not forget neither Dr. Alejandro Rodríguez Aguilera for his great support with the understanding of the volumetric resampling algorithm he developed during his Ph.D. and his technical support.

Finally, I can't be more thankful towards my beloved parents Anastasios and Georgia and my beloved sister Theodwra. Being far from them is not easy but you can't never be really far from the people you love, no matter the distance. I am grateful for their continuous support during all my life. I thank you for giving me the guidelines to be the person I am today and always loving me. You are my inspiration to all my achievements.

At last I want say a big thank you to Nathalie for being next to me, being supportive and understanding. You are a great scientist, person, friend, and partner. You deserve all the best. You give me strength and inspiration to be all I dream to be. I am blessed to share our dreams together today and every single tomorrow. Thank You!

To my family. To my partner. To my homeland.

“If you deconstruct Hellas, you will see in the end an olive tree, a grapevine, and a boat remaining. That is, with as much, you reconstruct her."

— Odysseas Elytis

Abstract

Prostate cancer is the second most common cancer in men. Two-thirds of the cases are diagnosed in developed countries and France is ranked third in incidence rate. Low-dose-rate (LDR) brachytherapy is a widely used treatment option. During LDR brachytherapy, radioactive seeds are implanted permanently in the prostate in order to deliver a therapeutic dose locally in the cancerous region while sparing the tissues and organs at risk (OARs). Despite its high success rate (75% to 91%), the side-effects (sexual and urinary problems) remain high.

The dose delivered to the tumor depends on the implantation positions of the seeds, which implies that treatment planning is essential. Clinical inverse planning systems automatically provide optimal implantation positions. However, this prediction is based on a simplified dosimetric model where the human body is considered an infinite volume of water. When tissue heterogeneity is not considered, the expected dose differs from the actual administered dose. The dose received by 90% of the prostate volume (D_{90}) may be overestimated up to 7% and may be associated with malignant recurrence.

Another important factor that induces treatment errors is the occurrence of prostate edema during brachytherapy that involves a volumetric change of the organ. Edema can lead to a significant underestimation of the D_{90}, for example, by 13.6% for a volumetric change of 20%. Moreover, the magnitude of edema varies considerably (10% to 96%) between patients. Today the exact mechanism of edema formation remains unknown. Changes in edema lead to significant uncontrolled degradation of treatment planning and therefore to the actual dose that the patient receives, resulting in overdose of the OARs and increased chance of side-effects.

To solve the first major limit of the treatment planning presented here, namely the calculation of dose, we propose an inverse planning system based on Monte Carlo (MC) dosimetry. GPU-accelerated dosimetry is combined with a fast simulated annealing method. The cost function of the optimization uses directly the dose volume histograms so that the found solution perfectly matches the dosimetric criteria, which is not the case for current systems used in clinical routine. Our method provides precise and automatic prediction of optimal implantation positions according to a personalized dosimetry in clinically compatible time. The treatment plans obtained from the proposed method were evaluated with a database of clinical treatment plans of 18 patients. The method proposed in this thesis makes it possible to obtain a treatment plan in barely a minute, with results that satisfies all the dosimetric criteria of the treatment.

In order to answer the second limit of a precise planning, that related to prostate edema, we propose a biomechanical model based on the finite element method (FEM) in order to estimate the effect of the tissue elastic parameters on the characteristics of the edema. We show that the large variation in edema as well as the varying half-life are correlated with changes in the elastic properties of the prostate. Variations in the characteristics of edema are studied with a database of 15 patients. To account for the impact of edema in dosimetry, we propose a dynamic dosimetry scheme. A prostate volume resampling algorithm allows to consider the volumetric changes associated with edema during the MC dosimetry. Dynamic dosimetry with edema shows consistent results with previous studies in the literature. That is, the underestimation of the dose due to edema. For example, for a magnitude of edema of 20%, the prostate dose D_{90} and the urethra D_{10} are 13.6% and 10.6%, respectively.

To conclude, we propose in this thesis a system of inverse treatment for prostate brachytherapy which takes into account a precise personalization of the dosimetry but also of the edema

of the prostate. This work can also be used in other clinical contexts, such as high-dose-rate brachytherapy, but also be adapted to treat other organs. In the future, our work will focus on the study and the ability to adapt the proposed prostate biomechanical model to each patient using elastic measurements via prostate elastography. Due to the inherent limitations of FEM, the incorporation of the biomechanical model of edema into the treatment planning system is costly in computation time. An alternative method would be to propose a new meshless model to improve the simulation of edema during intraoperative planning.

Resumé

Le cancer de la prostate est le deuxième cancer le plus fréquent chez les hommes. Les deux tiers des cas sont diagnostiqués dans les pays développés et la France occupe le troisième rang du taux d'incidence. La curiethérapie bas-débit dose (LDR) est une option de traitement largement utilisée. Au cours de la curiethérapie LDR, des graines radioactives sont implantées en permanence dans la prostate afin de délivrer une dose thérapeutique de façon locale dans la zone cancéreuse tout en épargnant les tissus et les organes voisins à risque (OAR). Malgré son taux de réussite élevé (75% à 91%), les effets secondaires (problèmes sexuels et urinaires) restent élevés.

La dose délivrée à la tumeur dépend des positions d'implantation des graines, ce qui implique que la planification du traitement est essentiel. Les systèmes cliniques de planification inverse fournissent automatiquement les positions d'implantation optimale. Cependant, cette prédiction est basée sur un modèle dosimétrique simplifié où le corps humain est considéré comme un volume d'eau infini. Lorsque l'hétérogénéité des tissus n'est pas considérée, la dose prévue diffère de la dose administrée réelle. La dose reçue par les 90% du volume de prostate (D_{90}) peut être surestimée jusqu'à 7% et peut être associée à une récidive maligne.

Un autre facteur important qui induit des erreurs de traitement est l'apparition d'un œdème de la prostate pendant par la curiethérapie impliquant un changement volumétrique de l'organe. L'œdème peut entraîner une sous-estimation significative du D_{90} par exemple il de 13.6% pour un changement volumétrique de 20%. De plus, la proportion de cet œdème varie considérablement (10% à 96%) entre les patients. Aujourd'hui le mécanisme exact de l'apparition de cet œdème reste inconnu. Les variations de l'œdème entraînent une dégradation incontrôlée significative de la planification du traitement et donc de la dose réelle donnée au patient entraînant un surdosage des OAR et des effets secondaires.

Pour résoudre la première limite majeures de la planification du traitement présentée ici, à savoir le calcul de dosimétrie, nous proposons un système de planification inverse basé sur une dosimétrie Monte Carlo (MC). Une dosimétrie MC accélérée par GPU est combinée avec une méthode d'optimisation par recuit simulé rapide. La fonction de cout de l'optimisation utilise directement l'histogramme de volume de dose pour que la solution trouvé colle parfaitement aux critères dosimétriques, ce qui n'est aujourd'hui pas le cas avec les systèmes utilisés en routine clinique. Notre méthode fournis une prédiction précise et automatique des positions d'implantation optimale en fonction d'une dosimétriques personnalisées, le tout dans un temps cliniquement compatible. L'évaluation des plans de traitement obtenues on été évaluée avec une base de données de traitements cliniques de 18 patients. La méthode proposée dans cette thèse permet d'obtenir un plan de traitement en à peine une minute, avec des résultats qui satisfait tous les critères dosimétriques du traitement.

Pour répondre à la deuxième limite d'une planification précise, celle liée à l'œdème de la prostate, nous proposons un modèle biomécanique basé sur la méthode des éléments finis (FEM) afin d'estimer l'effet élastiques des tissues qui joue sur les caractéristiques de l'œdème. Nous démontrons que la grande variation de l'œdème ainsi que la demi-vie de dégonflement sont corrélées avec les variations des propriétés élastiques de la prostate. Les variations des caractéristiques de l'œdème sont étudiées via une base de données de 15 patients. Pour tenir compte de l'impact de l'œdème dans la dosimétrie, nous proposons un système dynamique de dosimétrie MC. Un algorithme de ré-échantillonnage du volume de la prostate permet de prendre en compte les changements volumétriques associés à l'œdème dans la dosimétrie

MC. La dosimétrie dynamique avec l'œdème montre des résultats cohérents avec des études précédentes dans la littérature. A savoir qu'il y a une sous-estimation de la dose à cause de l'œdème. Par exemple, pour une amplitude d'œdème de 20%, la dose à la prostate D_{90} et de l'urètre D_{10} sont de 13.6% et 10.6%, respectivement.

Pour conclure nous proposons dans cette thèse un système de traitement inverse pour la curiethérapie prostate qui tient compte d'une personnalisation précise de la dosimétrie mais également de l'œdème de la prostate. Ces travaux peuvent également être utilisés dans d'autres contextes cliniques, tel que la curiethérapie haut-débit, mais également être adapté pour traiter d'autres organes. Dans le futur, nos travaux porteront sur l'étude et la capacité de personnaliser le modèle biomécanique de la prostate proposé à chaque patient en utilisant des mesures d'élasticité via l'élastographie de la prostate. En raison des limitations inhérentes à la FEM, l'incorporation du modèle biomécanique de l'œdème dans le système de planification du traitement est coûteuse en temps de calcul. Une méthode alternative, serait de proposer un nouveau modèle sans maillage afin d'améliorer la simulation de l'œdème pendant la planification intra-opératoire.

This page is intentionally left blank

CHAPTER

1

BACKGROUND

Background information on prostate anatomy and prostate cancer will be described in this chapter. An overview of the risk factors controlling prostate cancer occurrence, the classification and screening methodologies for early detection, and cancer staging will be given. Following, available options for the treatment of prostate cancer will be demonstrated with additional focus on current low-dose-rate (LDR) brachytherapy limitations. Finally, the objective of this thesis, which aims in the optimization of LDR brachytherapy, will be illustrated in detail. By the end of this chapter, the reader is expected to have a broad view of prostate cancer and to be able to follow effortlessly the developments of the following chapters for the improvement of LDR brachytherapy delivery. More specific theoretical aspects of the following developments will be given in the following chapters.

Des informations générales sur le cancer de la prostate ainsi que l'anatomie de la prostate seront décrites dans ce chapitre. Un aperçu des facteurs de risque qui contrôlent l'apparition du cancer de la prostate, la classification et les méthodes de dépistage précoce et la mesure de son évolution seront donnés. Enfin, l'objectif de cette thèse, qui vise à optimiser la curiethérapie bas-débit dose de la prostate sera présenté en détail. À la fin de ce chapitre, le lecteur devrait avoir une vision large du cancer de la prostate et pouvoir suivre facilement les développements des chapitres suivants. Des aspects théoriques plus spécifiques des développements durant cette thèse, seront présentés dans les chapitres suivants.

"All achievements, all earned riches, have their beginning in an idea."

— Napoleon Hill

1.1 The prostate gland

The *prostate* is an accessory gland of the male reproductive system found in most mammals. In humans, the prostate is located in the sub-peritoneal space between the urogenital diaphragm and the bladder (see Figure 1.1). It has the shape of a chestnut with an average weight in adults of 25-30 g and is approximately 4 cm long and 3 cm thick [Van De Graaff, 1995]. Moreover, it is oriented with its base directed to the bladder neck and its apex to the urogenital diaphragm. Behind the prostate is located the rectum, making possible to feel the prostate during digital rectal examination. In addition, the prostate surrounds the initial part of the urethra at the height of ejaculatory ducts (prostatic urethra).

Its role is the production of an alkaline fluid that combined with sperm cells from the testicles and seminal vesicle fluid makes up semen. During ejaculation, prostatic muscle cells contract and push the prostatic fluid out of the prostatic ducts into the urethra, where is mixed with the rest semen components before been released. Furthermore, the prostate secretes the enzyme acid phosphatase, which is often measured clinically to assess prostate function, and the prostate-specific antigen (PSA). PSA is a protein that, when is in high concentration in blood, indicates possible prostate cancer occurrence.

The prostate tissue can be divided into four different parts [McNeal, 1981]. The transition zone, the central zone, the peripheral zone, and the anterior fibromuscular stroma. These parts display histological and physiological differences between them and they are surrounded by a fibrous tissue. Often the surrounding fibrous tissue is referred as the prostatic capsule, even if there is not a true anatomic capsule but rather a mix of loose connective and adipose tissue surrounding the prostate gland.

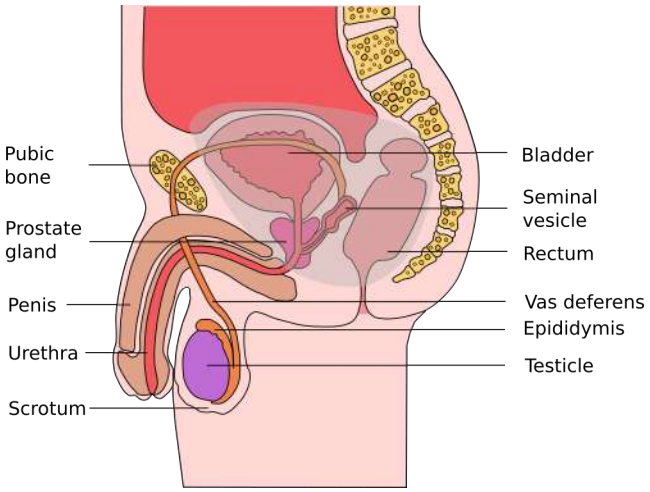

Figure 1.1 – The male reproductive system's anatomy. Prostate is located in the sub-peritoneal space between the urogenital diaphragm and the bladder in front of the rectum.

1.1.1 Transition zone

The *transition zone* is composed of two small lobules lateral to the urethra in the mid-gland, occupying about 5-10% of the prostate glandular tissue. Histologically, the glandular tissue of the transition zone has the same origin with the tissue found in the peripheral zone (see Figure 1.2). This segment of the prostate is involved in the development of benign prostatic

hyperplasia (BPH) and, less commonly, adenocarcinoma. Carcinomas originating from this zone have lower malignant potential and higher recurrence-free survival rates [Lee et al., 2015]. Despite this, some other studies suggest that there is no significant difference in outcome when controlled for grade and stage [Oh et al., 2003].

1.1.2 Central zone

The *central zone* is a cone-shaped area surrounding the ejaculatory duct apparatus that makes up the majority of the prostatic base (see Figure 1.2). It occupies about 20% of the prostate glandular volume. Certain enzymes of the seminal fluid are produced by the epithelial cells located specifically in this zone. The central zone is the most distant prostate segment from the rectum. As a result, prostate tumors in this zone, even if rare to appear, cannot be felt during digital rectal examination.

1.1.3 Peripheral zone

The outer zone of the prostate, called the *peripheral zone*, occupies 70-75% of the prostatic glandular tissue. It extends posterolaterally from the apex to the base near the rectum and surrounds the distal urethra (see Figure 1.2). In this zone, carcinoma, chronic prostatitis, and post-inflammatory atrophy are relatively more common than in the other zones [Hammerich, Ayala, and Wheeler, 2009].

1.1.4 Anterior fibromuscular stroma

The *anterior fibromuscular stroma* consists the one-third of the volume of tissue within the prostatic capsule (see Figure 1.2). It provides the convexity of the anterior surface of the prostate and has not proven role in prostatic function and pathology. The anterior fibromuscular stroma surrounds and compresses the urethra at its distal end. Furthermore, it has a significant role in involuntary sphincter functions.

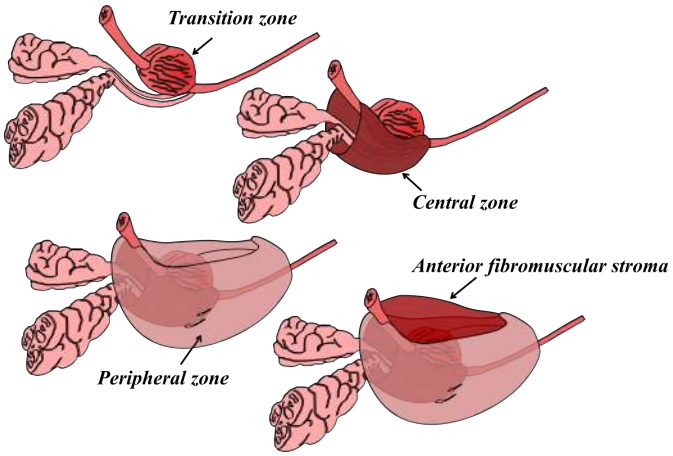

Figure 1.2 – The prostatic zones. Prostate is composed of four segments: the transition zone, the central zone, the peripheral zone, and the anterior fibromuscular stroma.

1.2 Prostate cancer

Prostate cancer is the most common type of cancer diagnosed in western countries and the second most lethal among men. In France, prostate cancer is the most common type of cancer in the male population. In 2012, 56841 new cases of prostate cancer and 8876 deaths were estimated [INCF, 2016].

While prostate cancer (PCa) is a leading cause of cancer death, the vast majority of men that will receive treatment will survive the disease and ultimately will die from other causes. The probability for a man to be diagnosed with prostate cancer, during his lifetime, is 16.6%. Among prostate cancer patients, few will proceed to treatment interventions, as many tumors will remain idle throughout the patient's life. Approximately, less than 20% of all prostate cancer patients will die from this disease. Nevertheless, prostate cancer patients who survive the disease may well suffer from disease relapse or treatment-related complications during their lifetime.

The aggressiveness of prostate cancer can be quite variable, ranging from localized idle tumors without any symptoms to widely metastatic treatment-resistant tumors. Therefore, understanding the risk factors of the disease and classifying accurately the prostate cancer types is essential for early detection and successful treatment of the disease.

1.2.1 Risk factors

Prostate cancer *risk factors'* evaluation is challenging due to the lack of extensive epidemiological studies. Current insight in PCa risk factors is obtained from several large, well-controlled, case studies and a few cohort studies.

PCa is one of the most age-dependent cancers. It is rare to occur before the age of 50, while the occurrence possibility increases exponentially thereafter. After age, the strongest risk factors for PCa, identified from case-control studies, are having a family history of PCa, and having a high dietary fat intake. Additionally, changes in plasma levels of key hormones and associated molecules or naturally occurring variants in genes (polymorphisms) might alter PCa risk. Likewise, dietary factors may affect PCa risk [Masko, Allott, and Freedland, 2013].

The causes of PCa still remain unclear, and extending our understanding on them is critical for the improvement of disease prevention. Eventually, PCa risk factors assessment is an open field of research.

1.2.2 Classification

Prostate cancer *classification* is indispensable for prognosis and therapy guidance. The treatment is suitably adjusted based on the PCa classification grade. The modified Gleason score (GS) system of the International Society of Urological Pathology (ISUP) 2005 is the recommended prostate cancer grade system. In biopsy, GS is the Gleason grade of the most extensive plus the highest pattern, regardless its extent. However, in radical prostatectomy (RP) a pattern comprising $\leq$5% of the cancer volume is not included in the GS, but its proportion should be reported separately if it is of grade 4 or 5.

The 2014 ISUP Gleason Grading Conference on Gleason Grading of Prostate Cancer [Epstein et al., 2016] adopted the concept of grade groups of PCa to align PCa grading with the grading of other carcinomas, eliminate the anomaly that the most highly differentiated PCas

have a GS 6, and highlight the clinical differences between GS 7 (3 + 4) and 7 (4 + 3) (see Table 1.1).

Table 1.1 – International Society of Urological Pathology 2014 grade groups

Gleason score	Grade group
≤ 6(3 + 3 or 3 + 2 or 2 + 3 or 2 + 2)	1
7(3 + 4)	2
7(4 + 3)	3
8(4 + 4 or 3 + 5 or 5 + 3)	4
9 – 10	5

It is advisable grade groups to be reported in addition to the overall or global Gleason score of a prostate biopsy or radical prostatectomy.

1.2.3 Screening and early detection

Screening aims in the *early detection* of cancer before the appearance of symptoms. PCa screening is based on the measurement of the level of PSA found in the blood. PSA is a glycoprotein enzyme produced by the epithelial cells of the prostate. Its role is the liquefaction of semen in order sperm to move freely. Elevated PSA level in serum may indicate cancer, benign prostatic hypertrophy, prostatitis, and other non-malignant conditions.

Screening based on PSA identifies additional cases of PCa but its effect on PCa-specific mortality is not yet clear. No statistically significant effect on PCa-specific screening is found in most trials, with many of them presenting conflicting findings [Schroder et al., 2009 and Andriole et al., 2009]. The ERSPC trial found an association of PSA screening with a 20% relative reduction in risk for PCa-specific death in a prespecified subgroup of men aged from 55 to 69 years [Schroder et al., 2009], whereas the PLCO trial found no effect [Andriole et al., 2009]. In addition, screening is associated with overdiagnosis and overtreatment, leading many organizations to caution against routine population screening. PSA-based screening is linked with detection of more prostate cancers, poor PCa-specific mortality reduction, and harms related to false-positive test results [Chou et al., 2011].

In order to maintain the potential benefit of early PCa detection while decreasing the risk of overtreatment, the link between diagnosis and active treatment should be broken by following specific screening guidelines [Mottet et al., 2016].

1.2.4 Staging

The *stage*, or in other words the extent, of prostate cancer is a critical factor during prognosis and treatment approach selection. PCa staging is based on results derived from the prostate biopsy, the PSA level in the serum at the time of diagnosis, and any other related exam. The purpose of a staging system is the characterization of the cancer spread. The most common PCa staging system is the American Joint Committee on Cancer (AJCC) TNM system.

The TNM staging system is based on 3 category groups (T, N, and M) and additionally the PSA level at the diagnosis time plus the prostate biopsy Gleason score. T categories refer to the extent of the primary tumor and range from T0 to T4. The categories N describe the spread of

cancer to nearby lymph nodes. NX corresponds to no lymph nodes assessment, N0 to no spread in lymph nodes and N1 to spread in lymph nodes. Finally, the categories M are describing the extent of metastasis in other parts of the body, with M0 referring to no metastasis occurrence other than in the nearby lymph nodes and M1 signifying metastasis beyond the nearby lymph nodes. T and M categories are subdivided into further subcategories for more detailed stage characterization.

The TNM staging system categories are summarized in Table 1.2. A complete overview of these staging categories can be found in [Ohori, Wheeler, and Scardino, 1994].

Table 1.2 – American Joint Committee on Cancer (AJCC) TNM staging system

Stages	T	N	M
Stage 0	Tis[a]	N0	M0
Stage I	T1	N0	M0
	T2	N0	M0
Stage II	T3	N0	M0
	T4	N0	M0
Stage III	T1, T2	N1 or N2	M0
	T3, T4	N1 or N2	M0
Stage IV	Any T	Any N	M1

[a] Defines carcinoma in situ.

PCa cancer stages can be derived by several combinations of the T, N, and M categories.

1.3 Prostate cancer treatment

Nowadays various therapeutic options are available for the *treatment of prostate cancer* with regard to its stage. Among these options more common are the active surveillance, radical prostatectomy, chemotherapy, external beam radiotherapy, and transperineal brachytherapy (low/high-dose-rate).

Therefore, therapeutic management of PCa has become more complex. Patients with low-risk PCa (PSA < 10 ng/ml and biopsy Gleason score 6 and cT1c-cT2a) or with intermediate-risk PCa (PSA 10.1-20 ng/ml or biopsy Gleason score 7 or cT2b-c) should be counseled by an interdisciplinary group consisted of an urologist and a radiation oncologist, to discuss possible treatment options. Patients with high-risk PCa (PSA < 20 ng/ml or biopsy Gleason score 8-10 or cT3a) should be counseled by a multidisciplinary tumor board.

Among the available treatment options, it is not possible to specify which is superior over the other due to the lack of randomized controlled trials in this field. However, based on the available literature, some recommendations can be made.

1.3.1 Active surveillance

Active surveillance (AS) must not be confused with watchful waiting. The latter is based on a delayed symptomatic non-curative treatment on patients who are not candidates for an aggressive local therapy, while AS is a suitable treatment option for patients who might also be offered a curative alternative. Very low-risk PCa patients are initially not treated but are

monitored and will receive treatment with a curative intent in case of progression or if the threat of progression occurs during follow-up [Heidenreich et al., 2014a].

AS was introduced aiming to reduce the ratio of overtreatment in patients with low-risk PCa. According to recent data, good candidates for AS are men with low-risk PCa and high life expectancy (>10 years). From the patients that will receive AS approximately 30% will require delayed radical intervention [Klotz et al., 2010].

1.3.2 Radical prostatectomy

Radical prostatectomy (RP) is an active treatment option for PCa where the whole prostate is surgically removed. Nerve-sparing RP is the gold standard approach for men with a normal erectile function and organ-confined cancer. The need for, and the extent of, pelvic lymphadenectomy is controversial. In men with low-risk PCa and <50% positive biopsy cores the risk of lymph node involvement is lower than in men with intermediate- or high-risk PCa [Heidenreich et al., 2011]. To patients of the latter group, extensive pelvic lymphadenectomy should always be performed [Briganti et al., 2006].

1.3.3 Androgen deprivation therapy

Androgen deprivation therapy (ADT) is the standard treatment option for advanced metastatic PCa. Surgical (orchiectomy) or medical ADT (hormone treatment) alleviates symptoms in many patients [Sharifi, Gulley, and Dahut, 2005] by decreasing the male hormones which support the prostate cancer growth. ADT can also be used as a complement to other treatments, such as radical prostatectomy, to increase their effectiveness by shrinking the PCa prior to the main treatment.

Among the possible agents, luteinising hormone-releasing hormone (LHRH) agonists have become the standard choice for ADT due to their reversibility potential, the lower risk for cardiotoxicity, the absence of psychological stress associated with orchiectomy, and their oncologic efficacy [Heidenreich et al., 2014b]. During the first weeks of LHRH-agonist therapy, an initial increase in testosterone levels is observed (flare).

Contrary to the agonists, LHRH antagonists result in a prompt decrease in targeting hormones (luteinising hormone, follicle-stimulating hormone and testosterone) levels without the occurrence of flare phenomenon. In recent studies, rapid suppression of testosterone has been shown within the first 3 days without flare phenomenon and with lower risk of PSA- and PCa-specific death [Klotz et al., 2008, and Tombal et al., 2010].

The speed and effectiveness of LHRH-antagonist therapy possesses a significant role in the treatment of patients with advanced metastatic disease. However, the benefit of the treatment in other clinical situations remains to be proven.

1.3.4 Chemotherapy

Chemotherapy is not so common as other treatment options (radical prostatectomy, external radiotherapy, brachytherapy) for the treatment of prostate cancer. It is usually an option for patients who have been diagnosed with metastatic PCa. It is offered alongside hormone therapy to improve the outcome of the latter, or alone to patients that have undergone previously hormone therapy and demonstrate disease relapse [Gibbons, 1987].

Chemotherapy drugs aim to delay or improve symptoms and decrease cancer's growth. However, their effectiveness is still not optimal due to the limited understanding of the biology of PCa [Petrylak, 1999]. Among chemotherapy drugs, docetaxel has demonstrated superior survival levels and symptoms improvement, when given with prednisone [Tannock et al., 2004].

1.3.5 External beam radiotherapy

External beam radiotherapy (EBRT) is a non-invasive treatment option where high-energy photon beams are used to kill cancer cells. A high-energy X-ray beam, produced by a linear accelerator, is directed to the prostate gland for the elimination of PCa. EBRT is advised for patients with localized cancer inside the prostate or with a limited spread in the proximal area.

The deposition of high-energy radiation in cancer cells results in ionization and eventual destruction of the genetic material, leading to cellular death. Ionization and genetic material damage occur also in healthy tissue cells in the beam's trajectory, but genetic material repair mechanisms, absent in cancer cells, restore the damaged tissue if the damage is tolerable. Nevertheless, side effects related to the healthy tissue damage such as urination difficulties, rectal bleeding, diarrhea, secondary cancer in the radiated region, and etc. are common, depending on the extent of the healthy tissue irradiation. Therefore, extra caution should be taken during the decision of treatment delivery.

In order to decrease the side effects occurrence in external beam radiation, intensity-modulated radiotherapy (IMRT) and its more recent update, the volumetric modulated arc therapy (VMAT), are two widely used methods. IMRT is an advanced form of three-dimensional conformal radiotherapy (3D-CRT) where intensity-modulated beams are used to irradiate the tumor from multiple angles. The intensity modulation of the radiation beams allows for higher conformity than conventional 3D-CRT and further reduction of the dose deposited in healthy surrounding tissues (see Figure 1.3). VMAT allows the delivery of three-dimensional optimized dose distribution in a single gantry rotation. Treatment time with VMAT is smaller compared to conventional IMRT and the dose deposited to the clinical target (CTV) can be increased without violating OAR dose constraints [Shaffer et al., 2009].

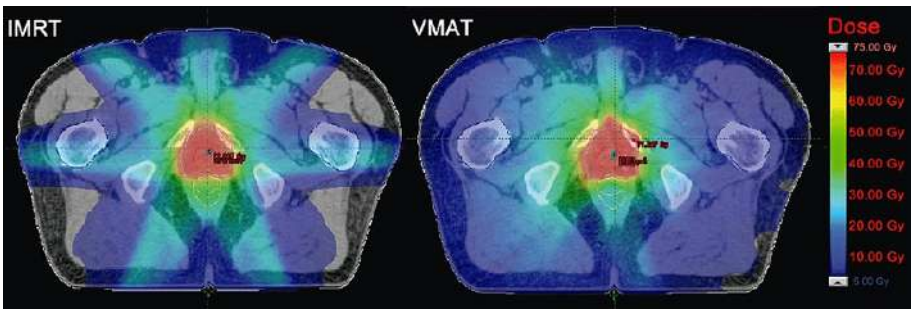

Figure 1.3 – Intesity-modualated (IMRT) and Volumetric modulated (VMAT) radiotherapy. VMAT allows for the delivery of increased dose at the target without violating OAR dose constraints and in reduced treatment time, compared to IMRT.

The treatment dose to be delivered depends on the stage of PCa. For low-risk PCa, at least 74 Gy should be delivered while for intermediate-risk PCa a higher dose in the range of 76-81 Gy is more effective. In high-risk PCa, external beam radiation is combined with ADT to reduce the risk of systematic relapse.

1.3.6 Transperineal LDR/HDR brachytherapy

Transperineal prostate brachytherapy is a least invasive and efficient treatment option for patients with organ-confined cancer. Candidates for treatment with transperineal brachytherapy alone, i.e. as monotherapy, include those for whom there is a significant likelihood that their PCa could be encompassed by an adequate dose distribution from this procedure alone. Patients with fewer than 5 years life expectancy, bleeding disorder, significant obstructive uropathy, pathologically positive lymph nodes, and distant metastases should not receive transperineal brachytherapy as a treatment option.

Low-dose-rate (LDR) brachytherapy

The longest experience of prostate brachytherapy is with *low-dose-rate (LDR) brachytherapy*, using Iodine-125 or Palladium-103 seeds. ^{125}I decays with a half-life of 59.43 days to a low-energy excited state of ^{125}Te, which immediately decays to stable ^{125}Te by gamma decay with emission energy of 27 keV. Likewise, ^{103}Pd decays to ^{103}Rh by electron capture emitting gamma photons with energy of 21 keV, but with a shorter half-life of 16.99 days. Due to its shorter half-life, ^{103}Pd has been proposed as more suitable for the treatment of aggressive cancers (Gleason score of 8-10), even though this has not been proven in clinical studies.

During LDR brachytherapy ^{125}I or ^{103}Pd seeds are implanted permanently in the prostate in order to deliver locally therapeutic dose, while sparing the surrounding healthy tissue. Prior LDR brachytherapy, a pre-planning step can be made based on transrectal ultrasound (TRUS) or CT/MRI imaging. A template guide with holes arranged with 0.5 cm spacing, both vertically and horizontally, is mounted on the TRUS probe. This forms a 2D grid of possible needle placing positions (see Figure 1.4). In the pre-treatment planning process, the patient is positioned in the same lithotomy position of the operation. The TRUS is calibrated carefully such as the largest prostate slice is in the middle of the template guide and a template hole will be available for the introduction of all the necessary needles.

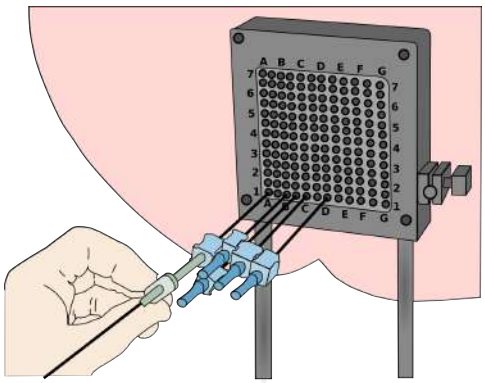

Figure 1.4 – TRUS template guide. A template guide with equally spaced holes is mounted on the ultrasound probe to facilitate the guidance, and later the reporting of the inserted needles.

Using a treatment planning software, the prostate is delineated in the TRUS image with an additional margin according to GEC ESTRO guidelines [Gerbaulet, 2002]. The urethra and rectal wall are organs at risk (OARs) and should be defined too. The prostate volume can then

be extracted and the positions of the seeds can be selected. The recommended prescription dose for the prostate (clinical target volume), is 145 and 125 Gy for ^{125}I and ^{103}Pd seeds respectively. According to the AAPM TG-137 [Nath et al., 2009] the D_{10} at the urethra, the delivered dose to 10% of the urethra volume, should be less than the 150% of the prescribed dose and the D_{2cc} at the rectum, the minimum dose deposited to the highest irradiated 2cc area, should be less than the prescribed dose.

Pre-treatment planning is a fundamental step of the brachytherapy procedure. However, one disadvantage is that the position of the patient during the operation can be different than that during the pre-treatment planning imaging. Therefore, many centers choose to perform the planning phase during the operation. Thusly, the operation time is increased but positioning errors are avoided.

During the operation, the needles are inserted in the planned positions. Needles can be inserted one by one and directly loaded or all together and be loaded afterward. The needle placing is guided by TRUS and seeds are deposited in the required positions. Seeds have typically 4.5 mm length and 0.8 mm diameter. They are pushed in the prostate using a stylet. By retracting the device by 5, or more, millimeters each time, seeds are placed from distant to proximal locations (see Figure 1.5). The seeds can be loosed or stranded in a suture of polyglactin. Loose seeds provide more freedom in their placement but it is easier to migrate. On the contrary, when stranded seeds are used, migration is more restricted but differential loading (tight or distant seeds placement to improve the dose distribution) is more difficult.

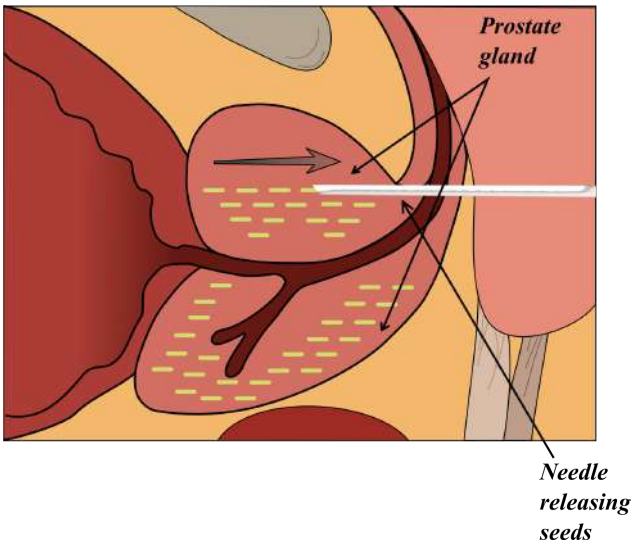

Figure 1.5 – Seeds placement. Retracting the needle by 5, or more, millimeters each time seeds are deposited in the planned positions in the prostate from distant to proximal locations.

After the insertion of all seeds and the removal of the needles, C-arm or CT-C-arm fluoroscopy is performed to count the number of seeds in the body of the patient. Accidentally misplaced seeds in the bladder of the patient are removed. Commonly, migration of seeds in other parts of the patient's body is rare at this time. It usually can occur after 1 or more months up to 1 year after the implantation. Migrated seeds can often be found in the thorax and also in the pelvic lymph nodes. Additionally, it is often possible for seeds to pass in the urine.

In the end of the procedure, the patient is hospitalized for one or two nights. Before leaving the hospital, it is checked that the patient can urinate and receives information on radiation

safety and possible side effects that might occur. After a period of approximately one month, the patient returns and undergoes a CT scan acquisition. Post-implant dosimetry is performed to evaluate differences between the planned and the actual delivered dose.

High-dose-rate (HDR) brachytherapy

High-dose-rate (HDR) prostate brachytherapy is a transrectal ultrasound-guided transperineal procedure similar to LDR procedure. However, instead of permanent low-dose-rate sources, after-loading applicators are placed in the prostate to direct the temporary insertion of a high-dose-rate source for the treatment of PCa. Typical high-dose-rate sources are loaded with Iridium-192 (^{192}Ir). In addition to LDR, HDR exploits the radiobiology of PCa. Due to the higher sensitivity of PCa over the normal tissue to radiation delivered in high dose fractions it can ensure additional sparing of normal tissues [Challapalli et al., 2014].

HDR brachytherapy procedure is performed with the patient under general or spinal anesthesia in the lithotomy position. After-loading applicators are placed through a template in the prostate guided by transrectal ultrasound (see Figure 1.6).

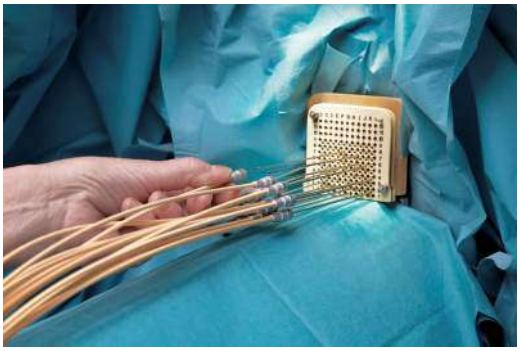

Figure 1.6 – HDR applicators insertion. After-loading applicators are placed through a template in the prostate, guided by TRUS, in order to insert temporarily a high-dose-rate ^{192}Ir source that delivers tumoricidal dose to the PCa. Image from [Kovács and Hoskin, 2013].

In common practice, the entire prostate is treated and applicators are placed at approximately 10 mm distance around the periphery of the gland. Furthermore, applicators at the central row of the template are placed at the extreme periphery to avoid urethral damage. An inner row of applicators is also placed to provide better dose control around the urethra. Lastly, the applicators are pushed beyond the prostate base to ensure the dose coverage of the base.

The source positions and source dwell times, time that the source remains at a given position, are determined using an inverse planning software to provide optimal dose distribution to the prostate and minimum dose to the OARs. Deviations of the true locations of the applicators from the pre-planned, ideal, positions must be accounted by the planning system. The source positions and dwell times are modified if necessary to consider these deviations.

The corrected treatment plan is transferred to the remote after-loader which delivers the source through the appropriate needles sequentially to the determined dwell positions for the corresponding dwell times (see Figure 1.7). This method is more flexible than LDR prostate brachytherapy. Source positions and dwell times can be adjusted in real time providing more precise dose distribution with improved selectivity. On the other hand, HDR brachytherapy requires several sessions associated with a brief hospital stay.

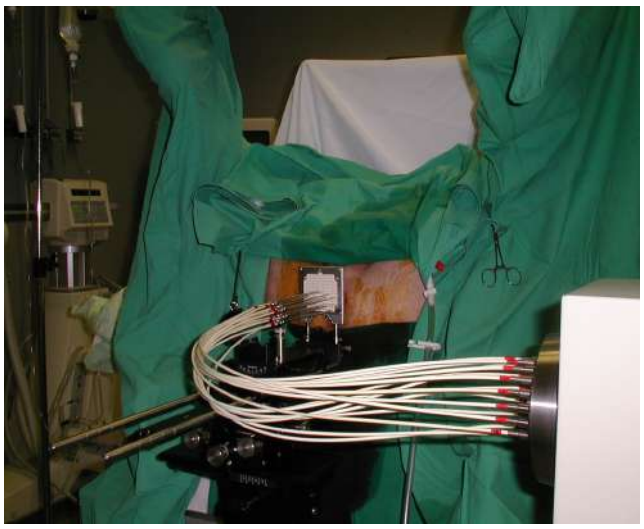

Figure 1.7 – HDR after-loader. The after-loader controls the delivery of the source at the corresponding dwell positions for the given dwell times according to the available treatment plan. Image from [Kovács and Hoskin, 2013].

1.3.7 Focusing on LDR brachytherapy

Among the available treatment options for prostate cancer, transperineal brachytherapy is one of the most appealing. It demonstrates less toxicity-related side-effects than EBRT as a result of the local deposition of radiation from sealed radioactive sources (seeds), implanted in the target area. In addition, it is less invasive than radical prostatectomy. Surgery related side-effects are hence, significantly reduced and the patient is able to leave the treatment center after one-two days of hospitalization.

Between HDR and LDR brachytherapy, LDR is an one-time procedure and has been the gold standard for the treatment of low risk patients since many years. On the other hand, HDR brachytherapy enables to control over its postimplant dosimetry (source position and dwell time modulation), however it requires several sessions [Skowronek, 2013].

While equivalent outcomes in localized prostate cancer with LDR or HDR brachytherapy are supported by radiobiological models, LDR is preferred by many clinical centers for practical reasons (one-time procedure, reduced hospitalization, etc.). Furthermore, recent advancements in focal treatment with LDR brachytherapy [Peach, Trifiletti, and Libby, 2016] present the advantage of reduced toxicity in surrounding healthy tissues and attract more interest to LDR over HDR brachytherapy. It is therefore necessary to increase the dosimetric control in LDR brachytherapy by addressing current limitations in the treatment's delivery.

1.4 LDR brachytherapy limitations

Despite LDR prostate brachytherapy is widely used with high success rates (75% – 91%), several limitations exist in the current treatment planning systems. The radioactive seeds' placement is guided intraoperatively by TRUS imaging, however the low image quality of TRUS induce difficulty in needle tracking. Moreover, needle artifacts reduce even more the

image quality and seeds' misplacement is a common issue. Current treatment planning systems do not consider the seeds' misplacement and do not provide adaptive planning capabilities.

Furthermore, they are based on simplified dosimetric models. These models are error-prone due to the considered rough approximations. In more detail, dose calculation is based on the 1995 AAPM Task Group No. 43 (TG-43) report [Meigooni, 1995] and its more recent TG-43U1 [Rivard et al., 2004] and TG-43U1S1 [Rivard et al., 2007] updates, where several approximations in regard to patient's anatomy and seed geometry are incorporated. Additionally physiological changes during and after the operation, such as formation and resorption of edema, that can lead to significant dosimetric errors, are not considered. Due to this number of unconsidered factors, inverse planning algorithms provide sub-optimal results with significant impact in the final outcome of the procedure.

The current standard in dose calculation formalism, edema modeling, and inverse planning are described in the following and associated limitations are highlighted.

1.4.1 TG-43 dose calculation formalism

The *TG-43 formalism*, which is the current worldwide standard for LDR brachytherapy dose calculation, describes dose deposition around a single source centrally positioned in a spherical water phantom. The dose rate is calculated by

$$\dot{D}(r,\theta) = S_k \cdot \Lambda \cdot \frac{G_L(r,\theta)}{G_L(r_0,\theta_0)} \cdot g_L(r) \cdot F_L(r,\theta), \tag{1.1}$$

where r is the distance (in centimeters) from the center of the active source to the point of interest, r_0 the reference distance (1 cm) and θ the polar angle specifying the point-of-interest, $P(r,\theta)$, relative to the source longitudinal axis. The reference angle θ_0 defines the source transverse plane and is specified to be 90° or $\pi/2$ radians (see Figure 1.8). S_k denotes the air-kerma strength, Λ the dose rate constant, and $G_L(r,\theta)$ the geometry function (point- or line-source model). Finally, $g_L(r)$ defines the radial dose function and $F_L(r,\theta)$ the 2D anisotropy function. Detailed information on the definition and measurement of the terms consisting the Equation 1.1 can be found in the work of Rivard et al. [2004].

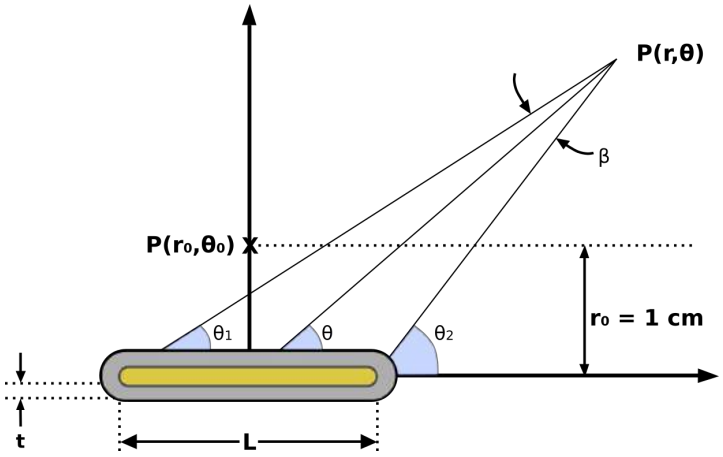

Figure 1.8 – TG-43 Coordinate system. Coordinate system used for brachytherapy dosimetry calculations.

Using Equation 1.1, the dose rate contribution from each source at the point-of-interest is calculated. The sum of all contributions, according to the sources placement, defines the total dose rate. The clinical practicality of TG-43 formulation lies in the fast dose rate calculation for a given sources' placement pattern (seeds' configuration).

However, this method assumes that there are no source-to-source shielding effects, that human tissue is composed by a homogeneous water-equivalent material and that the scattering volume, surrounding the point of calculation, is at least 5 cm of water-equivalent material. Due to the above assumptions, tissue heterogeneities, attenuation between seeds and finite patient dimensions are not considered, leading to a significant increase of dosimetric uncertainties.

For LDR sources, the photoelectric process is dominant therefore, differences in mass-energy absorption coefficients between various tissues and water [White et al., 1989] can result in significant dose differences, depending on the medium chosen for radiation transport and energy deposition [Beaulieu et al., 2012]. As reviewed in AAPM Task Group No. 186 (TG-186), dose differences up to 10% between results of Monte Carlo (MC) simulations, reporting dose to the prostate, and dose calculations in homogeneous water have been demonstrated for ^{125}I and ^{103}Pd sources by Taylor [2006].

The impact of considering the tissue composition on dose distribution and dose-volume histogram (DVH) has been investigated [Chibani, Williamson, and Todor, 2005]. For a treatment plan using ^{103}Pd the D_{100}, the dose deposited to the 100% of the prostate volume, was 6% lower when prostate was modeled as soft tissue rather than pure water. Similarly, differences of 4%-5% in D_{90}, the minimum dose deposited in 90% of the prostate volume, were found evaluating MC simulation results of treatment plans with ^{125}I [Carrier et al., 2006]. In the study of Carrier et al., the dose distribution for a TG-43 calculation was compared to a MC simulation with the prostate modeled as water and full MC simulation using a realistic prostate tissue model. In a later study of the same group [Carrier et al., 2007] the comparison of MC simulations, where material composition was determined using patient CT attenuation data, with the TG-43 formalism revealed a 7% difference in D_{90}, where 3% was associated with the tissue composition and the rest 4% with the attenuation between seeds. In all the mentioned studies, above, a general overestimation of the dose delivered in the prostate and OARs was demonstrated by TG-43.

In order to consider attenuation between seeds, patient geometry, and tissue composition heterogeneities during dose calculation, model-based dose calculation (MBDCA) methods have been developed. The three methods with application in LDR brachytherapy treatment planning are CC superposition/convolution [Carlsson and Ahnesjo, 2000], grid-based Boltzmann equation solvers (GBBS) [Zhou and Inanc, 2002, and Alcouffe et al., 1995] and MC simulations.

Among the MBDCA methods, MC simulation is the gold standard in computational dosimetry. MC techniques are based on iterative random sampling and are used for the solution of probabilistic or even deterministic problems exploiting randomness. The accuracy of MC methods depends strongly on the repetition number of random sampling.

Tissue material composition can be accounted in MBDCA methods by assigning interaction cross sections on each voxel of the patient's image dataset, using the electron densities ρ_e (or the mass densities ρ) derived from CT images. In brachytherapy, where photons with energy < 1 MeV are used, a large difference between mass-attenuation and mass-energy absorption coefficients is observed due to the importance of the photoelectric cross section. Therefore, the knowledge of tissue mass (or electron) density and the atomic number distribution of the

material is crucial [Williamson et al., 2006].

Especially in MC, a material has to be assigned on each voxel in addition to the mass (or electron) density. Consequently, dosimetric calculation accuracy depends strongly on the image segmentation process since inaccuracies in the materials assignment can lead to significant dosimetric errors [Verhaegen and Devic, 2005]. The assigned materials should be described by the elemental composition of materials as given in ICRU report No. 46 [Bethesda, 1992] and in [Woodard and White, 1986].

1.4.2 Edema during brachytherapy

Another significant issue in dosimetry calculation is the presence of edema in the prostate, and especially its variable influence on the dose over time, on post-implant evaluation, and on dose reporting.

Edema occurs due to the insertion of needles for the delivery of the seeds into the prostate gland. The mechanical trauma caused by the needle insertion, the resulting bleeding and the general inflammatory response leads to immediate swelling of the prostate, which reaches the maximum volume shortly after the end of the procedure and is followed by a gradual resorption [Speight et al., 2000 and Whittington et al., 1999]. Additionally, the cellular necrosis due to the dose delivered by the permanently deposited sources supports the inflammation and possibly can have a significant role in the regulation of edema resorption [Butler et al., 2000]. Despite that, no sufficient data exist for the correlation of edema characteristics (extent, temporal resorption pattern) with patient characteristics such as age, pre-implant gland volume, hormone uptake, or with procedure characteristics such as used radioisotope, number of needles, number of implanted sources and total source strength [Taussky et al., 2005a, Waterman et al., 1998, Badiozamani et al., 1999a and Yamada et al., 2003a]. Edema varies significantly from patient to patient and the underlying responsible mechanisms are yet to be understood.

In order to account for edema during dosimetry calculation, analytical models have been developed. In the work of Tejwani et al. [2012], edema was monitored for twenty-nine patients treated with LDR brachytherapy as monotherapy, or combined with external beam radiotherapy (EBRT). An exponential edema resorption pattern was observed similar to previous studies [Waterman et al., 1998] and a correction factor (CF) was proposed to account for dosimetric changes between day 1 and day 30 dosimetry. The proposed CF was calculated for each participating patient as

$$CF = \frac{PV_{30}}{PV_1}, \tag{1.2}$$

where PV_{30} defines the prostate volume as measured on day 30 and PV_1 the prostate volume as measured on day 1. The mean CF was used to estimate the D_{90} on day 30 from the D_{90} on day 1 as given below:

$$D_{90}Day_{30_{estimated}} = \frac{D_{90}Day_1}{CF_{mean}} \tag{1.3}$$

No significant difference was found in the D_{90} on day 30 estimation when the actual patient's CF was used rather than the mean CF. Additionally, in this study the seed activity, the treatment modality (monotherapy or boosted EBRT), and the Gleason score were found as significant edema parameters.

Another approach was proposed [Monajemi, Clements, and Sloboda, 2011 and Sloboda et al., 2012] where an analytical model of edema was developed based on data extracted from serial magnetic resonance imaging measurements on a group of forty patients, who have undergone LDR brachytherapy [Sloboda et al., 2009]. The proposed model described the observed spatially anisotropic and linearly resolving edema based on the edema magnitude (Δ)

$$\Delta = \frac{V_{max} - V_0}{V_0} \tag{1.4}$$

and the edema resorption time, T. In Equation 1.4, V_{max} specifies the prostate volume when maximum edema occurs and V_0 specifies the initial prostate volume with no edema.

Incorporating the described model in the TG-43 (see Equation 1.1), the dose delivered to a calculation point located at distance $\boldsymbol{r}$ relative to the seed can be measured after the edema has resolved by the extended TG-43 formalism for a point source by

$$D(\boldsymbol{r}) = S_k \cdot \Lambda \cdot r_0^2 \cdot \bar{\phi}_{an} \int_0^{\infty} |\boldsymbol{r}(t)|^{-2} \cdot g(|\boldsymbol{r}(t)|) \cdot e^{-\lambda t} dt. \tag{1.5}$$

The relative dose error, associated to disregarding edema was calculated for three ^{125}I implants using the proposed edema model with edema magnitude $\Delta = 0.2$ and edema resorption time $T = 28$ days. The average relative dose error for pre- and post-implant dosimetry was found 2% and 0%-3.5% respectively.

Both models described here are based on volumetric measurements derived using image processing techniques. The use of different modalities for volume information extraction during implantation (US or MRI) and post-implant follow-up (CT or MRI) results in the increase of volume measurement uncertainty, due to the different image quality and tissue visibility. Therefore, leads to inaccurate evaluation of the edema parameters (magnitude, resorption time) that affects significantly the outcome of these models.

Furthermore, edema parameters diversify strongly among patients and edema models should account for this diversion. Sophisticated models, considering tissue mechanical parameters could predict the diversion of edema parameters amongst patients and could eventually improve the dosimetry and success rate of LDR brachytherapy, if would be accounted during the treatment planning.

1.4.3 Inverse treatment planning

LDR brachytherapy *inverse treatment planning* aims in the determination of a seeds' distribution, such that the deposited dose covers completely the planning target volume (PTV) and is not less than the prescribed dose [Lahanas et al., 2004]. In contrast with forward planning, the required dose distribution is given and the seeds' configuration that can deliver this distribution is the unknown. A mathematical expression (cost function) that describes the required dosimetric objectives is constructed. The unknown seeds' configuration is then retrieved by the minimization of the cost function using a dedicated optimization algorithm. The quality of the optimization's outcome is strongly depended on the form of the cost function (smoothness, local extrema) and the optimizing properties of the selected algorithm.

The main dosimetric objectives to be expressed by the cost function is the delivery of as high as possible therapeutic dose to the cancerous tissue and the delivery of as low as possible dose to the OARs and surrounding tissues. Due to the nature of the radiation-tissue interaction

(high penetration, scattering), it is not possible to conform totally the delivered dose in the target area. The simultaneous satisfaction of both objectives is not always feasible and a trade-off between the two must be done.

The problem is updated in finding the seeds' configuration that results to the most proximal to the optimal dose distribution amongst all the possible ones. The similarity of a dose distribution to the optimal one can be naturally quantified by a distance measure, such as the L_p norm.

$$L_p = \left(\sum_{i=1}^{N} (d_i - {d_i}^*)^p \right)^{\frac{1}{p}}, \tag{1.6}$$

where N is the sampling points where the dose values of the given dose distribution d_i are evaluated against the optimal dose values ${d_i}^*$. The dose optimization is interpreted as the minimization of the distance between the ideal dose distribution and the achievable dose distribution. This can be expressed introducing the objective functions $f_L(\boldsymbol{x})$ and $f_H(\boldsymbol{x})$

$$f_L(\boldsymbol{x}) = \frac{1}{N} \sum_{i=1}^{N} \Theta(D_L - d_i(\boldsymbol{x}))(D_L - d_i(\boldsymbol{x}))^p, \tag{1.7}$$

$$f_H(\boldsymbol{x}) = \frac{1}{N} \sum_{i=1}^{N} \Theta(d_i(\boldsymbol{x}) - D_H)(d_i(\boldsymbol{x}) - D_H)^p, \tag{1.8}$$

where $d_i(\boldsymbol{x})$ defines the dose at the i^{th} sampling point that depends on parameters $\boldsymbol{x}$, such as the total seeds' number, p defines the type of the distance norm, N is the number of sampling points, D_L and D_H the low and high dose limits. These expressions are used if dose values above D_L and below D_H are to be ignored, expressed by the step function $\Theta(\boldsymbol{x})$.

In order to address the dose optimization process, several algorithms have been proposed. An iterative geometric optimization algorithm has been proposed by Chen et al. [1997]. In each iteration of this method, a new seed is placed in the coldest spot of the dose distribution in the PTV, improving in each step the dose uniformity. Optimized seeds' configuration is considered the one with the minimum total activity. The minimum total activity varies slowly with the number of the seeds and multiple clinically acceptable seeds' configurations with similar total activity but different individual activities are generated. The configuration with total activity as close as possible to the minimized value is chosen, if an individual activity is matched.

Alternative inverse planning systems based on simulated annealing (SA) have been proposed by various groups [Sloboda, 1992, Sloboda, Pearcey, and Gillan, 1993 and Pouliot et al., 1996]. SA is a metaheuristic optimization algorithm inspired by metal annealing. When a metal is cooling down, slowly enough, its atoms are rearranging to form eventually a crystal structure which corresponds to the global minimum thermodynamic energy state of the system. Similarly, in SA a virtual temperature is used. This temperature is incorporated in the acceptance probability formula of the form

$$P_{accept} = e^{\frac{-\Delta E}{T}}, \tag{1.9}$$

where P_{accept} denotes the acceptance probability of the new configuration, ΔE denotes the energy (cost) difference between the previous and new configuration, and T defines the virtual temperature. Lower energy configurations are always accepted, while higher energy

configurations can be accepted if the acceptance probability is higher than a specified threshold (usually randomly selected from a uniform distribution). The particularity of SA is the ability to escape from local minima in the initial steps of the algorithm where T is high. While T is gradually decreasing the system's state is hopefully in the global optimum area and only "better" solutions are accepted (see Figure 1.9).

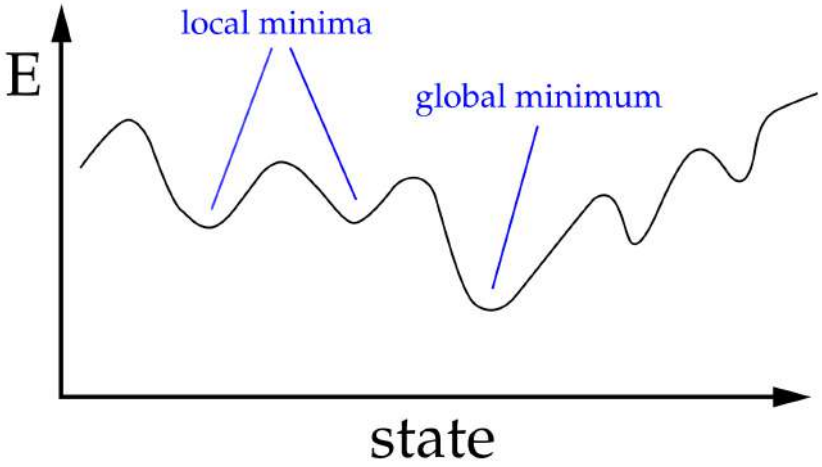

Figure 1.9 – Energy (cost) function with several minima. The global minimum is located at the state with the lowest energy (E).

In the SA-based optimization scheme proposed in [Pouliot et al., 1996] several objectives, with manually adjusted importance factors by the operator, are optimized simultaneously providing control over the dose to be deposited on the PTV and the cold-/hot-spot occurrence. The whole optimization procedure is completed in approximately 15 minutes.

Genetic algorithm (GA), another metaheuristic optimization algorithm, has also been applied in LDR brachytherapy optimization [Yu and Schell, 1996, Yang et al., 1998, and Yu et al., 1999].

GA is a variant of evolutionary algorithms [Deb, 2001]. It is designed for solving optimization problems based on a natural selection process inspired from biological evolution. In contrast to SA, GA generates a population of candidate solutions in each iteration, rather than one. The candidate solutions are evaluated and then ranked from best to worst. New solutions are generated from the previous ones following the process of elitism, mutation or crossover [Vasconcelos et al., 2001].

In a recent study, a new approach for the optimization of LDR brachytherapy using a compressed sensing inspired solver has been proposed [Guthier et al., 2015]. Compressed sensing is a signal processing technique for signal reconstruction, exploiting the sparsity of a signal through optimization to recover it from fewer samples than required by the Shannon-Nyquist sampling theorem [Luke, 1999]. Guthier et al. in their work exploit the sparsity of the seeds' configuration to optimize a multi-objective function considering dose delivery both in PTV and OARs within few milliseconds.

Per contra, compressed sensing solvers are greedy algorithms and do not guarantee to identify the global optimum. Under center conditions, the global optimum can be found with high probability, however, was not investigated whether the LDR brachytherapy optimization problem satisfies these conditions.

1.5 Thesis objective statement

The objective of this thesis is to optimize the treatment planning of low-dose-rate prostate brachytherapy. The goal is to meet the limitations of current planning systems as described in Section 1.4. The planning of the brachytherapy procedure can be summarized in the decision of optimal seed positions, so that the maximum possible dose is delivered to the tumor target while simultaneously depositing as little dose as possible in the OARs and surrounding tissues.

Inverse treatment planning systems that reduce the time required to complete a dose plan are already available in clinical routine. However, the accuracy of the solution depends on the models and calculation methods used in these systems. For reasons of computation speed, since the plan is performed intraoperatively, the `AAPM TG-43` dose formalism is used. However, it considers the patient as a volume of water, which introduces an important approximation on the performed treatment plan. In addition, there is another important approximation on treatment planning. In fact, the insertion of the needles as well as the radiation-induced tissue necrosis creates a physiological response which results in the creation of prostatic edema. Deformations of the prostate and surrounding tissues during and after surgery due to edema are not taken into account by current treatment planning systems. As a result, once more, there is a significant gap between the estimated plan and the treatment that will be provided to the patient.

The goal of this work is to help improve the treatment planning of prostate brachytherapy. To do so, recalling the two main limitations, namely, the approximate dose calculation and the non-consideration of the edema will be addressed by proposing:

1. An inverse treatment planning system (ITPS) with a dose calculation mechanism based on Monte Carlo (MC) simulation methods to take into account the heterogeneity of the patient's tissues (by image acquisition). To ensure cumputational time complying to clinical restrictions, the dose calculation engine `GGEMS`, which employs graphics processing units (GPUs), will be used. This system will be combined with a fast simulated annealing optimization method and a cost function based on dose volume histograms.

2. A biomechanical model of the edema evolution mechanism. Based on theories of elasticity and mixtures, a computational model is developed and incorporated into the ITPS dose calculation mechanism. The objective of this development is the correlation between the mechanical properties of the patient's specific tissues and the parameters of the edema (magnitude, resorption time), in order to allow the in situ prediction of the edema evolution mechanism and the integration of this information in the seed implant positions planning.

This manuscript will present these two suggestions for improvements in prostate brachytherapy treatment planning in 3 main chapters.

Chapter 2 will describe the methods for the implementation of the ITPS. The methodology assumptions will be presented, in particular on the conversion of the patient into a computational phantom from intraoperative ultrasound images and its effect on the accuracy of MC simulations. The dosimetric objectives will be translated into a cost function and a methodology for optimization will be established. The optimization capabilities of the proposed ITPS will be evaluated with actual clinical plans using the recommendations of `AAPM TG-137`.

In Chapter 3, a brief introduction on the theoretical aspects of continuum mechanics and numerical modeling will describe the biomechanical model of edema that will be proposed. A series of experiments for the model's evaluation will be carried out and will make it possible to understand the important parameters of the model and in particular the impact of the tissue elasticity in the formation of the edema.

Chapter 4 will be the last chapter describing the methodology. This chapter will propose a strategy to incorporate the edema biomechanical model into the dosimetry of the ITPS, including the introduction of a dynamic dosimetry system. The advantage of this approach is that allows the consideration of anatomical changes in dosimetry. It will be studied by comparing the intraoperative and postoperative dosimetry according to different scenarios of edema evolution. A representative case will be selected to demonstrate the ability of the proposed strategy to produce treatment plans where the seeds migration is considered in dose calculation during treatment planning.

To conclude, a final chapter of discussion and conclusion will be presented. It will focus on the major results of this thesis but also on the different approximations and consequently the various points that still need to be improved as perspectives.

1.6 Objective de thèse

L'objectif de cette thèse est d'optimiser la planification dosimétrique de la curiethérapie prostate à bas débit de dose. Le but est de répondre aux limites des systèmes de planification actuels tels qu'ils sont décrits dans la section 1.4. La planification de la procédure de curiethérapie peut être résumée dans la décision des positions optimales des grains, de sorte que la dose maximale possible soit délivrée à la cible tumoral alors que, simultanément, déposée le moins de dose possible dans les OAR et les tissus environnant.

Il existe en routine clinique des systèmes de planification de traitement inverse qui facilitent le temps de réalisation d'un plan de dose. Toutefois, l'exactitude de la solution dépend des modèles et méthodes de calcul employés dans ces systèmes. Pour des raisons de rapidité de calcul, car le plan est réalisé en peropératoire, le formalisme de calcul de la dose `AAPM TG-43` est utilisé. Cependant il considère le patient comme un volume d'eau, qui apporte une approximation importante sur un plan de dose réalisé à partir d'un tel formalisme. En plus de cela, il existe une autre approximation importante sur la planification du traitement. En effet, l'insertion des aiguilles ainsi que la nécrose des tissus par irradiations créées une réponse physiologique qui se traduit par la création d'un œdème de la prostate. Les déformations de la prostate et des tissus environnants pendant et après l'opération en raison de la formation d'un œdème ne sont pas prises en compte par les systèmes actuels de planification du traitement. En conséquence, encore une fois, il y aura un écart important entre le plan estimé et le traitement qui sera prodigué au patient.

L'objectif de cet travail est de contribuer à améliorer la planification de dose du traitement de curiethérapie de la prostate. Pour cela les deux limitations principales évoquant ultérieurement à savoir le calcul de dose approximatif et la non considération de l'œdème sera résolue en proposant :

1. Un système de planification de traitement inverse (ITPS) avec un mécanisme de calcul de dose basé sur des méthodes de simulation par Monte Carlo (MC) permettant de prendre en compte l'hétérogénéité des tissus du patient (via une image scanner). Pour garantir un

temps clinique le moteur de calcul de dose GGEMS utilisant des processeurs graphiques (GPU) sera utilisé. Ce système sera combiné à une méthode d'optimisation par recuit simulé et une fonction de cout basé sur les histogrammes de volume de dose.

2. Un modèle biomécanique du modèle d'évolution de l'œdème. Sur la base des théories de l'élasticité et des mélanges, un modèle de calcul est développé et incorporé dans le mécanisme de calcul de la dose MC de l'ITPS. L'objectif de ce développement est la corrélation entre les propriétés mécaniques des tissus spécifiques du patient et les paramètres de l'œdème (grandeur, temps de résorption), afin de permettre la prédiction in situ du modèle d'évolution de l'œdème et d'intégrer cette information dans la planification de la position des grains.

Ce manuscrit présentera ces deux propositions d'améliorations de la planification de la dose en curiethérapie prostate en 3 chapitres principaux.

Le chapitre 2 décrira les méthodes pour la réalisation de l'ITPS. Les hypothèses seront présentées, notamment sur la conversion du patient en fantôme numérique à partir d'images ultrason peropératoires et leurs effets sur la précision des simulations MC. Les objectifs dosimétriques seront traduits en fonction de coût et une méthodologie pour son optimisation sera établie. Les capacités d'optimisation de l'ITPS proposé seront évaluées avec des plans cliniques réels en utilisant les recommandations du rapport AAPM TG-137.

Dans le chapitre 3, après une brève introduction sur les aspects théoriques de la physique mécanique continue et de la modélisation numérique, on décrira le modèle biomécanique de l'œdème qui sera proposé. Une série d'expériences pour l'évaluation sera réalisée et permettra de comprendre les paramètres important du modèle et notamment de la place des valeurs d'élasticités des tissus dans la formation de l'œdème.

Le chapitre 4 sera le dernier chapitre méthodologique. Ce chapitre proposera une stratégie pour incorporer le modèle biomécanique de l'œdème dans le calcul dosimétrique de l'ITPS, notamment en introduisant un système de dosimétrie MC dynamique. La capacité de cette approche est de permettre la compensation des changements anatomique dans la dosimétrie. Elle sera étudier en comparant la dosimétrie peropératoire et post-opératoire en fonction de différents scénarios de création d'œdèmes. Un cas représentatif sera sélectionné pour démontrer la capacité de la stratégie proposée à produire des plans de traitement où la position des grains est compensée par la prédiction de l'œdème.

Pour terminer un dernier chapitre de discussion et de conclusion sera présenté. Il portera sur les résultats majeurs de cette thèse mais également sur les différentes approximations et par conséquent les divers points qu'ils restent à améliorer en tant que perspectives.

CHAPTER

2

MONTE CARLO INVERSE TREATMENT PLANNING ALGORITHM

A fast and efficient inverse treatment planning algorithm is presented. The fast simulated annealing is used as the optimization method. Dose calculations are performed based on GPU-accelerated Monte Carlo (MC) simulations using the GGEMS platform. The quality of the generated treatment plans is evaluated with the AAPM TG137 recommendations. Treatment plans are also compared with clinical plans of 18 patients. The DVH-based optimization outperforms in planning quality the clinical plans. Treatment plans of high quality can be produced in less than 1 minute providing MC dosimetric accuracy.

Un algorithme de planification de traitement inverse rapide et efficace est présenté dans ce chaptire. Le recuit simulé rapide est utilisé comme méthode d'optimisation. Les calculs de dose sont effectués par des simulations Monte Carlo (MC) accélérées sur GPU à l'aide de la plate-forme GGEMS. La qualité des plans de traitement générés a été évaluée avec les recommandations de l'AAPM TG137. Les plans de traitement obtenus ont été également comparés à ceux obtenus par le système clinique de 18 patients. L'optimisation basée sur l'histogramme du volume de dose est supérieure aux plans obtenus par le système clinique. Les plans de traitement obtenus par notre méthode sont produits en moins d'une minute.

"Well begun is half done."

— Aristotle

2.1 Inverse treatment planning algorithm overview

The quality of the LDR brachytherapy outcome depends strongly on the placement of the radioactive sources (seeds) in the prostate. Considering the anatomical constraints, such as the volume and size of the gland, and the procedure constraints that are introduced by the use of the 2D template guide for needle guiding and seeds' placement (see Figure 1.4), the number of available positions that a seed can occupy ranges between 200 and 600. During a typical implant, approximately 60-70 seeds are chosen to be delivered in specific locations, from the available 200-500 positions. The selected seeds' configuration (implant) should deliver the desired dose to the prostate while sparing the organs at risk (OARs). Achieving the specified dosimetric objectives is a matter of selecting the best combination of seed positions (optimal implant). In the minimum set-up of 200 available seed positions, the number of possible combinations for 60 seeds, C_{200}^{60}, can be calculated using the combinatoric formula

$$C_{200}^{60} = \frac{200!}{60!(200-60)!} \approx 7 \times 10^{51}. \tag{2.1}$$

Finding the optimal implant manually, out of this astronomical number of possible configurations, is impossible. Therefore, a satisfying implant rather than the optimal is selected based on the experience and the intuition of the clinician. Additionally, it is usually necessary to evaluate several implants until conclude, "hopefully", to the most satisfying one.

Alternatively to the manual implant selection, inverse treatment planning algorithms (presented in Subsection 1.4.3) aiming to the automatic prediction of the optimal implant have been proposed [Pouliot et al., 1996, Yang et al., 1998, and Guthier et al., 2015]. The introduction of inverse treatment planning algorithms in the clinical procedure improves the treatment's outcome and decreases the overall operation time. These algorithms are usually based on iterative methods in order to "explore" the large space of possible implants and eventually select the optimal (or near optimal) one.

The quality of an inverse treatment planning algorithm lies in its ability to achieve an optimal implant in the possible least time. Among the various proposed algorithms, simulated annealing (SA) is known as one of the most capable to achieve the global optimum implant and hence is widely used in inverse treatment planning systems, dedicated to various treatment procedures [Lessard and Pouliot, 2001, Webb, 1991, Martin et al., 2007, and Dai Kubicky et al., 2008]. As a result of the thermal fluctuations model (see Equation 1.9) of the SA metaheuristic, "worse" quality implants can be selected during the first iterations of SA avoiding, therefore, local minima "traps". The probability to select solutions of lower quality is decreasing as the system "cools down" and the algorithm is expected to eventually converge at the global optimum. The global optimum convergence of SA depends on the *cooling rate (CR)* of the algorithm. For standard SA the temperature for the j^{th} state is given by $T^j = \frac{T_0}{ln(j)}$ and leads to a big number of iterations until the algorithm cools down to the optimal solution.

Due to the increased computational cost, this cooling procedure is not applicable in an intraoperative environment, hence improved simulated annealing procedures have been introduced. These procedures follow a fast cooling schedule of the form $T^j = \frac{T_0}{j}$, where j is the j^{th} iteration and have already been applied successfully in LDR prostate brachytherapy [Pouliot et al., 1996]. The fast simulated annealing FSA of Pouliot et al. was able to produce treatment plans in 15 minutes on a `Sparc-5 SUN` workstation at the time of publication, however the FSA implementation in modern computer systems can converge to the optimal solution in

≈ 1 minute [D'Amours et al., 2011]. A novel approach in LDR brachytherapy optimization demonstrating interesting results was introduced recently by Guthier et al. [2015]. Guthier et al. proposed an inverse planning algorithm based on compressed sensing [Donoho, 2006]. The compressed sensing optimization algorithm presented by Guthier et al. is based on the sparsity of the seeds' configuration and was demonstrated that outperforms SA (x542 faster), while generating similar optimization results. However, this implementation is based on a greedy algorithm and its ability to overcome local minima traps was not investigated by the authors.

Despite the ability of an inverse planning optimizer to achieve the optimal implant, the quality of its result is as good as the explored solutions' space. While the various proposed inverse planning systems are focusing on the decrease of the optimization time, little has been done in the improvement of the accuracy during the generation of the configuration space to be explored. The previously proposed inverse treatment planning algorithms are based on the `AAPM TG-43` protocol recommendations (see Subsection 1.4.1) for the dosimetric evaluation of the possible configurations' space. Since the optimization procedure of the inverse planning algorithms is based on the evaluation of the dose deposited by the possible seeds' configurations, the generated optimal configuration of the optimizer is expected to be in reality sub-optimal, due to dosimetric errors introduced by the rough approximations of the `TG-43` protocol.

In an effort to develop a high-quality optimizer, a Monte Carlo inverse treatment planning algorithm (MC-ITPA) is proposed in this chapter. Similarly to previous work in HDR brachytherapy inverse planning [D'Amours et al., 2011], we evaluate the dose deposition of the possible seeds' configurations using Monte Carlo (MC) calculated dose kernels. Patient specific anatomy and tissue heterogeneities can, therefore, be accounted. In contrast to the method of D'Amours et al., the dose kernels are not precalculated using time-consuming conventional MC algorithms. We rather exploit the power of parallel processing on GPU.

We introduce `GGEMS` [Bert et al., 2013] - a GPU-accelerated Monte Carlo library - in the inverse treatment planning system. The fast MC dosimetry implementation of `GGEMS` enables the calculation of dose kernels in intraoperative acceptable times. Furthermore, the optimization of the seeds' configuration selection is based on an FSA implementation following the paradigm of Pouliot et al. [1996] since the alternative considered method of Guthier et al. lacks maturity at the current moment. The steps of the proposed MC-ITPA pipeline are listed below with a brief description:

1. Dose kernel generation — A dose deposition map is calculated for every possible seed position
2. Implant total dose — Accumulation of dose deposition maps of selected seeds forming the given implant
3. Optimal implant — Optimization of the implant using fast simulated annealing

2.1.1 GPU-accelerated Monte Carlo dosimetry

MC simulations are based on random sampling methods to numerically approach the solution to physical and mathematical problems that might be deterministic. Among many science fields, these simulations are used in particle physics to model accurately physical processes and

interactions between particles and matter. These methods find significant application in medical imaging and radiotherapy. Especially in radiotherapy applications, the MC simulations enable accurate dosimetry calculations during the treatment planning procedure [DeMarco, Solberg, and Smathers, 1998, Verhaegen and Seuntjens, 2003, and Flampouri et al., 2006].

However, an important drawback of the MC simulations is the associated high computational time that limits the full incorporation of the method in the routine clinical practice. A possible solution to reduce computational time of MC simulations is to exploit the implicit parallelism of the method. The MC simulation can be partitioned in sub-tasks and distributed in a computer cluster in order to decrease the simulation time. Unfortunately, this solution is difficult to be adopted within a routine clinical environment due to the high associated cost and logistic issues for the establishment and maintenance of a computer cluster (sufficient space, informatics infrastructures). Over the last decade, graphics processing units (GPUs) have become a low cost alternative solution for the acceleration of computationally demanding processes [Nickolls and Dally, 2010]. The GPU architecture is able to provide to any conventional computer the computation power of a small cluster. It has been shown that the use of GPU is the best way to decrease the computational cost of MC simulations [Lippuner and Elbakri, 2011, Hissoiny et al., 2011, and Jia et al., 2011].

GPU architecture

GPUs were initially designed for the processing and the interactive display of graphics in computers. Within this context the GPU architecture is conceived for computation intensive highly parallel execution. Exploiting their architecture, GPUs can be used as numerical computing engines, where numerical tasks are distributed over a large number of execution threads. The GPU hardware design differs from the CPU architecture. While in CPU the majority of transistors are devoted to data caching and flow control, in GPU architecture a high number of transitors is dedicated to data processing (see Figure 2.1). A GPU is organized in several streaming multiprocessors (SMs) each composed of numerous stream processors (SPs) that share control logic and cache. Most recent GPU architectures contain more than 2000 such streaming processors. Every SM manages a number of threads which are organized in blocks, with each thread representing a basic data element to be processed.

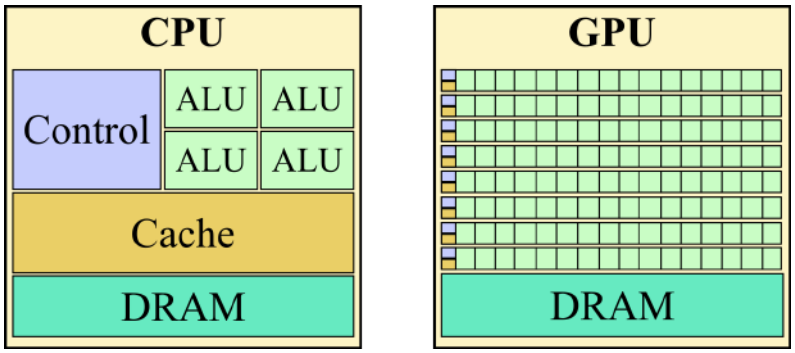

Figure 2.1 – GPU architecture. The majority of transistors in GPU architecture is dedicated to data processing providing ability for highly parallel computations, while in contrast the majority of transistor in CPU are devoted to data caching and flow control.

As a single instruction multiple data device, all threads of a GPU execute the same code, called kernel. Once a kernel is launched, the GPU architecture automatically schedules all blocks of threads on the different SMs. Each block assigned to a SM is subdivided into units called warps, which can be considered as the smallest executable unit of code. Recent GPU architectures have at least 32 SPs per SM, meaning that a SM processes a single instruction over all of the threads in a warp at a time. The capability to process warps in a parallel way over thousands of SPs sets the GPU a highly parallel computing device.

Multiple memory spaces are available from where threads may access data during their execution. Each thread has private local memory, while each block of threads has shared memory visible to all threads of a block. Local and shared memory provide quick access, however their size per block remains rather small (16–64 kB per block). In addition to local and share, all threads have access to the same global memory. This global memory is the largest one (up to 12 GB), and even it has a high latency compared to the local and shared memory, its bandwidth remains higher than the one provided by recent CPU processors (547.7 GBps for the latest `NVIDIA TITAN Xp` and only 34.1 GBps for an `Intel Core i7-7920HQ`).

Moreover, there are two additional read-only memory spaces, namely the constant and texture memory, accessible by all threads residing within the global memory but cached for efficient access. The constant memory, which is usually limited in size (<65 kB for recent NVIDIA GPU architectures) is often used for input variables, since their values can be accessed by all threads. On the other hand, texture memory is an alternative way to use cached data residing on the global memory, without the memory size limitation of the constant memory. For a more detailed description of GPU architectures the reader is referred to (Blythe 2008, Nickolls and Dally 2010).

Considering the implementation for MC simulations in GPUs, it has to be particularly adapted to perfectly fit the specifications and constraints of the GPU architecture. GGEMS library, is a Geant4-based MC simulation library for medical application using the CUDA paradigm, which allows harnessing in an efficient manner the power of recent GPU architectures.

GGEMS platform

The `GGEMS` platform (GPU GEant4-based Monte carlo Simulations, `http://ggems.fr`) is a toolkit for MC simulations in medical applications based on the extensively validated physics models of `Geant4` [Agostinelli et al., 2003]. The physics processes of the photoelectric phenomenon and Compton scattering from the standard model as such as the Rayleigh scattering from the Livermore model are implemented in GPU, based on the original `Geant4` implementation, without introducing any approximations [Bert et al., 2013, Bert, 2016].

The particle-emitting source is modeled by a phasespace file provided in the simulation process which can be generated by any other simulation toolkit such as `Geant4` or `GATE` [Jan et al., 2011, Sarrut et al., 2014]. Otherwise, if it is available, it can be retrieved by the `GGEMS` database. The use of phasespace files for modeling the particle-emitting source is adopted in order to avoid degradation of the simulation speed due to the analytical construction of source models with complicated shape, such as the ones found in brachytherapy procedures.

The particles emitted from the phasespace-modeled source are tracked in a voxelized phantom that represents the anatomy of the patient. In case that a CT image of the patient anatomy is provided, it can be used directly as the voxelized phantom by implicitly converting the electronic density of the CT image voxels to the corresponding materials using the `GGEMS` material

database. Therefore, voxel-level heterogeneities of the patient anatomy can be considered in the MC simulation.

In GGEMS plaform, in order to further decrease the simulation time, dose deposition recording using track length estimator (TLE) is implemented [Williamson, 1987], additionally to dose deposition recording based on the conventional analog estimator. In the case of the analog estimator, the dose delivered by a particle is expressed as the ratio of the energy deposited in a voxel of interaction and the mass of this voxel. However, in TLE the dose is recorded in all the traversed voxels by the given particle's trajectory. In this way, the desired statistical uncertainty can be obtained for a significantly lower number of simulated particles compared to the standard analog estimator.

Considering a LDR brachytherapy simulation were ^{125}I seeds are used, the statistical uncertainty in the prostate volume is $\approx 2\%$ for a GGEMS simulation using the TLE for 5×10^6 simulated particles. Under these conditions, a MC simulation of a LDR prostate brachytherapy treatment plan can be executed in $\approx 6s$ on a standard laptop equipped with a NVIDIA GEFORCE GTX 960M graphic card and in $\approx$ 2s on a workstation equipped with a NVIDIA GTX Titan X. The high accuracy of the resulting dose map and the low execution time provided by GGEMS platform sets it ideal to be used in the proposed MC-based inverse treatment planning algorithm (MC-ITPA).

2.1.2 Brachytherapy seed model in the proposed MC-ITPA

While in conventional inverse treatment planning algorithms (ITPA) based on the TG-43 recommendations the radiation sources are modeled as either point or linear sources, in our proposed MC-ITPA the full analytical model of the seed type used in our simulations is considered. All the undergone simulations during the development and validation of the MC-ITPA were done using the STM1251 (Bard Medical Division, Covington, GA, USA) seed model, as it is the seed type used in the Regional University Hospital Center (CHRU) of Brest, from where clinical data were provided for the validation of our developments.

The STM1251 seed is a cylindrical ^{125}I source of 4.5 mm length and 0.81 mm diameter [Kirov and Williamson, 2001]. The radioactive ^{125}I source has the form of a cylindrical coat embedded in a coaxial cylindrical geometry of seven layers of different material composition (see Figure 2.2).

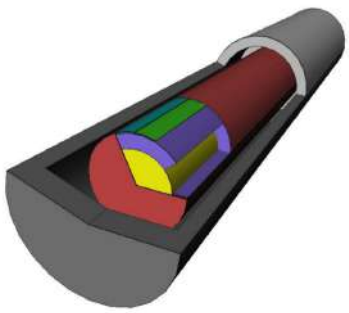

Figure 2.2 – STM1251 seed model. The STM1251 seed is a LDR ^{125}I emitting source and is composed of 7 coaxial cylindrical layers. Ordered from the inner to the outer, the seed consists of gold, aluminum, copper, iodine-125, nickel, air, and titan.

The core of the STM1251 seed is composed by gold ($Z_{Au} = 78$) and is 3.8 mm long with 0.36 mm diameter. As a result of its high atomic number, gold absorbs X-rays and hence, facilitates the localization of the seeds in fluoroscopic or tomographic imaging used for post-implant evaluation of the brachytherapy procedure.

The seed's gold core is covered by three layers of aluminum, copper, and nickel with similar length as the gold core and thickness of 0.15 mm, 1.9 μm, and 2.5 μm respectively. The role of these three layers is to provide chemical fixation between the gold core and the ^{125}I layer which is located between the copper and nickel layers and has a thickness of 17 nm. The external layer (4.5mm length, 0.81 mm diameter) is composed by titan and is separated from the coated core by a layer of air. Furthermore, the coated core is not spatially fixed and is in contact with the external titan shield due to gravity.

The STM1251 was previously modeled by Lemaréchal et al. [2015] and a phasespace file, where particle interactions within the seed's geometry are taken into account, is available in GGEMS phasespace database. The phasespace file of the described STM1251 seed is used in the simulations of the proposed MC-ITPA for the generation of single-seed dose maps for all the possible positions a seed can occupy in the prostate of a given patient. These single-seed dose maps are accumulated, in different combinations, to form the total dose maps for various implants which are evaluated by an optimization algorithm in order to provide the optimal implant.

2.1.3 Fast simulated annealing in LDR brachytherapy

Fast simulated annealing (FSA) is a version of simulated annealing (SA) with accelerated convergence towards the optimal solution in comparison with the classic SA. It is chosen as the optimization algorithm of the proposed MC-ITPA due to its maturity and extensive use in various, commercial and no, algorithms for the inverse treatment planning of several medical procedures [Oldham and Webb, 1995, Pouliot et al., 1996, Rowbottom, Nutting, and Webb, 2001, and Lahanas, Schreibmann, and Baltas, 2003]. FSA has been successfully implemented in the past [Pouliot et al., 1996] for the optimization of ^{125}I LDR prostate brachytherapy, demonstrating the capability to produce clinically acceptable treatment plans.

Because of computational power limitations at the time of implementation (1996), several approximations were considered. During the optimization procedure, the space of possible solutions was constrained by setting, manually, prior to the optimization, the desired needles' trajectories. In this way, the number of possible seeds' positions to be considered was limited to the number of seeds that correspond to the selected trajectories.

Furthermore, the objectives of the optimization were limited to maximum prostate dose coverage and sufficient dose uniformity, in order to avoid cold/hot spots, in the prostate interior. Restrictions for the dose delivered to the organs at risk (OARs) were not considered in the cost function

$$E(k) = \frac{f}{N}\sum_{i=1}^{N} H_i + W\frac{g}{M}\sum_{j=1}^{M} B_j, \tag{2.2}$$

but were rather controlled by the initial needles selection. In the above cost function (see Equation 2.2) $E(k)$ is an "energy-like" cost value at the k^{th} iteration. The optimal solution for the optimization objectives corresponds to the minimum cost value of the given function. The

optimization objectives are expressed in terms of the objective functions H_i and B_j, evaluated at the prostate contour points N and uniformity measurement points M which are located in the inter-space between the possible seeds' positions (see Figure 2.3). Finally, f and g are normalization factors and W is a weighting factor to control the contribution of the dose uniformity objective in the optimization process.

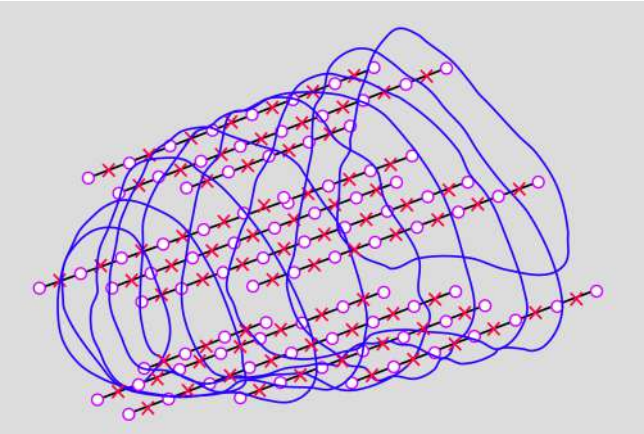

Figure 2.3 – Pouliot et al., [1996] cost function objectives. The maximum prostate dose coverage is measured on the prostate contour points (blue lines) and the dose uniformity on the uniformity measurement points (crosses) located between the possible seeds' locations (circles) on the available needle trajectories.

To accelerate the convergence of the algorithm towards the optimum solution, Pouliot et al. proposed an annealing schedule with an initial annealing temperature $T_{anneal} = 100$ and a cooling rate (CR) inversely proportional to the number of annealing iterations, $T_k = \frac{T_0}{k}$. Additionally, fast search of the seeds' configuration space was performed allowing for swapping two or even three seeds per annealing iteration. However, the applied CR was only admissible for small "jumps" in the search space, hence the simultaneous shift of two or three seeds, was allowed only with a 25% probability. Pouliot et al. were able to achieve optimal treatment plans in 15 minutes based on the `TG-43` dose formalism.

In our proposed implementation of FSA, prostate contour dose and prostate interior uniformity objectives, such as upper dose restriction objectives on both rectum and urethra, are considered in the cost function generation. Additionally, in contrast to the implementation of Pouliot et al., no manual input from the clinician is required during the needles' selection and the number of the needles to be used is treated as an additional objective of the cost function. The whole space of seeds' configurations is considered in our implementation. A dose map is precalculated using the MC method for each possible seed position for all the needle trajectories that penetrate the prostate.

Moreover, by introducing an optimized data structure we are able to achieve optimal solutions significantly faster for an annealing schedule with a few orders of magnitude higher initial temperature and a notably slower cooling rate. Furthermore, the search space exploration is limited to singe seed shifts improving the optimal solution convergence of the annealing procedure.

2.2 MC-ITPA development

While previously proposed inverse planning algorithms for LDR brachytherapy are based on the TG-43 dose calculation recommendations, our inverse planning algorithm uses MC-simulated dose calculation for high dosimetric accuracy. Even if, inverse planning algorithms based on MC dose kernels have previously been proposed [D'Amours et al., 2011], our development (according to our current knowledge) is the first to incorporate a fast GPU-accelerated MC dosimetry scheme in inverse planning with intra-operative acceptable computational time requirements. The combination of MC dosimetry with FSA enables the fast, fully automatic, optimization of the treatment planning procedure of LDR prostate brachytherapy.

2.2.1 MC-based seed dose map generation

MC simulations produce high accuracy dose maps that consider the heterogeneities in the patient's anatomy. In order to acquire a result of satisfying low statistical uncertainty, a great number of particles (10^9) must be generated during the simulation. This demand leads to a significant increase of the simulation's computational time and is the main reason that MC-based dosimetry is not yet fully integrated into the clinical routine.

In order to overcome this limitation of the MC-based dosimetry, we incorporated the GGEMS platform in our proposed MC-ITPA. Using GGEMS, the simulation time is dramatically decreased by exploiting GPU computational resources to track the interaction history of multiple particles inside a medium in parallel. Furthermore, the use of the TLE implementation provided by GGEMS enables the reduction of the number of particles required to acquire a statistical uncertainty of $\approx 2\%$ inside the prostate from 10^9 to 5×10^6 particles.

Even though MC simulation is fast using GGEMS, it can not be incorporated directly in any inverse planning algorithm of iterative nature, such as the fast simulated annealing. The dosimetric evaluation of several thousands of possible implants required by the FSA optimization algorithm is expected to result in long simulation times, not applicable in clinical routine.

This limitation is addressed by generating and storing in secondary memory (hard disk drive) single-seed dose maps for all the possible positions that a seed could occupy, instead of evaluating the dosimetry for various implants "on the fly", considering a realistic clinical setup (patient's anatomy, seed's geometry). The possible seed locations are retrieved with respect to all the possible needle trajectories available at the needle-guiding template grid (see Figure 2.4). Noticeably, candidates for dose map generation are seed occupying positions that are located only on needle trajectories penetrating the prostate gland.

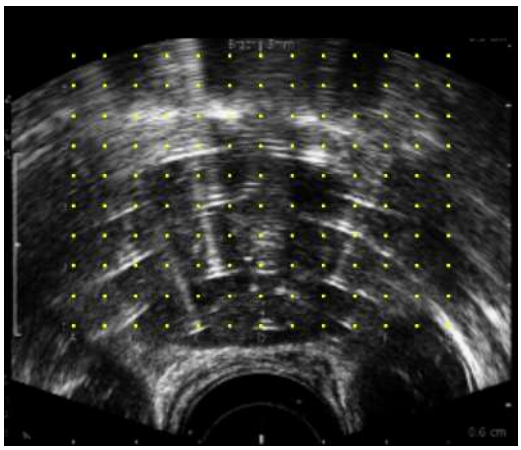

(a) Transperineal US image

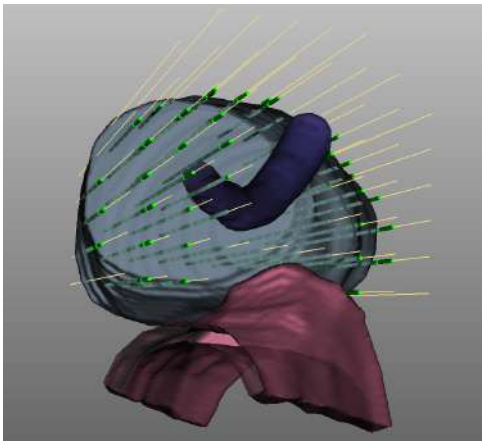

(b) 3D representation of possible seeds' positions

Figure 2.4 – Possible seed positions. The possible positions that seeds can occupy in a treatment plan are selected considering the needle positions, as given by the template guide. Needles that do not penetrate the prostate, or penetrate additionally an OAR (urethra or rectum) are not considered during the possible seeds' locations calculation.

The seed positions located on needle trajectories that are not penetrating the prostate and the ones on trajectories that penetrate, additionally to the prostate, an OAR (urethra or rectum) are discarded and no dose map is generated for them. By discarding seed positions that are expected to never be selected, we reduce significantly the search space of possible implants during the optimization process and, eventually, the necessary time to generate the single-seed dose maps.

In the inverse planning process, the generated dose maps will be retrieved and will be accumulated to generate the total dose map of the possible implants that will be evaluated during the optimization. While interactions between emitted particles from a seed with neighbor seeds can not be accounted with this approach (single-seed dose map generation), interactions within the seed are considered by using a phase-space to simulate the seeds (`STM1251` seed model) derived from `GGEMS` database. For the generation of the employed phasespace, MC simulations were executed considering an analytical model of the full geometry of the `STM1251` seed [Lemaréchal et al., 2015].

Moreover, heterogeneities between different underlying tissues are taken into account. For voxel-level heterogeneities consideration, a CT acquisition has to be available in order to convert the voxel electronic density to material composition, since such information is not available in the ultrasound image, used during treatment planning. The CT acquisition should be registered to the intra-operatively acquired US image using a dedicated registration algorithm.

However preoperative CT imaging is not part of the standard imaging protocol of LDR brachytherapy and is associated with additional exposure of the patient to ionizing radiation. On the other hand, according to the recommendations of the AAPM TG-186 [Beaulieu et al., 2012], computational phantoms can be generated by assigning materials with elemental composition, following the ICRU report No. 46 [Bethesda, 1992] and the recommendation of Woodard and White [1986], on the different labels of the segmentation image that is generated during the standard operation procedure by the clinician for the assessment of the size and shape of the prostate and OARs.

In the experimental validation of the MC-ITPA development, prostate is described by the material composition given in ICRU report No. 46 [Bethesda, 1992]. The material composition of the OARs is derived from the ICRP Publication No. 89 recommendations [Valentin, 2002] similarly to previous work [Oliveira et al., 2014]. The rest pubic tissue is modeled as an homogeneous soft tissue block (see Figure 2.5).

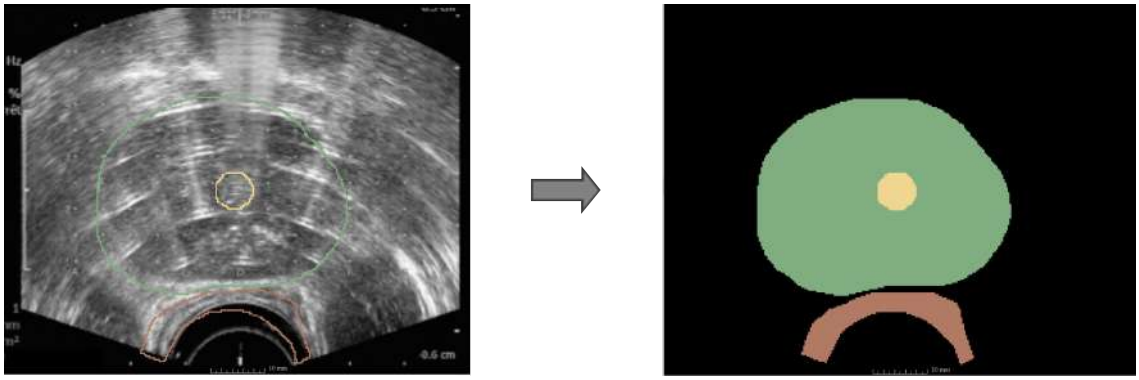

Figure 2.5 – US image conversion to computational phantom. According to the segmentation of the US image the prostate, the urethra, and the rectum are modeled following the material composition recommendations available in ICRU report No. 46 [Bethesda, 1992] and ICRP Publication No. 89 [Valentin, 2002]. An heterogeneous computational phantom for MC-based dosimetry is generated. The rest pubic structures are modeled as an homogeneous soft tissue with the corresponding material composition.

Materials' composition, as described by ICRU report No. 46 and ICRP Publication No. 89 recommendations, is expressed in terms of elemental mass fractions and mass density. A detailed description of the used materials' elemental composition is given in Table 2.1 below.

Table 2.1 – Material composition of the various materials present in the heterogeneous computational phantoms

Tissue	Elemental composition (% by mass)												Density
	H	C	N	O	Na	Mg	P	S	Cl	K	Ca	Zn	(g/cm^3)
prostate[a]	9.76	9.11	2.47	78.10	0.21	0.02	0.10	-	-	0.20	0.02	0.01	1.045
urethra [b,c]	10.45	23.22	2.49	63.02	0.11	0.01	0.14	0.20	0.14	0.20	0.02		1.000
rectum[b]	10.60	11.50	2.20	75.10	0.10	-	0.10	0.10	0.20	0.10	-	-	0.932
soft tissue[b]	10.45	23.22	2.49	63.02	0.11	0.01	0.14	0.20	0.14	0.20	0.02		1.000

[a] ICRU report No. 46 recommendations [Bethesda, 1992]
[b] ICRP Publication No. 89 recommendations [Valentin, 2002]
[c] Soft tissue composition is used.

In a typical treatment plan, for a given patient's anatomy, 400-600 possible seeds' positions are available. Corresponding single-seed dose maps of statistical uncertainty in the prostate of $\approx$ 2% can be generated in simulations of 5×10^6 emitted particles in $\approx$ 15-20 minutes ($\approx$ 2s per single-seed dose map) on the `NVIDIA GTX Titan X`. However, the $\approx$ 2% statistical uncertainty is desired only for the dose map of the final implant. The number of simulated particles during single-seed dose maps calculation, therefore, can be reduced. This will lead to single-seed dose maps with higher statistical uncertainty, however the desired uncertainty for

the final dose map of the implant is not affected. This is a result of the dose "hits" accumulation when the individual seed dose maps are added. Furthermore, the computational time is reduced since less emitted particles are simulated.

As an example, for a standard implant of 60 seeds, where all the seeds have the same activity, the emission of the simulated particles (5×10^6) is equally distributed at the available seeds of the given implant. As a result, the number of simulated particles per single-seed dose map can be divided by a factor of 60, achieving a significant acceleration during the single-seed dose map generation (15/20s for 400/600 single-seed dose maps). When these 60 dose maps are accumulated, the resulting total dose map is expected to have similar statistical uncertainty as if the dose map was produced by a complete simulation for the implant with 5×10^6 emitted particles.

With this approach, the computational time is greatly decreased, allowing for intra-operative MC dosimetry. In Table 2.2, the difference in the statistical uncertainty in the prostate for a dose map generated by a simulation for the total implant with 5×10^6 simulated particles and the corresponding dose map from the accumulation of the 60 single-seeds' dose maps simulated with 83334 particles, each, is demonstrated.

Table 2.2 – Comparison of the statistical uncertainty in the prostate between the total implant dose map generated by a complete MC simulation and generated by single-seed dose maps accumulation

Organ	Complete simulation	Single-seed dose map accumulation
prostate uncertainty	2.27 ± (0.16)%	2.29 ± (0.15)%

The presented results correspond to a 18 patients dataset. In complete simulations of the total seeds' configuration, 5×10^6 particles are simulated. In single-seed dose maps generation $5 \times 10^6/N$ particles are simulated where $N = 60$ is the number of the seeds in the total configuration.

As expected, the statistical uncertainty's difference between the two dose maps is very low (lower than the standard deviation) and hence MC-based dosimetry can be fully integrated in the clinical environment without significant computational overhead. Before continuing with the development of the optimization process of the MC-ITPA, the effect of the considered assumptions (number of simulated particles, material composition) on the dosimetric results should be evaluated.

2.2.2 Statistical uncertainty effect in MC-ITPA dosimetry

In order to reduce the statistical uncertainty of MC simulations the number of simulated particles should be increased at the cost of increased computational time. However to allow for the incorporation of MC simulations in clinical practice, the computation time should be reduced significantly. Nevertheless, an appropriate statistical uncertainty, usually $\approx 2\%$ is required to ensure accurate dosimetric results.

In our experiments, single-seed dose maps were generated using few thousands of particles ($\approx$ 60-80 $\times 10^3 particles$) exploiting the TLE implementation of the `GGEMS` platform. The

number of simulated particles was selected appropriately so that the generated dose map of the optimal implant should have the desired statistical uncertainty (≈ 2%) in the prostate. For this number of simulated particles, each single-seed dose maps was generated in ≈ 35 ms on the workstation (`NVIDIA GTX Titan X`).

In order to verify the dosimetric accuracy of simulations with 5×10^6 particles, their dosimetric results were compared with dosimetric results from simulations with 10^7 particles (≈ 1% statistical uncertainty in the prostate). Simulations were executed for three randomly selected patients from the MC-ITPA dataset. The percentage relative difference in the dose metrics between the simulations with 5×10^6 and 10^7 particles is demonstrated in Table 2.3.

Table 2.3 – Simulated particles number effect on the dose metrics. The percentage relative difference in the dose metrics for simulations with 10^7 particles (≈ 1% statistical uncertainty) against simulations with 5×10^6 particles (≈ 2% statistical uncertainty) is given.

Organ		10^7 p. vs 5×10^6 p. relative difference (%)
Prostate	V_{100}	0.04 ± (0.05)
	V_{150}	−0.11 ± (0.15)
	V_{200}	0.00 ± (0.00)
	D_{90}	0.02 ± (0.06)
Urethra	D_{10}	−0.74 ± (0.26)
	D_{30}	0.30 ± (0.15)%
Rectum	D_{2cc}	−0.03 ± (0.02)
	$D_{0.1cc}$	−1.46 ± (0.27)

Comparison between these simulations yielded negligible dosimetric differences in all criteria except than a low overestimation of the $D_{0.1cc}$ dose metric of 1.4% for the simulation with 5×10^6 particles. It is shown that the chosen number of simulated particles to achieve a ≈ 2% uncertainty was sufficient for the generation of dosimetric results of high accuracy.

2.2.3 Material composition effect in MC-ITPA dosimetry

Another important factor affecting the dosimetric accuracy of the MC simulation is the selection of the materials that are assigned to the corresponding tissues during the computational phantom generation. Heterogeneous phantoms can be constructed by assigning different material attributes to the segmented organs (see Figure 2.5). Using such phantoms the non-uniform dose distribution can be simulated with realism in contrast to homogeneous water-like phantoms such as the ones used in the `TG-43` dose formalism.

Similarly to the dose overestimation induced by the `TG-43` "water-phantom" assumption, the dose can be over or underestimated if not realistic materials are used in the simulation. To avoid such situation, appropriate materials should be selected. A more appropriate way to generate computational phantoms is by using the patient's CT image. This image can be directly converted in a computational phantom with voxel-level heterogeneity by converting the underlying Hounsfield units [Brooks, 1977] in the corresponding material values. While this approach enables the consideration of the complete heterogeneity pattern of the underlying tissues during the MC simulation, is only applicable if the patient's CT image is available.

Since pre-operative CT imaging is not part of the imaging protocol of LDR brachytherapy, it is of interest to investigate the dosimetric impact of computational phantoms derived from the segmentation image rather than the patient's CT image. Here, we investigate dosimetric differences between computational phantoms based on the ICRU report No. 46 and the ICRP Publication No. 89 recommendations (Comp. Ph.) and CT image derived phantoms (CT Ph.). The preoperative CT images, and the corresponding segmentation images, of the 5 patients available in the MC-ITPA database are used. MC simulations are executed using `GGEMS` with the TLE enabled with 5×10^6 simulated particles. Since the urethra was not segmented in the provided dataset the effect of the assumed material composition on the various dose metrics of interest was investigated only for the prostate and the rectum.

The relative dosimetric difference between the computational phantoms and CT phantoms is demonstrated in Table 2.4. A comparison with filtered CT image phantoms, after applying a Gaussian filter, is also considered in order to account for the effect of the statistical noise present in CT images.

Table 2.4 – Effect of the materials' composition on the dose metrics. Percentage relative difference of the various dose metrics between simulations performed with computational phantoms and CT derived phantoms (without or with statistical noise correction).

Organ		Comp. Ph. vs CT Ph. relative difference (%)	Comp. Ph. vs filtered CT Ph. relative difference (%)
Prostate	V_{100}	1.4 ± (0.8)	0.4 ± (0.2)
	V_{150}	6.8 ± (1.8)	2.4 ± (0.6)
	V_{200}	8.1 ± (0.4)	2.9 ± (0.7)
	D_{90}	6.5 ± (0.6)	1.8 ± (0.6)
Rectum	D_{2cc}	2.2 ± (3.0)	3.4 ± (4.7)
	$D_{0.1cc}$	−5 ± (7.2)	−2.2 ± (3.3)

It was demonstrated that the computational phantoms are overestimating the deposited dose in general. This results from not accounting the complete heterogeneity of the patient's tissue. However, the dose differences are reduced when the statistical noise is removed from the CT image. This shows that an initial image processing should be done on the CT images before used in MC dosimetry to avoid false heterogeneities.

It was found that the dose overestimation when computational phantoms are used is less than 5% compared to the filtered CT-derived phantoms for the given dataset. This allows the use of such computational phantoms for MC dosimetry when a CT image is not available. Nevertheless, CT-derived phantoms should be preferred as patient-specific heterogeneities such as calcifications can be considered, too. However image processing is admissible in order to reduce the statistical noise and improve the outcome.

2.2.4 Optimization process

Following the generation and storage of the single-seed dose maps for all the possible seed locations, the optimization process is initiated in order to retrieve the optimal implant that corresponds to the desired dose distribution in the area of interest. Due to the extensive use of the single-seed dose maps during this process, a data structure of dose vectors (*dectors*) is

extracted from the given single-seed dose maps. The dectors are loaded in primary memory once (initialization phase) and are used through the whole treatment planning optimization process. In this way, speed-down due to data latency (multiple access in secondary memory during single-seed dose map retrieval), is avoided.

Dectors construction

The goal of the optimization process, in order to acquire the optimal implant, is to achieve several dosimetric objectives. These objectives correspond to the dose preferences or restrictions on the treated region (prostate) and the proximal OARs (urethra and rectum). The dosimetric objectives are evaluated either on the corresponding organ's surface or internal points of the organ. The aim of the dosimetric evaluation on an organ's surface (contour) is to achieve a desired dose coverage for the whole organ, while on the other hand, the evaluation at internal points aims at achieving an adequate dose uniformity in the interior of the organ (avoid hot/cold dose spots).

Since only dose values recorded on the dose map's voxels that correspond to either the given organ's contour or internal points are required, the processing of millions of voxels available in the generated dose maps, is rendered useless. In order to avoid pointless data processing and reduce, therefore, the computational workload the *dector* data structure is constructed. Dose values stored in voxels that belong to the organ's contour or the selected internal points are extracted from the dose maps while the rest are discarded. This procedure is repeated for all the organs and corresponding optimization objectives. The generated dectors are expected to be of size given as

$$Size_{dector} = N_{voxels} \times M_{seeds}, \tag{2.3}$$

where N_{voxels} is the number of voxels that correspond to either the contour, or the internal organ points for the respective objective and M_{seeds} is the number of possible seeds for which the single-seed dose maps have been generated earlier. Additionally, the value N_{voxels} is stored in the relevant dector structure in order to enable the extraction of bunches of dose values (specific single-seed dose map contribution) later during the accumulation and evaluation of the seeds' configurations in the optimization procedure.

This procedure is based on the formation of a cost function, combining the several desired objectives. The arithmetic reduction of the cost function for various implants results to different cost values. By seeking the implant that leads to the minimum cost value, we can retrieve the optimal one according to the given objectives.

Cost function establishment

The cost function is the combination of all the desired optimization objectives in a single function. The target is to minimize the cost value, which is often interpreted as energy. The minimum cost value is the one that, ideally, satisfies all the optimization objectives. However, in many applications various objectives are competitive, meaning that they cannot be satisfied simultaneously.

Due to the rising complexity of the cost function, many local extrema are expected to be present in the function's solution space, therefore an algorithm able to explore the whole space sufficiently well and to avoid getting trapped in local extrema is necessary, in order to achieve

a global optimum. In LDR prostate brachytherapy inverse planning, several objectives with respect to the dose criteria for the different organs of interest are present in the cost function. In the proposed MC-ITPA, five objectives are considered in the cost function construction. The generated cost function is a weighted sum of the five objectives given as

$$CF = w_1 Obj_{pcd} + w_2 Obj_{pdu} + w_3 Obj_{ucd} + w_4 Obj_{rcd} + w_5 Obj_{nn}, \tag{2.4}$$

where Obj_{pcd} is the prostate's contour dose objective function, Obj_{pdu} defines the prostate's dose uniformity objective function, Obj_{ucd} refers to the urethra's contour dose objective function, Obj_{rcd} is the rectum's contour dose objective function, and finally Obj_{nn} is the objective function associated with the number of needles used in the treatment plan. The above objective functions are simulating specific dose preferences and restrictions at the various organs of interest, according to the clinical requirements.

Many of these criteria are competitive (e.g Obj_{pcd} and Obj_{rcd} cannot be satisfied simultaneously), therefore the importance of these criteria in the optimization is controlled implicitly, by the form of the mathematical expression describing the respective objective functions, and explicitly by the operator, with the adjustment of the weight factors $w_1 - w_5$ of the given objectives. The sum of the weight factors is equal to unity, hence the weight factors can be interpreted as the percentage of the contribution of the respective objective to the cost function.

Cost function objectives

In order to favor the satisfaction of specific objectives in a cost function constructed by competitive objectives, as the one presented above, mathematical expressions with steep gradient can be used. The term "steep gradient" refers to the magnitude of cost value changes in respect with variations of the objective's dose value from the given prescribed dose.

As an example, an objective with a quadratic relation between the cost and the dose produces higher cost values for a given dose variation than an objective with a linear relationship. Hence, the contribution of the former objective in the cost function is higher than the contribution of the latter. In the proposed development, different mathematical expressions are used for the description of the different objectives that form the cost function. Furthermore, all the objectives, except the one associated with the number of needles (Obj_{nn}), are expressed in terms of dose variations.

The cost of a given objective is expressed as the sum of the dose difference between the dose values recorded in the dectors and the respective dose prescriptions. This sum is normalized by the number of the contributing voxels to produce the final contribution of the objective in the total cost function value.

Prostate contour dose objective: The prostate's contour dose objective is considered the most important in the cost function generation of the MC-ITPA implementation. The main goal of LDR prostate brachytherapy is to deliver the higher possible dose to the cancerous region of the prostate. Usually, cancerous areas are spread all over the prostate tissue, therefore a minimum dose coverage of the whole prostate is required by current recommendations (`AAPM TG-137`).

In order to simulate this requirement, an asymmetric, dose restricting, objective function is established and evaluated on the contour voxels of the prostate. As a result of this unsymmetrical

behavior, lower doses than the desired are more penalized than higher doses. Considering the prescribed dose on the contour of the organ, the prostate's contour dose objective is set as

$$Obj_{pcd} = \frac{1}{N_{pc}} \sum_{i=1}^{N_{pc}} \frac{(D_i - D_{pc})^a}{D_i^b}, \tag{2.5}$$

where N_{pc} is the number of the prostate contour voxels (dose evaluation points), D_i is the dose deposited in the i^{th} contour voxel, D_{pc} defines the required dose value (prescribed by the clinician) and the exponents a, b are even numbers satisfying the condition $a > b$ used to control the slope of the two parts of the asymmetric objective function (see Figure 2.6a).

Prostate dose uniformity objective: Another restriction taken into consideration refers to the uniformity of the dose to be deposited in the prostate. The dose uniformity is an important factor that should be respected in order to avoid cold dose spots (regions receiving significantly lower dose than the desired), which are connected with cancer recurrence, and hot spots (regions receiving significantly higher dose than the desired), which are connected with increased toxicity.

This requirement is expressed using a symmetric dose restricting objective function (see Figure 2.6b), which is established and evaluated at measurement points located between the possible seed positions. The prostate's dose uniformity is, therefore, given as

$$Obj_{pdu} = \frac{1}{N_{pu}} \sum_{j=1}^{N_{pu}} (D_j - D_{pu})^c, \tag{2.6}$$

where N_{pu} defines the number of voxels where prostate's dose uniformity is evaluated, D_j is the dose value of the j^{th} prostate dose uniformity measurement voxel, D_{pu} defines the expected dose as it is prescribed by the clinician and the exponent c is an even number controlling the slope of the symmetrical objective function.

Urethra & rectum contour dose objective: Following the dose requirements for prostate dose coverage and uniformity, the dose received by the OARs is also required to satisfy specific criteria. In more detail, the dose received by the urethra and the rectum should not exceed the higher dose limits set by the corresponding dose recommendations.

The dosimetric restriction on the OARs is implemented here by a high dose restricting objective function (see Figure 2.6c). Since only a high dose limit exists for these organs, doses below the prescribed dose should have no contribution to the total cost function (zero cost). The dose restricting objective functions for the urethra and rectum are formed as

$$Obj_{ucd} = \frac{1}{N_{uc}} \sum_{k=0}^{N_{uc}} \Theta(D_k - D_{uc}) \cdot (D_k - D_{uc})^d \tag{2.7a}$$

$$Obj_{rcd} = \frac{1}{N_{rc}} \sum_{l=0}^{N_{rc}} \Theta(D_l - D_{rc}) \cdot (D_l - D_{rc})^e, \tag{2.7b}$$

where N_{uc} and N_{rc} define the number of contour voxels of the urethra and the rectum respectively, Θ expresses the Heaviside step function, D_k and D_l are the doses corresponding to the k^{th} and l^{th} contour voxels of the urethra and rectum respectively, D_{uc} and D_{rc} define the desired prescribed doses, and finally the exponents d,$e \in N$ are used to control explicitly the

slope and eventually the contribution of these objectives in the cost function. Usually, D_{uc} and D_{rc} are expected to be different for the two OARs.

Needles number objective: Another significant criterion is the number of needles used to deliver a given treatment plan. Since no recommendation about the number of needles to be used is given in `AAPM TG-137` report [Nath et al., 2009], it is up to the clinician's intuition to control this factor.

It should be noted that the insertion of a greater number of needles in the prostate is correlated with increased mechanical trauma which can lead to increased edema response. Edema reduces the quality of the treatment's outcome by cause of resulting seed migration from the original planned positions, therefore, treatment plans where a high number of needles is used are expected to have lower quality than those where edema is controlled.

To address this treatment plan quality criterion, an objective controlling the number of the needles to be used is introduced in the cost function. This objective has the simple form of

$$Obj_{nn} = k \times N_{needles}, \tag{2.8}$$

where the contribution of this objective in the cost function is proportional to the number of the used needles in the optimized treatment plan and is controlled explicitly by the multiplying factor k (see Figure 2.6d).

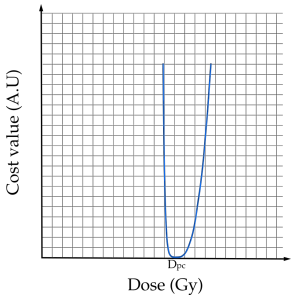

(a) Prostate contour dose objective (asymmetric)

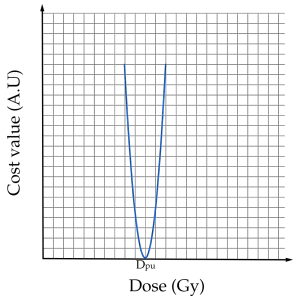

(b) Prostate uniformity objective (symmetric)

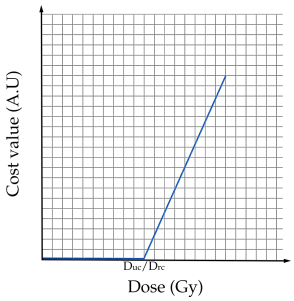

(c) OAR contour dose objective (linear)

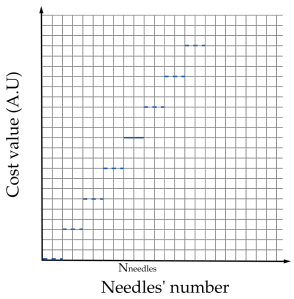

(d) Needles number control objective

Figure 2.6 – Cost function objectives. The various objectives controling the contribution of the prostate, organs at risk (OARs), and the number of needles can be parametrized by the clinician, adjusting the prescription parameters and weight factors. The "steepness" of the objectives' slopes can be controlled by the given exponents and the OAR contour dose objective can be converted in quadratic, using exponents > 1.

By introducing the objective functions described in Equations 2.5 - 2.8 in Equation 2.4, we derive the complete form of the cost function implemented in the proposed MC-ITPA given as

$$CF = w_1 \frac{1}{N_{pc}} \sum_{i=1}^{N_{pc}} \frac{(D_i - D_{pc})^a}{D_i^b} + w_2 \frac{1}{N_{pu}} \sum_{j=1}^{N_{pu}} (D_j - D_{pu})^c + w_3 \frac{1}{N_{uc}} \sum_{k=0}^{N_{uc}} \Theta(D_k - D_{uc}) \cdot (D_k - D_{uc})^d + w_4 \frac{1}{N_{rc}} \sum_{l=0}^{N_{rc}} \Theta(D_l - D_{rc}) \cdot (D_l - D_{rc})^e + w_5 k \times N_{needles}. \tag{2.9}$$

Minimizing this cost function, the optimal seeds' configuration with respect to the prescribed doses on the different objectives can be retrieved. By modifying the weight factors w_1 - w_5 and the exponents a, b, c, different implants can be achieved that favor selected criteria. In order to explore the space of the different available solutions of the presented cost function effectively, the fast simulated annealing (FSA) is implemented.

Core of the optimization procedure

FSA is chosen as the optimization method of the proposed MC-ITPA due to its previously successful application in inverse planning algorithms [Oldham and Webb, 1995, Pouliot et al., 1996, Rowbottom, Nutting, and Webb, 2001, and Lahanas, Schreibmann, and Baltas, 2003]. Adjustments on FSA have been done as seen appropriate in order to introduce the dector structures in the algorithm's implementation and are described below.

Prior to the optimization of the implant, the number of seeds to be used in the treatment plan must be estimated to adjust the number of the simulated particles per single-seed dose map. This input can be determined either manually by the clinician, or implicitly by the MC-ITPA algorithm based on the empirical formula introduced by Pouliot et al. [1996] in which the number of seeds to be used is given by

$$N_{seeds} = 4 + \frac{4.674 \times V^{0.562}}{A}, \tag{2.10}$$

where V defines the volume of the prostate expressed in cm^3 and A is the activity per seed expressed in mCi.

During the optimization process, according to the given number of seeds to be used, an initial implant is set by occupying N_{seeds} random positions from the available possible seeds' positions. All the possible seeds' positions are implicitly numbered and the indices of the initially selected seeds are used as an offset in the processing of the dector structures in order to extract the dose contribution of the given seed to the organs of interest (see Figure 2.7).

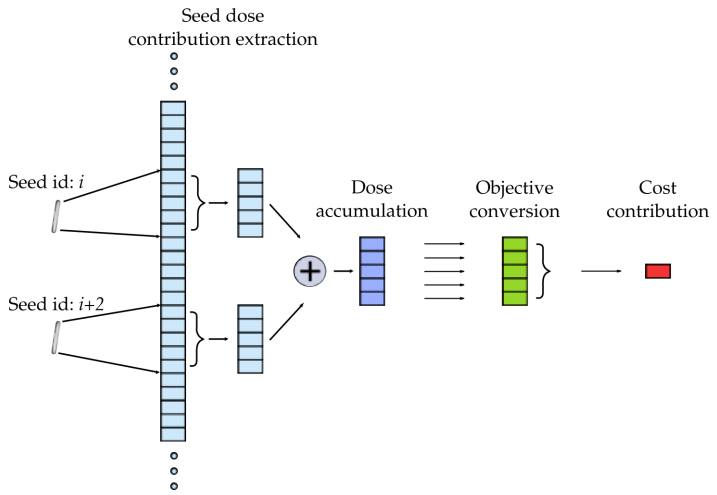

Figure 2.7 – Initial seeds' configuration's cost. Given the indices of the seeds selected in the initial implant, the respective dose values are extracted from the dector structures and accumulated in the total dose vector. This vector is converted in the objective function and the total contribution in the cost is calculated.

Once the dose contributions of each seed are extracted from the dectors, they are accumulated in vectors (1-D matrices) representing the total dose deposited in the voxels of the areas of interest for the given seeds' configuration.

The accumulated dose vectors are processed according to Equations 2.5 - 2.7 to generate the objective functions which subsequently are combined with the needles number objective function to form the initial value of the total cost function (see Equation 2.9).

Afterwards, with respect to the given initial annealing temperature (T) and cooling rate (CR), a number of iterations will be performed in the FSA algorithm, where in each iteration the initial implant will be modified by randomly selecting one seed (from the ones in use) to be discarded and a new (from the previously not used seeds) to be added, in order to form a new implant (see Figure 2.8).

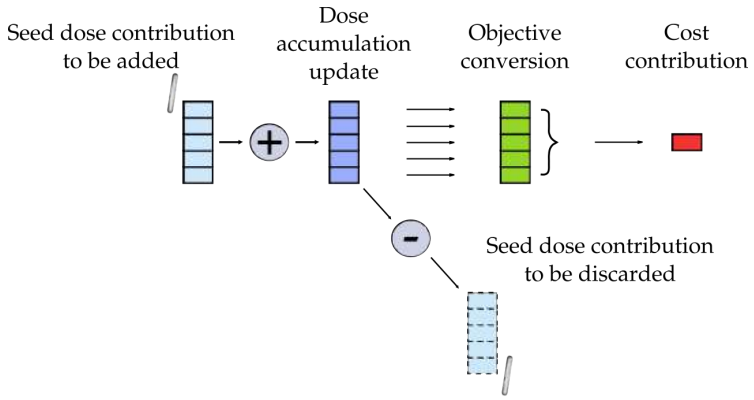

Figure 2.8 – Implant cost update by seed swapping. During each iteration of the FSA algorithm, a new seed is added in the current implant and a previously used seed is discarded. After this seed swapping, the total accumulated dose vector is updated and the new cost value is calculated.

According to this seed "swapping", the dose contribution of the discarded seed in the accumulated dose vector will be subtracted and the dose contribution of the newly added seed will be accumulated. The updated accumulated dose vectors will be used to update the objective functions and calculate the updated value of the cost function.

During the FSA process, each update of the implant is accepted as "better" if the associated cost value is lower than the cost value of the previous implant. If the cost value is higher, the new implant is accepted with a probability $P(\Delta E)$ given as

$$P(\Delta E) = e^{\frac{-\Delta E}{T(k)}}, \tag{2.11}$$

where $\Delta E = E' - E$ is the difference of the updated implant cost (E') and the previous cost of the previous one (E). $T(k) = T(k-1) \times (1 - CR)$ defines the annealing temperature of the k^{th} iteration in relation to the annealing temperature of the previous iteration and the cooling rate (CR) which get values from the interval $(0, 1]$.

The probability $P(\Delta E)$ tends to unity for high values of annealing temperature (worse configuration acceptance) and to zero when the annealing temperature is low (worse configuration rejection). This probabilistic acceptance of lower quality implants enables the algorithm to avoid being trapped in local minima during the first iterations when the annealing temperature is high. After a big number of iterations, when the annealing temperature has been lowered, it is expected to converge towards the global optimum since only better implants will be admissible then. The process of FSA, as was implemented in the proposed MC-ITPA, is given in the pseudo-code snippet in Appendix B.

The acceptance probability of lower quality implants depends on the given value of the initial annealing temperature and the selected cooling rate. For high initial annealing temperature and considerably slow cooling rate, the algorithm is capable of exploring the solution space efficiently and escaping local minima. In contrast, for a low initial temperature and a high cooling rate, implants of worse quality are early rejected and the algorithm is more keen to be trapped in local minima, while for zero initial temperature the algorithm transforms to greedy (worse implants are never accepted).

The initial annealing temperature value and the cooling rate affect also the speed of the algorithm to converge to the final solution, since for a slower cooling scheme the algorithm tends to be slower by executing more iterations until reaching convergence. The trade-off between computation time and outcome's quality must be considered by the operator, taking into account the constraints of the given clinical setup.

The capabilities of the proposed MC-ITPA algorithm to produce efficiently clinically accepted treatment plans can be evaluated by its ability to generate treatment plans that respect the current dose recommendations, such as the ones recommended by the `AAPM TG-137` report [Nath et al., 2009].

As those recommendations may not always be satisfied under realistic clinical conditions (anatomic-related restrictions in seeds delivery), a comparison between treatment plans produced from the proposed MC-ITPA and clinical plans delivered to real patients will be considered in the evaluation of the planning capabilities of our development, following below.

2.3 MC-ITPA validation process

The capability of an inverse treatment planning system to produce implants of good quality should be evaluated by means of clinical dose recommendations and clinical practice setup. For the validation of the proposed MC-ITPA a database of 18 patients, that have undergone LDR prostate brachytherapy as monotherapy in the CHRU of Brest, was used.

The first objective was to investigate the ability of the MC-ITPA to produce treatment plans that satisfy the AAPM TG-137 recommended dose restrictions. Due to the competitive nature of these dose restrictions, the generation of a treatment plan that satisfies all of them simultaneously is challenging and, therefore, the AAPM TG-137 recommendations satisfaction is a good quality measure for the evaluation of the algorithm under general conditions.

The second objective of this validation was to evaluate the ability of the algorithm to produce treatment plans with dosimetric outcome comparable to that of real clinical treatment plans, that were delivered to patients in CHRU Brest. In this way, the response of the proposed algorithm under realistic clinical conditions was investigated.

2.3.1 Patients database for MC-ITPA validation

The patients' database used for the validation of the MC-ITPA development was created by retrieving treatment plans delivered to 18 patients in CHRU of Brest. These treatment plans were retrieved from the VariSeed™ v9.0 LDR treatment planning system of CHRU Brest.

The final database was composed of 18 files where the planned seeds' positions, approved by the clinician for implantation, were recorded. Complementary the intra-operative US images, after the insertion of the peripheral needles, and the post-implant CT images of the 18 patients were acquired.

In addition, pre-operative CT images were available for 5 out of the 18 patients and were included in the database. In all the collected intra-operative US images the contours of the prostate (clinical target volume - CTV), of the urethra, and the rectum were available.

Prior to use, all the patient datasets were anonymized in respect to the confidentiality of the acquired clinical data. The database was named "MC-ITPA database" and was used in the evaluation phase of the MC-ITPA.

2.3.2 MC-ITPA evaluation

The first objective of the *MC-ITPA evaluation* was the investigation of the algorithm's ability to produce treatment plans that respect the AAPM TG-137 dosimetric recommendations [Nath et al., 2009]. These recommendations, initially introduced by PROBATE group of GEC ESTRO [Salembier et al., 2007], aim to the standardization of certain planning parameters in order to assist in the understanding of arising differences in outcome, morbidity, and post-implant dosimetry. In a brief review the planning recommendations consider the clinical target volume (CTV), which in the case of brachytherapy is the whole prostate gland, the urethra, and the rectum.

Prostate planning criteria are:

I. $V_{100} > 95\%$ of CTV. That means that the V_{100}, the percentage of the CTV that receives at least the prescribed dose, must be at least 95%.

II. $V_{150} \leq 50\%$ of CTV. Which translates into the V_{150}, the percentage of the CTV that receives at least 150% of the prescription dose, should be equal to or less than 50%.

III. $V_{200} \leq 20\%$ of CTV. Which express the requirement that V_{200}, the percentage of the CTV that receives at least 200% of the prescription dose, should be equal to or less than 20%.

As a result of the V_{100} criterion the D_{90}, the dose that covers 90% of the CTV, will be larger than the prescription dose. In the following, the criteria for the organs at risk (OARs) are given

Urethra planning criteria are:

I. $D_{10} < 150\%$ of the prescribed dose.

II. $D_{30} < 130\%$ of the prescribed dose.

Rectum planning criteria are:

I. $D_{2cc} < 100\%$ of the prescribed dose.

II. $D_{0.1cc}(D_{max}) < 150\%$ of the prescribed dose.

The urethra D_{10} and the rectum D_{2cc} are the primary planning criteria, while the urethra D_{30} and the rectum $D_{0.1cc}$ are considered secondary. The prescribed dose, intended dose for the 100% isodose, for ^{125}I LDR brachytherapy according to `AAPM TG-137` is $145Gy$ and is the prescribed dose value that was used in our experimentations. For the prescription dose of $145Gy$, the numerical values of the planning criteria are summarized in the following table (Table 2.5).

Table 2.5 – AAPM TG-137 planning criteria for prescribed dose (D_{presc}) 145 Gy.

Organ	V_{100}	V_{150}	D_{90}	D_{30}	D_{10}	D_{2cc}	$D_{0.1cc}$
prostate	$> 95\%$	$\leq 50\%$	> 145.0	-	-	-	-
urethra	-	-	-	< 188.5	< 217.5	-	-
rectum	-	-	-	-	-	< 145.0	< 217.5

MC-ITPA vs AAPM TG-137 recommendations

The capability of an inverse treatment planning algorithm to meet the planning criteria of `AAPM TG-137` recommendations depends on the chosen cost function to be minimized. The cost function implemented in the proposed MC-ITPA (see Equation 2.9) provides the flexibility to achieve the desired planning criteria by modifying the expected dose prescriptions, the objective functions' weight factors, and their respective exponents.

For a given combination of the cost function's parameters, the optimal seeds' configuration is acquired by minimizing the employed cost function. The final accomplishment of the

planning criteria (various dose metrics on CTV and OARs) depends strongly on the selection of these parameters.

The intra-operative US image of a randomly selected patient from the MC-ITPA database was used and treatment plans were generated for various parameter combinations. The number of seeds to be used during treatment planning was implicitly calculated by the MC-ITPA algorithm. A possible combination of cost function parameters that satisfied adequately the AAPM TG-137 planning criteria was chosen (see Table 2.6). The resulting dose metrics for the CTV and the OARs are shown in Table 2.7.

Table 2.6 – Cost function parameters set-up to achieve the AAPM TG-137 planning criteria for one patient.

Organ	Prescriptions					
Prostate	D_{pc}	a	b	D_{uc}	c	w_2
	380	4	2	230	2	0.05
Urethra	D_{uc}		d		w_3	
	140		3		0.04	
Rectum	D_{rc}		e		w_4	
	250		3		0.04	
Needles	k			w_5		
	80000			0.06		
Prescribed Dose	$145Gy$					

Modification of the selected parameters leads to plans with different dosimetric outcome. By fine-tuning the given parameters, high-quality treatment plans can be achieved.

Table 2.7 – Dosimetric results of a treatment plan generated with cost function parameters as given in Table 2.6

Organ	Metrics		
Prostate	$V_{100}(\%)$	$V_{150}(\%)$	$D_{90}(Gy)$
	95.6	49.7	160.4
Urethra	$D_{10}(Gy)$		$D_{30}(Gy)$
	207.8		186.4
Rectum	$D_{2cc}(Gy)$		$D_{0.1cc}(Gy)$
	118.0		187.4

Dosimetric criteria as given by AAPM TG-137 are met. 17 needles are required for the delivery of the given plan rendering it admissible for clinical application.

For the chosen cost function parameters all the AAPM TG-137 planning criteria were satisfied successfully showing the ability of the algorithm to produce high quality treatment plans. In addition, 17 needles were selected in the generated implant, demonstrating the clinical applicability of the treatment plan. The MC-ITPA was able to generate realistic treatment plans where the dosimetric outcome was controlled by the input parameters selected by the

operator. Different combinations of the input parameters result to treatment plans with different dosimetric outcome, therefore, the effect of these parameters on the optimization procedure should be investigated.

Effect of dose prescriptions' variation on optimization

During the optimization, the resulting treatment plan depends on specific dose prescriptions for the various organs (optimization parameters) given by the operator as input to the algorithm. The effect of the variation of these parameters on the optimization's outcome is of great interest. Considering the selected values in Table 2.6, the effect of the variation of each individual parameter is investigated. Maintaining all the other parameters constant, a single dose prescription parameter is modified in a range of dose values between 0 to 500 Gy and the resulting dosimetric changes are studied.

The effect of the variation of each prescribed dose parameter on the prostate's contour, the prostate's interior, and the contours of the OARs is presented in Figures 2.9 - 2.12 respectively. In these figures, the variation of the dose metrics of interest in relation to the variation of the respective parameter is demonstrated.

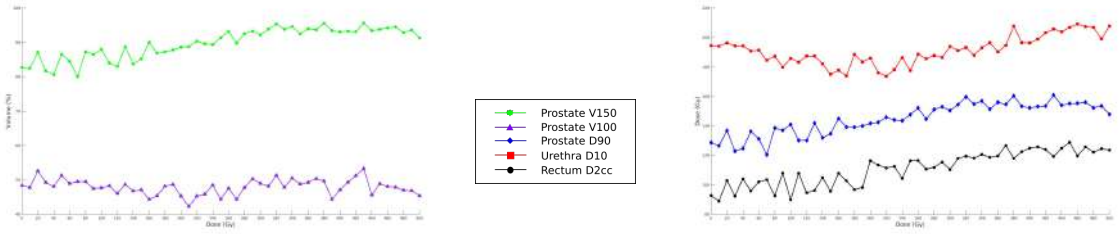

(a) Volume coverage metrics (b) Dose coverage metrics

Figure 2.9 – Prostate contour-dose-prescription variation

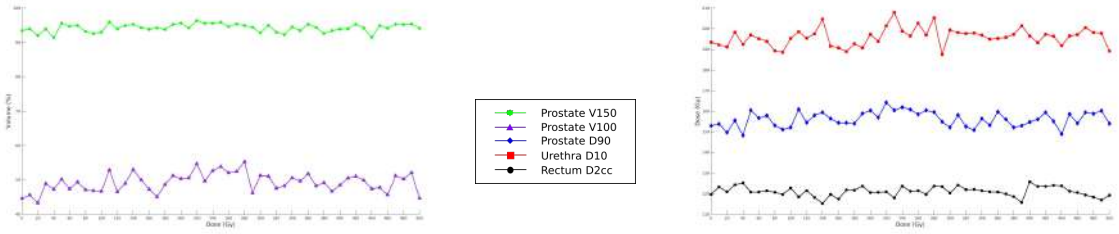

(a) Volume coverage metrics (b) Dose coverage metrics

Figure 2.10 – Prostate uniformity-dose-prescription variation

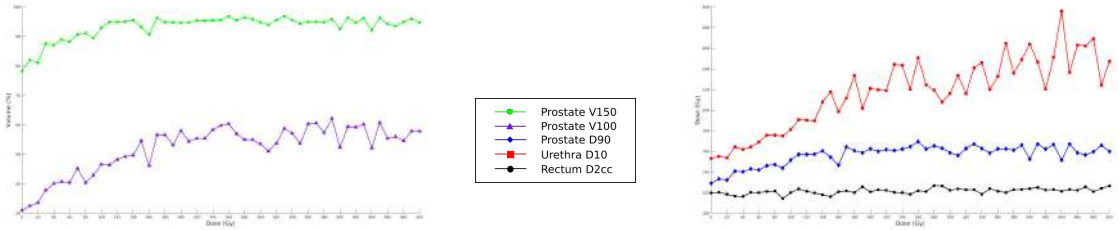

(a) Volume coverage metrics (b) Dose coverage metrics

Figure 2.11 – Urethra contour-dose-prescription variation

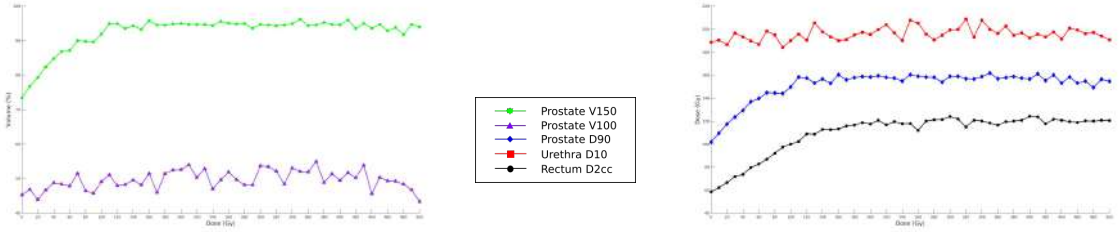

(a) Volume coverage metrics (b) Dose coverage metrics

Figure 2.12 – Rectum contour-dose-prescription variation

As shown in the results demonstrated in Figures 2.9 - 2.12, the increase of the prostate's contour prescribed dose leads to an increase of the overall dose delivered to the prostate (V_{100}, D_{90}) and the OARs (D_{10}, D_{2cc}). However, the prostate's dose uniformity (V_{150}) is not affected. On the other hand, the variation of the prostate's dose uniformity parameter, did not seem to affect significantly any of the investigated dose metrics, for the given optimization parameters setup.

Considering changes in OARs' dose prescription parameters, their variation showed a proportional relationship with variations on the corresponding dose metrics (D_{10} for the urethra optimization parameter and D_{2cc} for the rectum's parameter). Moreover, variations on the urethra prescribed dose resulted to a proportional increase of the prostate's V_{150} dose metric, and similarly variations of the rectum's prescribed dose led to a proportional increase of the prostate's V_{100} and D_{90}. These last findings demonstrate that the satisfaction of the maximum prostate dose coverage objective is opposed to the rectum sparring objective. Furthermore, urethra's hot/cold spots are associated with prostate's hot/cold spots in the deposited dose distribution.

This experiment aimed to demonstrate the general relationship between the various optimization objectives and the effect of their variation in the overall dose distribution. An extensive investigation of these relationships requires the investigation of the variations on various parameters' configurations. Nevertheless, the sensibility of the optimization algorithm to modifications of the OARs' planning criteria was demonstrated. This sensibility is ensured by the choice of high exponents in the OARs' objective functions (see Table 2.6) that results in steep cost gradients and strong contribution in the cost function. On the other hand, if low exponents are chosen for the OARs' objective functions then the sensibility is decreased and the quality of the optimization outcome cannot be ensured.

Annealing parameters effect on optimization convergence

The optimization result of the FSA algorithm, similarly to the other simulated annealing variations, depends strongly on the selected annealing temperature (T) and cooling rate (CR). These two variables control the acceptance probability (see Equation 2.11), and hence the ability of the algorithm to avoid getting trapped in local minima. When T is high the probability to accept a lower quality solution increases, therefore, the possibility to avoid local minima "traps" increases, too. For a high value of initial T and a significantly low CR, the FSA will follow a slow cooling procedure and a bigger range of the solution space will be explored, leading to the convergence at a better final solution.

On the other hand, the combination of a very high initial T and a very low CR leads to increased computational time and a trade-off between the solution's quality and the computational time must be done. In the previous validation process of the MC-ITPA against the `TG-137` recommendations and in the following validation process against the clinical treatment plans, the initial T was set at 10^5 and the chosen CR was 0.2%. For this setup the MC-ITPA was able to converge to the minimum possible cost function value in 0.8s using an `Intel Core i7 4720HQ` processor.

In order to ensure the appropriateness of the selected parameters' values, a series of tests were executed where T was modified in a range from 1 to 10^6 while the CR was held constant to 0.2% to study the dependence of the algorithm's convergence on the annealing temperature (see Figure 2.13). An additional series of tests, where now the initial T was held constant at 10^5 and the CR was modified in the range of 0.01% to 20% was executed to investigate the dependence of the solution's quality on the selected cooling rate (see Figure 2.14).

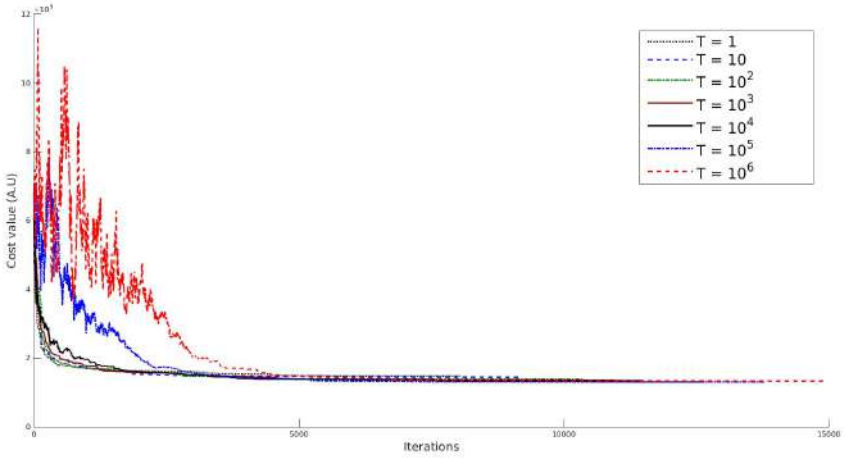

Figure 2.13 – FSA convergence dependence on temperature. For increasing temperature, FSA algorithm explores more efficiently the solution space by accepting worse solutions initially. Convergence to better solutions is achieved for higher temperature.

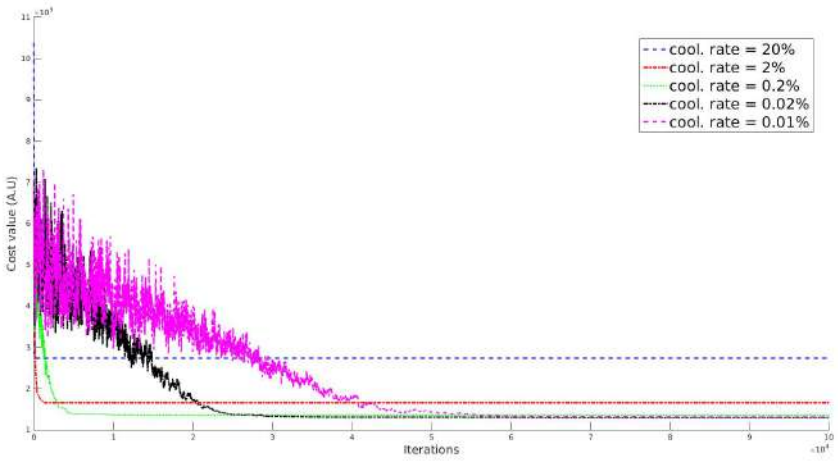

Figure 2.14 – FSA convergence dependence on cooling rate. The convergence of FSA algorithm has a stronger dependence on the cooling rate (CR) than the temperature. For not sufficiently low CR, the algorithm is trapped in local minima. However, very low CR can make the algorithm slow. It is shown that $CR = 0.2\%$ is a very good comprimise between solution quality and computational time.

In figures 2.13 and 2.14, it is shown that the MC-ITPA convergence is depended more strongly on the selected cooling rate, rather than the temperature (given a sufficiently low cooling rate is selected). As demonstrated in Figure 2.13, for T = 10^5 the exploration of the solution space is sufficiently large and convergence to a similar cost value as for T = 10^6 can be achieved. For lower temperatures the solution space exploration is limited, however not significant degradation to the cost convergence is observed.

On the contrary, variations of the cooling rate affect strongly the algorithm's convergence, where for high cooling rates (20%, 2%) the algorithm converges to worse solutions with higher cost values. For high cooling rates, the annealing temperature decreases fast during the first iterations and the algorithm performs similarly to a greedy algorithm. The 0.2% cooling rate provides sufficient solution space exploration and convergence to similar cost value as for lower cooling rates (0.02%, 0.01%) but at least $\times 10$ times faster.

The optimization process of the MC-ITPA, as demonstrated, can provide solutions of high quality in less than 1 second and therefore satisfies the clinical time requirements providing real-time optimization.

MC-ITPA vs Clinician's treatment plan

Having proved the ability of the proposed MC-ITPA algorithm to generate treatment plans that satisfy the `AAPM TG-137` planning criteria, the next objective of the validation process was to test its ability to produce treatment plans comparable to those applied in real clinical environment situations.

In this experiment, the clinical treatment plans delivered to 18 patients were compared to the corresponding treatment plans generated by the MC-ITPA in terms of the dosimetric criteria satisfaction. The clinical treatment plans were delivered to the patients using the `VariSeed`$^{\text{TM}}$ `v9.0` LDR treatment planning system of CHRU Brest. In the real clinical procedure, an initial

treatment plan was generated using the optimization algorithm available in VariSeed™ v9.0 in 1 minute. Following, the generated treatment plan was modified manually by the clinician for a time period of 15-20 minutes until the treatment plan met all the desired dosimetric criteria prior to its delivery to the patient.

These treatment plans were reproduced with MC simulation using the GGEMS platform, the MC dosimetry engine, of the MC-ITPA algorithm. In this way, dosimetric differences between clinical and MC-ITPA plans, related to the chosen dosimetric formalism, were eliminated. In the MC simulations of the clinical treatment plans 5×10^6 particles were simulated using the track length estimator (TLE) in order to generate dose maps of similar statistical uncertainty to those generated by the MC-ITPA.

For all the available patients, treatment plans of comparable quality to the clinical treatment plans were generated using the MC-ITPA. The planning criteria of MC-ITPA were adjusted manually for each patient in order to generate treatment plans that meet the desired dosimetric criteria while a number of seeds and needles is used, similar to the ones used in the clinical plans.

The mean values of the various considered dosimetric criteria, with their standard deviation, for the MC-simulated clinical plans and the MC-ITPA treatment plans are demonstrated in Table 2.8, while individual values are reported in Appendix C, Table C.1.

Table 2.8 – Dose metrics comparison between clinical plans (simulated with MC) and MC-ITPA generated plans. Mean dose metrics' values with their standard deviation are presented. The percentage relative difference between the MC-ITPA and the clinical plans is given.

Organ		Clinical plan (MC)	MC-ITPA plan	Rel. difference (%)
Prostate	$V_{100}(\%)$	94.7 ± (2.3)	95.8 ± (1.1)	1.2
	$V_{150}(\%)$	44.8 ± (4.8)	51.3 ± (3.0)	14.5
	$V_{200}(\%)$	18.9 ± (2.5)	25.4 ± (4.0)	34.4
	$D_{90}(Gy)$	156.7 ± (6.4)	161.5 ± (4.6)	3.1
Urethra	$D_{10}(Gy)$	172.7 ± (8.9)	178.8 ± (15.7)	3.5
	$D_{30}(Gy)$	159.7 ± (5.7)	165.4 ± (11.8)	3.6
Rectum	$D_{2cc}(Gy)$	108.1 ± (10.9)	114.4 ± (9.0)	5.8
	$D_{0.1cc}(Gy)$	153.6 ± (15.7)	167.8 ± (16.0)	9.2
Seeds		64 ± 7	64 ± 5	0.0
Needles		18 ± 2	16 ± 2	−11.1

Clinical plans are simulated using MC and considering the tissue heterogeneities similarly to MC-ITPA dosimetry. In this way dosimetric differences depend only on the selected seeds' configurations.

For all the considered patients, the MC-ITPA treatment plans demonstrated better dosimetric quality than the simulated clinical plans. The majority of the dosimetric recommendations were met in all cases in the MC-ITPA plans. However, the dose homogeneity in the prostate was not completely satisfied where V_{150} was found 1.3% higher than the upper limit. Similarly, the V_{200} metric was 5.4% higher than the recommended limit.

The treatment plans generated by the MC-ITPA comprised the same number of seeds as the clinical plans but 10.5% fewer needles were used in average. This is a finding of great

importance, since it demonstrates that good quality treatment plans can be produced by the proposed algorithm using fewer needles and hence, reducing the associated trauma which is directly related to the formation of edema, a quality decreasing factor of the treatment to be delivered.

The overall superior dosimetric quality of the MC-ITPA-generated treatment plans over the simulated clinical plans is visible in the graphical representation of the respective dose-volume histograms (see Figure 2.15).

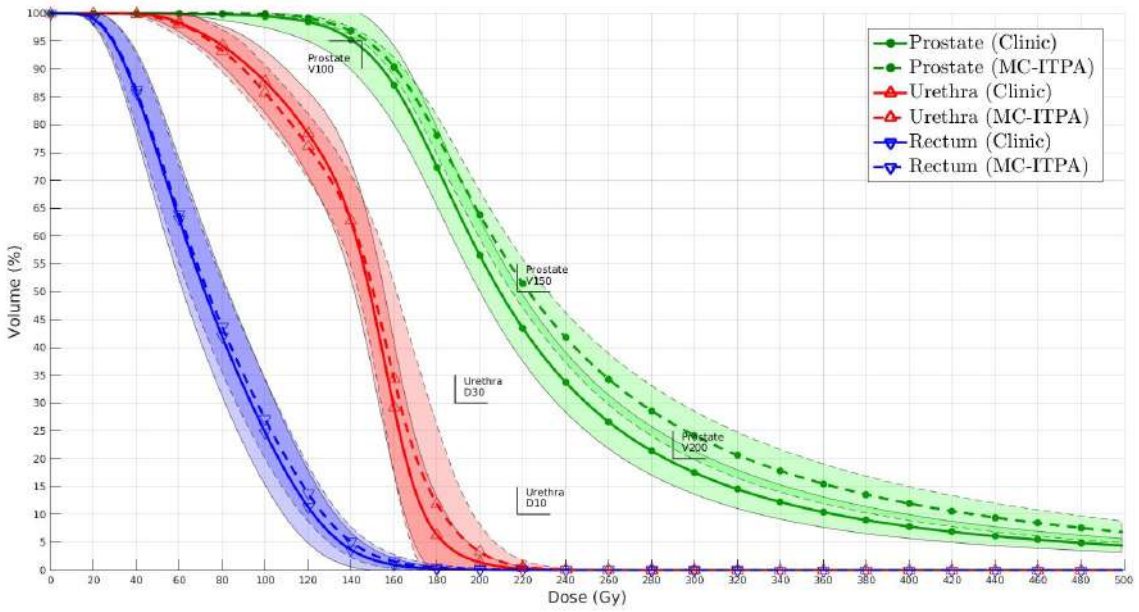

Figure 2.15 – DVH comparison of clinical and MC-ITPA plans. Clinical plans demonstrate more homogeneous prostate dose coverage (V_{150}, V_{200}) than the MC-ITPA plans but the V_{100} is lower than the recommended value (95%), therefore their quality is inferior.

The general lower dose distribution observed in the MC-simulated clinical treatment plans (see Table 2.8, Figure 2.15) is a result of the dose overestimation present in the `AAPM TG-43` formalism. Due to this overestimation, the minimum dose coverage criterion for the prostate ($V_{100} \geqslant 95\%$) is not respected, as presented by the MC simulation. The well-known and extensively reported issue of dose overestimation of the `TG-43` formalism [Beaulieu et al., 2012, Sinnatamby et al., 2015, Xu et al., 2015, and Peppa et al., 2016] is demonstrated in Table 2.9. The clinical plans' dosimetry considering heterogeneous materials, Clinical plan (MC), is compared with the MC simulation of the `TG-43` dosimetry, Clinical plan (`TG-43`), in which all the tissues are simulated as water.

Table 2.9 – Dose metrics overestimation by TG43 dosimetric formalism. The simulated clinical plans with MC on computational heterogeneous phantoms are compared to the clinical plans following the TG43 paradigm. TG43 dosimetric formalism is simulated by MC assigning to all the materials of the computational phantom the composition of water. The percentage relative difference between the TG43-based and the MC-based plans is given.

Organ		Clinical plan (MC)	Clinical plan (TG-43)	Rel. difference (%)
Prostate	$V_{100}(\%)$	94.7 ± (2.3)	96.1 ± (1.5)	1.5
	$V_{150}(\%)$	44.8 ± (4.8)	49.0 ± (4.0)	9.4
	$V_{200}(\%)$	18.9 ± (2.5)	20.7 ± (2.2)	9.5
	$D_{90}(Gy)$	156.7 ± (6.4)	161.6 ± (4.9)	3.1
Urethra	$D_{10}(Gy)$	172.7 ± (8.9)	184.6 ± (8.5)	6.9
	$D_{30}(Gy)$	159.7 ± (5.7)	171.3 ± (4.5)	7.3
Rectum	$D_{2cc}(Gy)$	108.1 ± (10.9)	109.4 ± (10.3)	1.2
	$D_{0.1cc}(Gy)$	153.6 ± (15.7)	156.6 ± (14.8)	2.0

The dosimetric values of clinical plans when the TG-43 formalism is considered demonstrate similar satisfaction to the treatment planning criteria as the MC-ITPA generated plans. However, when MC dosimetry is used dosimetric inaccuracies are reduced and the actual deposited dose does not satisfy the planning criteria in the case of the clinical plans, as it is revealed. Therefore, the selected implants in the clinical plans are sub-optimal compared to the MC-ITPA implants. This is an outcome of the inaccurate dosimetry of the former and the false satisfaction of the treatment planning criteria.

Comments on MC-ITPA plans' quality

Using the proposed MC-ITPA, treatment plans of comparable quality to clinical plans (based on TG43 formalism) can be generated. Moreover, the planning recommendations of the AAPM TG-137 report are respected. High quality plans can be generated fast and efficiently in less than 1 second ($\approx 0.6 - 0.8s$) on the Intel Core i7 4720HQ. However, homogeneous dose delivery in the prostate can be difficult to be achieved in some cases and fine tuning of the optimization parameters is required. This is a drawback of the proposed method and other similar methods that optimize the deposited dose on sampling points on the surface and interior of the organs [Pouliot et al., 1996, D'Amours et al., 2011].

The objective of the clinician is to optimize the dose to be delivered to the patient as it is expressed by the dose volume histogram (DVH). However, since the optimization algorithm optimizes the dose deposited on sampling points (mainly distributed on the surface of the organ), the optimization of the dose deposited in the organs' volume is addressed indirectly. The benefit of this method is that significantly lower amount of data is processed during the optimization (dectors) allowing for fast generation of results. However, a significant drawback is that a complicate cost function must be employed to achieve this indirect optimization (see Equation 2.9). This leads to the introduction of a significant number of optimization parameters (15 in our development) that should be set accordingly in order to achieve plans of good quality. Moreover these parameters do not represent realistic dose requirements and could introduce a significant learning curve in the optimization procedure.

Aiming to provide a "user-friendly" optimization procedure of improved quality, we focus on the direct optimization of the actual dosimetric criteria. To do so we are proposing a DVH-based optimization, based on the presented MC-ITPA.

2.4 DVH-based inverse planning

Optimization of the treatment planning procedure directly on the DVH metrics has been previously performed for inverse planning of IMRT and prostate brachytherapy (LDR/HDR) [Spirou and Chui, 1998, Gorissen, Den Hertog, and Hoffmann, 2013, and Chen, Boyer, and Xing, 2000]. The optimization of DVH-based dose metrics has a natural analogy to the treatment's optimization, therefore, the learning-curve is avoided. More significantly, the simultaneous satisfaction of all the desired dose metrics can be translated in a simple cost function which can be minimized easier. The only drawback of the DVH-based optimization is that a bigger amount of data must be processed during each iteration of the optimization which can lead to longer computational time. To adapt the MC-ITPA to the DVH-based optimization at the minimum computational cost, modifications are introduced in three different steps, named: preprocessing; cost function generation; optimization loop.

Preprocessing update

The DVH-based optimization demands the evaluation of the total dose map of the implant rather than the corresponding dectors in each iteration step. In contrast to the standard version of MC-ITPA, here the total dose map of the implant is constructed in each iteration of the optimization loop by accumulating the corresponding single-seed dose maps. Since the whole single-seed dose map for each seed swapping must be accumulated in each update of the implant's dose map, extra computational work-load is added. However, only the dose recorded in voxels belonging to the organs of interest (prostate, urethra, rectum) is evaluated. In order to reduce the operations during the dose maps accumulation the single-seed dose maps are compressed in a preprocessing step prior to the optimization. In this compression step voxels that do not belong in any of the organs of interest are discarded from the single-seed dose maps and the new compressed dose maps are used during the FSA optimization.

Cost function update

The demand of simultaneous satisfaction of the desired DVH metrics (`AAPM TG-137` recommendations) can be translated in a much simpler cost function than Equation 2.9. This leads to a smoother solution space that can be explored more efficiently by FSA. In the employed DVH-based cost function eight different objectives are simultaneously addressed. These objectives are firstly the requirement of a lower limit for the V_{100} metric, a higher limit for V_{150} metric, and a higher limit for V_{200} metric for the prostate. Secondly, higher limits for the D_{30}, D_{10} and D_{2cc}, $D_{0.1cc}$ metrics for the urethra and the rectum, respectively. Finally, an objective considering the number of the needles to be used for the delivery of the treatment plan. The

DVH-based cost function therefore gets the form

$$\begin{aligned} CF = & w\Theta(V_{100_{LB}} - V_{100}) \cdot (V_{100_{LB}} - V_{100}) + \\ & \sum^{i} w\Theta(V_X - V_{X_{HB}}) \cdot (V_X - V_{X_{HB}}) + \\ & \sum^{j} w\Theta(D_X - D_{X_{HB}}) \cdot (D_X - D_{X_{HB}}) + wN_{needles}, \end{aligned} \tag{2.12}$$

where $V_{100_{LB}}$ defines the lower limit (minimum acceptable value) for the prostate's V_{100} metric, $V_{X_{HB}}$ is the higher limit (maximum acceptable value) for the V_{150} and V_{200} metrics of the prostate. $D_{X_{HB}}$ corresponds to the higher limit for the D_{10}, D_{30} and D_{2cc}, $D_{0.1cc}$ metrics for the urethra and rectum, respectively. Moreover, $w = \frac{1}{N_{objectives}} = \frac{1}{8} = 0.125$ is a common weight factor for each objective and $N_{needles}$ refers to the number of the used needles. The V_{100} and V_X, D_X are the DVH metrics of the plan under evaluation. The lower and higher limits are selected equal to the values given by the `AAPM TG-137` recommendations. The resulting treatment plan can be modified by altering these parameters.

Optimization loop update

The optimization of the DVH-based cost function requires the generation and evaluation of the DVH of the accumulated dose map for each implant during the optimization loop of the FSA algorithm. Since the dose metrics are extracted from the cumulative DVH, the dose map should be processed several times in each iteration for the construction and evaluation of the histograms of the prostate, the urethra, and the rectum. To avoid computational time increase, we construct in each iteration the differential DVHs for the three organs. The three histograms are initialized consisting 500 dose bins with bin width equal to 1 Gy. The dose map is processed only once and according to the recorded dose values the corresponding bins of the differential DVHs are populated. Finally, the differential DVHs are converted in cumulative and the values of the desired dose metrics are extracted. In this way direct DVH-based treatment planning optimization can be achieved in $\approx$ 15s on the `Intel Core i7 4720HQ`.

Dosimetric evaluation of the DVH-based MC-ITPA

The updated DVH-based version of the MC-ITPA (DVH-MC-ITPA) is evaluated against the, previously presented, standard version (MC-ITPA). It is shown that the DVH-MC-ITPA outperforms in dosimetric quality the standard MC-ITPA and provide plans with higher dose homogeneity in the prostate (see Table 2.10).

Table 2.10 – Impoved treatment planning with DVH-MC-ITPA. The DVH-based version of the MC-ITPA can generate treatment plans of improved quality against the standard version. Dose metrics of the treatment plans generated with the two methods are compared and the percentage relative difference between the two is given.

Organ		standard MC-ITPA	DVH-MC-ITPA	Rel. difference (%)
Prostate	$V_{100}(\%)$	95.8 ± (1.1)	96.6 ± (1.0)	0.8
	$V_{150}(\%)$	51.3 ± (3.0)	46.0 ± (2.7)	−10.3
	$V_{200}(\%)$	25.4 ± (4.0)	19.6 ± (0.5)	−22.8
	$D_{90}(Gy)$	161.5 ± (4.6)	162.4 ± (3.8)	0.6
Urethra	$D_{10}(Gy)$	178.8 ± (15.7)	177.3 ± (11.8)	−0.8
	$D_{30}(Gy)$	165.4 ± (11.8)	165.0 ± (9.2)	−0.2
Rectum	$D_{2cc}(Gy)$	114.4 ± (9.0)	108.7 ± (7.8)	−5.0
	$D_{0.1cc}(Gy)$	167.8 ± (16.0)	166.7 ± (21.2)	−0.7
Seeds		64 ± 5	64 ± 5	0.0
Needles		16 ± 2	17 ± 2	6.25

The direct optimization of the DVH metrics enables the fast and efficient generation of treatment plans conforming with great accuracy to the desired planning criteria. There is no need for experimentation with parameters that could create confusion such as in the case of the standard MC-ITPA. Significantly improved dose homogeneity can be achieved in the prostate with the DVH-MC-ITPA. This is demonstrated by the 10.3% and 22.8% decrease in the V_{150} and V_{200} metrics, respectively. Dose deposition in OARs can also be decreased (5.0% decrease in rectum D_{2cc} metric). The improved planning quality of the DVH-MC-ITPA against the standard MC-ITPA can be observed graphically in the DVH representation of the generated treatment plans (see Figure 2.16).

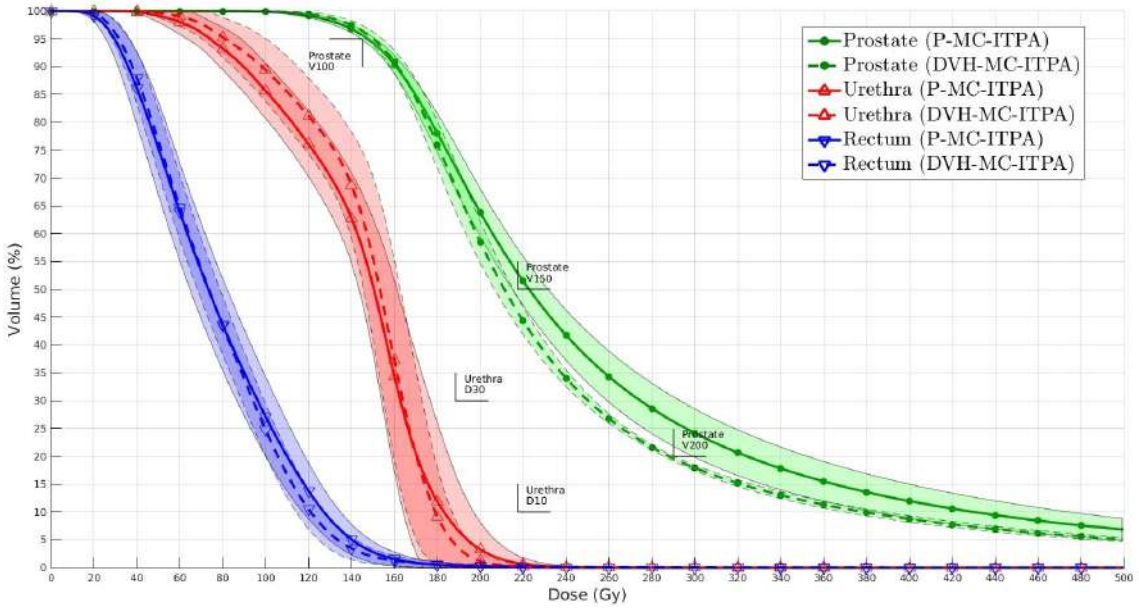

Figure 2.16 – DVH comparison of DVH-MC-ITPA and standard MC-ITPA plans. Planning criteria can be addressed more efficiently by the DVH-MC-ITPA and increased dose homogeneity in the prostate can be achieved while sparring the OARs.

It is demonstrated in Figure 2.16 that the DVH-MC-ITPA can generate treatment plans that respect all the desired planning criteria with improved dose homogeneity at the prostate. Furthermore, the reduced standard deviation, especially for the prostate and the rectum demonstrates the ability of FSA to minimize the employed function effectively. In this way, the desired planning criteria are efficiently met without significant variations for all the patients. Moreover, as shown in Table 2.10, the DVH-MC-ITPA provides improved quality plans compared to the standard MC-ITPA for a similar number of used needles. It was found that for the given patients the `AAPM TG-137` planning criteria were always satisfied. However, the presented results were acquired using a more "restrictive" planning schedule than the one recommended by `AAPM TG-137`. This was done in order to evaluate the performance of the algorithm under extreme conditions. The desired DVH metrics used in this planning schedule are summarized in Table 2.11.

Table 2.11 – Used planning schedule for treatment planning with DVH-MC-ITPA.

Organ	V_{100}	V_{150}	V_{200}	D_{30}	D_{10}	D_{2cc}	$D_{0.1cc}$
prostate	$> 98\%$	$\leq 49\%$	$\leq 20\%$	-	-	-	-
urethra	-	-	-	< 180	< 200	-	-
rectum	-	-	-	-	-	< 145	< 200

The DVH-MC-ITPA is able to satisfy even more "restrictive" planning schedules, however, such plans demand a higher number of needles to be used for their delivery. Therefore, these schedules were not considered. Dose metrics of the treatment plans generated for each individual patient are summarized in Appendix C, Table C.2.

2.5 MC-Inverse treatment planning algorithm summary

In this chapter a fast and efficient GPU-accelerated Monte Carlo inverse treatment planning algorithm (MC-ITPA) was presented. Dosimetry in state of the art inverse treatment planning algorithms (ITPAs) is based on the AAPM TG-43 protocol, which is proven to overestimate the deposited dose (see Subsection 2.3.2). Therefore, based on inaccurate dosimetry, mathematically optimal treatment plans, as generated by current ITPAs, are suboptimal in reality.

On the contrary, the proposed MC-ITPA provides significantly more accurate dosimetric results and hence more optimal solution by using MC-based dosimetry. Even if MC-based dosimetry suffers by long computational time, in our implementation GPU-accelerated MC dosimetry, as provided by the GGEMS platform, is combined with the track length estimator (TLE) to provide fast MC-based dosimetry.

The uncertainty reduction during single-seed dose maps accumulation allows for the generation of dose maps with only few thousands of simulated particles without modifying the statistical uncertainty of the final total seed's configuration dose map. With only $\approx 35ms$ for the generation of a single-seed dose map on a workstation equipped with NVIDIA GTX Titan X, the generation of 400 single-seed dose maps (for all the possible positions a seed could occupy in a standard plan) can be completed in ≈ 15 seconds, time absolutely acceptable in an intraoperative environment.

Following the single-seed dose maps generation, the use of the fast simulated annealing (FSA) algorithm enables, the fast optimization and retrieval of the optimal seeds' configuration in less than $1s$ ($\approx 0.8s$) when the standard proposed MC-ITPA is used. Clinically acceptable plans can be achieved, comparable with clinical plans that were delivered in CHRU Brest. The indirect planning optimization by optimizing the deposited dose on the organ's surface may lead to a learning curve for the operator. Additionally, it is not easy to achieve adequate dose homogeneity in the prostate. The presented DVH-based version of the MC-ITPA overcomes these limitations and delivers plans of improved quality in ≈ 15s on an Intel Core i7 4720 HQ CPU. All the treatment plans generated by the DVH-MC-ITPA during the validation phase of the algorithm (see Subsection 2.3.2) satisfied all the AAPM TG-137 planning recommendations and were significantly better than the provided clinical plans. Moreover, the MC-ITPA was able to achieve these plans using fewer needles than used in the clinical plans which results to treatment plans' delivery with decreased needle-induced mechanical trauma and associated edema occurrence.

Having introduced a fast and efficient inverse planning algorithm using MC-based dosimetry, our focus is now set to decrease further the treatment planning inaccuracies by taking into consideration the formation and evolution of the edema which is associated with the treatment delivery. To do so the edema evolution mechanism must be understood and modeled appropriately.

In the following chapter the LDR brachytherapy-induced edema will be investigated and a biomechanical model aiming to predict its resorption pattern will be developed and presented.

CHAPTER

3

EDEMA BIOMECHANICAL MODELING

Edema mechanism is investigated based on continuum mechanics principles. Following an introduction to the continuum mechanics theory, a patient-specific biomechanical model is developed using the Finite Element (FE) method. Statistical data derived from the literature are used for the validation of our developments. Variations of edema magnitude and edema half-life are associated with the underlying inflammation and the tissue mechanical properties. The effect of prostate stiffness on the edema resorption pattern is studied. Insight in edema dynamics and inter-patient diversion is provided.

Le mécanisme de l'œdème de la prostate est étudié en fonction des principes de la mécanique continue. Suite à une introduction de la théorie de la mécanique continue, un modèle biomécanique spécifique au patient est développé à l'aide de la méthode des éléments finis (FE). Les données statistiques dérivées de la littérature sont utilisées pour la validation de nos développements. Les variations de l'œdème ainsi que de la demi-vie du dégonflement sont associées à l'inflammation sous-jacente et aux propriétés mécaniques des tissus. L'effet de la raideur de la prostate sur la mécanique de résorption de l'œdème est également étudié dans ce chapitre. Des informations sur la dynamique de l'œdème ainsi que sa variation en fonction des patients sont présentées.

"People who are crazy enough to think they can change the world, are the ones who do."

— Rob Siltanen

3.1 Edema effect on dosimetry

Brachytherapy-induced edema is an uncontrolled parameter during and after the treatment procedure. The divergence in edema magnitude and resorption time among patients incommodes the *a priori* estimation of the impact of edema in the treatment delivery.

Consequently, despite how much optimal is a treatment plan, a misplacement of the seeds is expected due to the edema and depends on its magnitude [Villeneuve et al., 2008]. To minimize the seeds misplacement, the treatment planning is executed during the operation after the insertion of the peripheral needles, or/and locking needles, when edema has already occurred. However, no measures are taken to account for the resorption of the edema and the associated movement of the seeds from the initial implantation positions.

Due to changes in the final positions of the seeds, *edema has a negative effect on dosimetry*. As a result, intra-operative dosimetric calculations can have significant deviations from post-implant dosimetric evaluation measurements.Waterman et al. [1997] have demonstrated that a prostate volume decrease of 17% during 38 days after the operation leads to 13% higher D_{90} as measured in post-implant dosimetry at Day 38. This volume decrease is related to edema resorption since volumetric change due to radiation is not expected in only 38 days for ^{125}I implants. Similarly, dose underestimation during Day 1 dosimetry has been shown by Chira et al. [2013] where for a prostate volume change of 10% from Day 1 to Day 30, an 11.7% increase of the D_{90} metric was found in Day 30 dosimetry. Likewise, more studies have demonstrated similar results showing the underestimation of the actual dose to be delivered when the edema resorption mechanism is not accounted [Leclerc et al., 2006 and Villeneuve et al., 2008].

In order to reduce the difference between the estimated dose during the operation and the actual dose to be delivered in the prostate and organs at risk (OARs), several models have been proposed to account for the edema effect on dosimetry (see subsection 1.4.2). However, these models, based on statistical data, do not account for patient-specific edema characteristics. Since edema magnitude can vary from 10% up to 96% and edema half-life (time needed for edema resorption by 50%) from ≈9.3 up to ≈30 days [Waterman et al., 1998, Chira et al., 2013, and Sloboda et al., 2012] such models, depending on averaged data, can not be considered sufficiently accurate.

Understanding the factors and parameters on which edema depends on is essential to establish patient-specific models. According to Tejwani et al. [2012], such factors are the seed activity, the treatment modality (monotherapy vs. combined therapy), and the Gleason score. Contradictorily, Waterman et al. [1998] in their study found no evident correlation between the number of needles, the radioisotope, the number of seeds, and the total seed strength neither with the edema magnitude nor with the half-life. Additionally, no consistent correlation between neither the edema magnitude nor the resorption time is found in other published studies with patient characteristics such as age, pre-implant prostate volume, hormonal uptake, number of needles, number of seeds, and seed activity [Badiozamani et al., 1999b, Taussky et al., 2005b, and Yamada et al., 2003b].

The difficulty in correlating patient characteristics with the edema evolution can be attributed to underlying mechanisms that still remain not investigated. In order to extend our understanding of edema, more extensive investigation of the initial cause of it is required.

Consequently, the attention should be pointed on the initial inflammatory response of the prostate to the treatment procedure which results in the formation of edema. Obtaining insight

into the mechanism of the inflammation could possibly enable the prediction of the resulting edema characteristics.

3.2 Inflammation

Inflammation is the initial body response to biological stress related to intruding pathogens and tissue injury. It involves host cells, blood vessels, proteins, and other mediators aiming in the elimination of the initial cause of cell injury, the cleansing of necrotic cells and tissues, and finally the triggering of the repair process [Kumar, Abbas, and Aster, 2013].

Even though inflammation's role is the defense against harmful agents and the repair of damaged tissues in the affected area, the defending mediators are capable of injuring normal tissues, too. As an outcome to the damage to healthy tissues, further stimulation of inflammation can occur leading to a recursive response which could even result in organ failure and death [Kumar et al., 2004]. This counter-effect of inflammation can arise in situations of severe infection, of eradication-resisting pathogens, or in autoimmune diseases. Under normal conditions, inflammation is a physiological process consisting the first-line defense of the organism. The mechanism of this process is a complex cascade of sequential events.

3.2.1 Underlying inflammation mechanism

In homeostasis, cells and molecules of the immune system, such as leukocytes and plasma proteins are circulating in the blood. When a tissue damage occurs, by cause of an infection or injury, the triggered inflammatory response intends to bring the immune system mediators to the damaged site.

In more detail, in the presence of an injury, resident cells of the impaired area, such as macrophages, dendritic cells, and mast cells secrete chemical mediators (i.e. cytokines and others) that control the consequent inflammatory response [Ahmed, 2011]. Furthermore, plasma proteins are producing inflammatory mediators, too. These mediators react with microbes or damaged tissues and support the efflux of plasma carrying leukocytes from the circulation to the injured region (see Figure 3.1). The delivered leukocytes are activated and endeavor to remove the offending agents by phagocytosis.

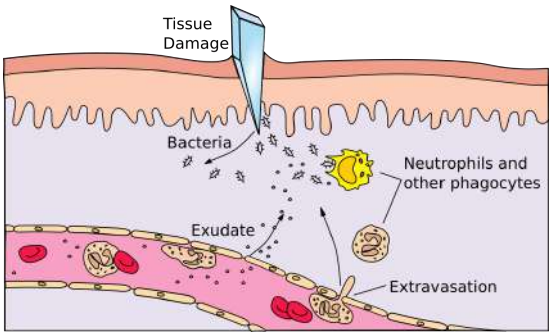

Figure 3.1 – Inflammation mechanism. In the presence of a pathogen intrusion or tissue injury the inflammation mechanism is triggered. Mediators originated from the damaged area and the proximal vasculature initiate a cascade of events aiming to eliminate the pathogenic agent and repair the injury.

The external signs of inflammation are heat, redness, swelling, pain, and loss of function. Considering its duration, inflammation can be characterized as acute or chronic. The rapid response to an alteration of homeostasis by an offending agent describes the acute inflammation response. This rapid response is often controlled and can last from few seconds up to few days. If the infection or injury cannot be quickly eliminated the result may be chronic inflammation, which lasts from several days up to years and can cause serious detrimental side-effects (heart disease, cancer, diabetes, etc).

Acute inflammation

In *Acute inflammation* (AcI), leukocytes and plasma proteins are delivered rapidly to the damaged site. The role of leukocytes is to iradicate the invading pathogens and begin the digestion process of necrotic tissues. Vascular changes, such as vasodilation and increased permeability, support the emigration of leukocytes and plasma proteins. These vascular changes can be triggered by various stimuli, such as infections, trauma, tissue necrosis, and foreign bodies [Kumar, Abbas, and Aster, 2013]. They are prompted by chemical signals emitted from receptors (phagocytes, dendritic cells, and other epithelial cells) that can sense microbes, infectious pathogens, and substances released from dead cells.

Due to the arteriolar vasodilation, the blood flow is increased locally and the down-stream capillary beds are enlarging. This vascular expansion is the cause of the redness and warmth characteristic of acute inflammation. The increase of vascular permeability facilitates the movement of protein-rich fluid into the extravascular tissues. This movement results in an increased concentration of red cells and hence, increased blood viscocity and slower blood circulation (stasis). As stasis develops, leukocytes (principally neutrophils) start to accumulate along the vascular endothelial surface and eventually emigrate in the extravascular tissues.

The excessive accumulation of protein-rich fluid and blood cells in the extravascular tissues increases the osmotic pressure of the interstitial fluid, resulting in increased outflow of water from the blood into the tissues. The resulting protein-rich fluid accumulation is called exudate and is responsible for the formation of edema (see Figure 3.2).

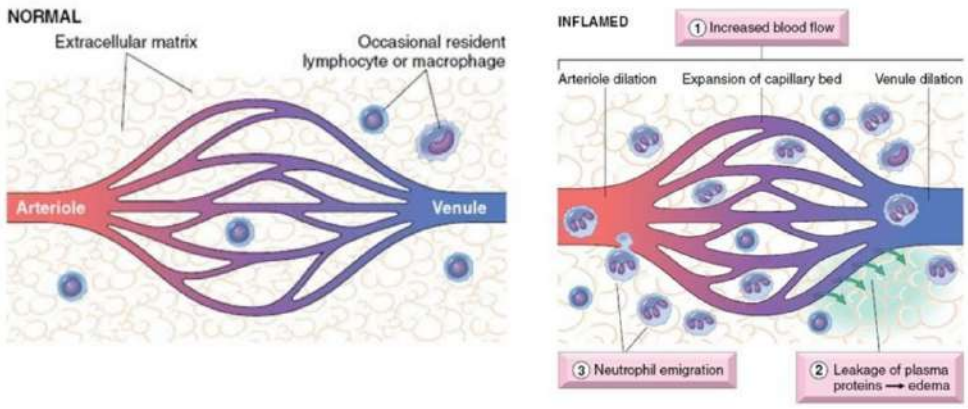

Figure 3.2 – Exudate formation. The vascular permeability increase promotes the movement of repairing cells and proteins to the impaired area. These agents are carried by a protein-rich fluid called exudate which accumulates in the extravascular tissues and leads to edema formation. Image from [Kumar, Abbas, and Aster, 2013]

The most common cause of increased vascular permeability is endothelial cell contraction, which creates intercellular gaps in postcapillary venules [Vandenbroucke et al., 2008]. This increase occurs immediately after the binding of mediators with specific receptors and usually has a short duration (15 to 30 minutes). Moreover, changes in the cytoskeleton and cytokines such as tumor necrosis factor (TNF) and interleukin-1 (IL-1) may induce a slower and more prolonged retraction of endothelial cells. This reaction may take 4 to 6 hours to develop after the initial trigger and can persist for 24 hours or more.

Endothelial injuries cause endothelial cell necrosis and detachment resulting in vascular leakage. Endothelial cells are impaired after a severe injury, such as burns and aggressive infections. In most cases, leakage starts shortly after the injury and endures for several hours (or even days) until the damaged vessels are repaired.

The outcome of acute inflammation may be the removal of the exudate and restoration of the normal tissue architecture (resolution); transition to chronic inflammation; or extensive tissue destruction resulting in scarring.

Chronic inflammation

Chronic inflammation (ChI) is a state in which inflammation, tissue injury, and healing proceed simultaneously for a prolonged time. Chronic inflammation is characterized by infiltration of mononuclear cells (macrophages, lymphocytes, and plasma cells), tissue destruction, and repair involving new vessel proliferation (angiogenesis) and fibrosis [Shacter and Weitzman, 2002]. ChI can pursue acute inflammation in case the latter cannot be resolved. Persistent microbial infections that are difficult to eradicate, immune-mediated inflammatory diseases, or prolonged exposure to potentially toxic agents can be the cause of chronic inflammation. The combination of prolonged and repeated inflammation, tissue destruction and fibrosis that characterizes chronic inflammation involves complex interactions between several cell populations and their secreted mediators.

The macrophages, the first involved population, are the dominant cells of chronic inflammation. They are tissue cells originated from monocytes circulating in the vasculature after their emigration from the bloodstream. The role of macrophages, like neutrophils, is the ingestion and elimination of microbes and dead tissues. Additionally, macrophages trigger the process of tissue repair and are implicated in fibrosis. Furthermore, they secrete mediators of inflammation, such as cytokines (TNF, IL-1, chemokines, and others) and eicosanoids [Nathan, 1987]. These cells are, therefore, central to the initiation and propagation of all inflammatory reactions. Macrophages display antigens to T lymphocytes and respond to signals from T cells, thus setting up a feedback loop that is essential for defense against many microbes by cell-mediated immune responses (see Figure 3.3). After the initiating stimulus is eliminated and the inflammatory reaction recedes, macrophages eventually die or drift into the lymphatics. In chronic inflammatory sites, however, macrophage accumulation persists, through continued recruitment from the blood and local proliferation.

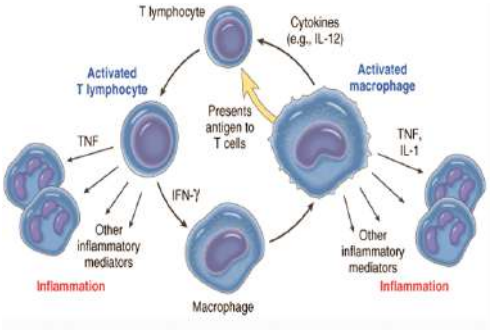

Figure 3.3 – Chronic inflammation recursion. Macrophages which have a key role in inflammatory reactions display antigens to T lymphocytes and additionally respond to signals emitted from the latter. This emission-response circle leads to a chronic inflammation recursive loop that can lead to serious complications.

Another involved population, are the lymphocytes which are triggered by any specific immune stimulus (i.e., infections) as well as non-immune-mediated inflammation, such as trauma. They are responsible for the inflammatory response to many autoimmune and chronic inflammatory diseases.

Lymphocytes and macrophages interact in a bidirectional way (see Figure 3.3), and their interactions play an important role in propagating chronic inflammation. Macrophages display antigens to T cells, express membrane molecules, and produce cytokines that stimulate T cell responses. Moreover, T lymphocytes, in response, produce cytokines which engage and activate macrophages. The result is a recursive loop of cellular reactions that fuel and sustain chronic inflammation.

In some strong and prolonged inflammatory reactions, the accumulation of lymphocytes (antigen-presenting cells) and plasma cells may assume the morphologic features of lymphoid organs and alike to lymph nodes may even contain well-formed germinal centers. This pattern of lymphoid organogenesis is often seen in the synovium of patients with long-standing rheumatoid arthritis and the thyroid of patients with autoimmune thyroiditis [Dayan and Daniels, 1996].

3.2.2 Starling equation

Edema formation can be associated with different pathologic conditions. Excessive fluid can accumulate within cells (cellular edema) or within the extracellular matrix in the interstitial space (interstitial edema). Some of the possible types of interstitial edema are:

- Vasogenic — due to capillary hypertension or hypoproteinemia
- Permeability edema — due to trauma, or endogenous mediators
- Myxedema — due to overproduction of interstitial collagen and mucopolysaccharides
- Lymphedema — due to lymphatic vessels dysfunction

In brachytherapy operation, the occurring edema is a result of the inflammation response associated with trauma, due to needle penetration and radiation-related cellular death, as described in subsection 3.2.1. The flow of exudate in the interstitial matrix, facilitated by the

increased vascular permeability, increases the interstitial colloid osmotic pressure which consequently increases the net filtration pressure (see Figure 3.4). Furthermore, due to vasodilation, the capillary pressure elevates, further increasing the net filtration pressure. The microvascular surface area available for fluid and protein flux into the tissues also increases as a consequence of vasodilation [Scallan, Huxley, and Korthuis, 2010]. The microvascular surface increase supports the increased net filtration pressure, promoting volume flux. Moreover, the releasing products of phagocytic cells (hydrolytic enzymes, reactive oxygen, and nitrogen) disrupt the extracellular matrix components and allow a larger volume of extracellular fluid to be accumulated within the matrix with little increase in interstitial fluid pressure.

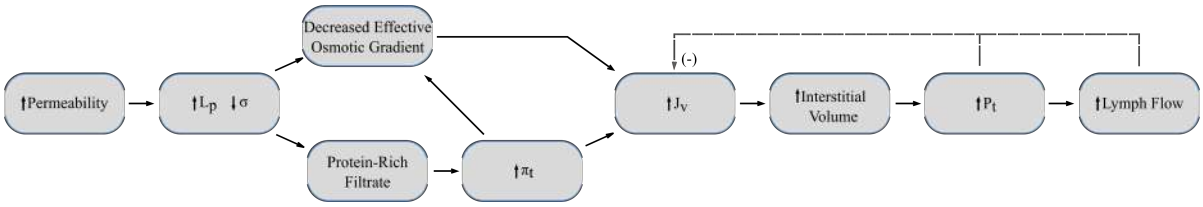

Figure 3.4 – Volumetric fluid flux increase. The increase of vascular permeability due to the inflammatory response results in increase of the interstitial colloid pressure and subsequently increase in the net filtration pressure promoting the volumetric fluid flux increase and fluid accumulation in the extravascular tissue.

It is obvious that the fluid flow between the vascular system and the interstitial matrix is associated with pressure differences between the two compartments that drive the flow of the fluid. Ernest Starling in 1896, introduced a model for the description of fluid movement between vascular and tissue compartments based on the hydrostatic and oncotic pressure gradients and the surface area [Starling, 1896]. The surface area is a parameter determined by the dimensions, length and diameter, and the number of vessels in a network. The hydrostatic pressure gradient (ΔP) represents the relative pressure difference between a capillary and the interstitial space,

$$\Delta P = P_c - P_t, \tag{3.1}$$

where P_c defines the capillary pressure and P_t the interstitial pressure. In similar manner, the oncotic pressure gradient ($\Delta\pi$) is given as

$$\Delta\pi = \pi_c - \pi_t. \tag{3.2}$$

The capillary hydrostatic (P_c) and the interstitial osmotic (π_t) pressures support the movement of fluid from the vascular to extravascular compartment, while the capillary osmotic pressure favors the movement of fluid into the vascular space [Scallan, Huxley, and Korthuis, 2010]. P_c is a function of blood pressure, while the oncotic pressure (π) is a function of protein concentration in the corresponding compartment.

For given surface area (S), hydrostatic (ΔP), and oncotic ($\Delta\pi$) gradients, the volumetric fluid flux (J_v) is described by the modern version of the *Starling equation*:

$$J_v = L_p S(\Delta P - \sigma\Delta\pi) = L_p S(NFP), \tag{3.3}$$

where L_p defines the hydraulic conductivity, NFP is the net filtration pressure, and σ refers to the osmotic reflection coefficient. In homeostasis, NFP is positive and results in a slight net

fluid movement (capillary filtration) into the tissues. This net fluid movement is balanced by the lymphatic drainage (see Figure 3.5).

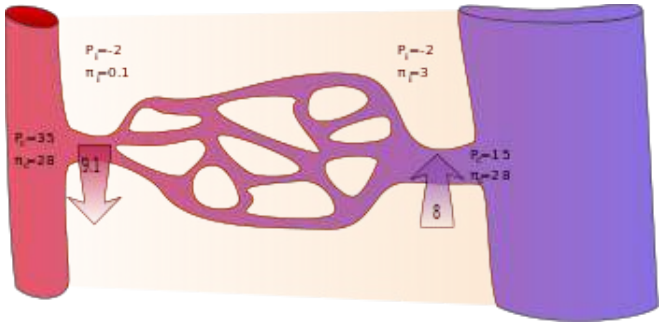

Figure 3.5 – Capillary filtration equilibrium. The slight net fluid movement from the capillaries to the extravascular tissue is balanced by lymphatic drainage during homeostasis and no fluid accumulation is observed. Image from Wikipedia.

During an inflammatory response, *NFP* is further increasing and the fluid accumulation in the interstitial matrix is greater than the lymphatic drainage leading to swelling of the tissue. Therefore, Starling equation (see Equation 3.3) is a useful tool to describe fluid accumulation in tissular media in terms of pressure gradients. The extent of swelling, due to the volume fluid flux, depends upon tissue mechanical parameters, such as elastic properties, and should be accounted for a complete description of the phenomenon.

3.3 Continuum mechanics

Continuum mechanics is a branch of physics dealing with the analysis of kinematics and mechanics of materials modeled as continuum bodies. Partial differential equations (PDEs) are used to describe conservation laws of mass, momentum, and energy that describe the state of a given body. The response of the body under specific boundary conditions (BCs), such as displacement and traction conditions, can be calculated solving the initial-boundary value problem of the given PDEs for the specified BCs.

In medicine, continuum mechanics is used to model the response of various organs to external loads (surgery manipulation, etc.) or internal loads (forces arising inside the organ). It should be noted that the system of equations arising in an initial-boundary value problem is underdetermined (less equations are available than the unknown fields). In order to overcome this inconsistency, constitutive equations which describe the material-specific relation between kinetic and kinematic unknown fields are introduced. The realism of a continuum mechanics model depends strongly on the applied constitutive equations used to describe the mechanical response of the continuum body.

Generally, it is quite challenging to formulate constitutive equations able to describe accurately biological tissues demonstrating high anatomical complexity. However, some approximations can be done in regard to the given tissue and phenomenon under investigation and accurate results can be obtained. Moreover, models of various complexity can be applied according to the desired level of detail. In principle biological tissue is a biphasic material (vascularized tissue), where a fluid phase is coupled with a solid porous compartment, and

the interaction between the two phases should be described mathematically. In case that this interaction is not of significant interest, the model's complexity can be relaxed by modeling the given tissue as a pure elastic material (linear or non-linear). Furthermore, when tissues of high stiffness are under examination the complexity can be further decreased by approaching the tissue of interest as rigid, which is the case mainly when dealing with osseous tissue.

All the three approaches (biphasic, elastic, rigid) are employed in the following development of the prostate edema biomechanical model. Therefore, the mathematical formalism of these approaches is briefly described in subsections 3.3.1-3.3.3 for consistency. For a more extensive understanding of continuum mechanics and the mentioned approaches, the reader is addressed to [Gonzalez and Stuart, 2008 and Ateshian, 2017]

3.3.1 Rigid body deformations

Due to the continuum assumption, a given material body can be identified at any fixed instant of time by an open subset B of Euclidean space $\mathbb{E}^3$. B is called a *configuration* of the body in $\mathbb{E}^3$. Now, a change of the initial body configuration B (reference) to a new configuration B' (deformed) is called deformation. The deformation from configuration B to configuration B' is described by a deformation map. The deformation map is a function $\phi : B \rightarrow B'$, mapping each point $\boldsymbol{X} \in B$ to a point $x = \phi(\boldsymbol{X}) \in B'$ (see Figure 3.6)

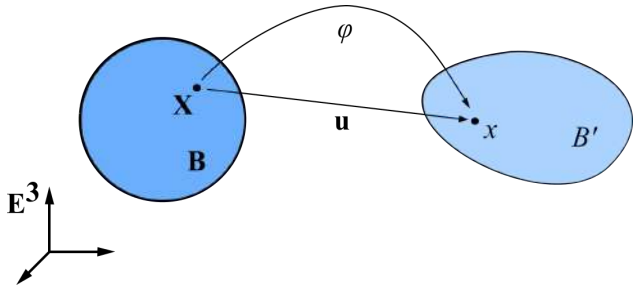

Figure 3.6 – Deformation map. Every configuration, B', of a given body can be described as deformation map $\phi : B \rightarrow B'$, mapping each point $\boldsymbol{X}$ of the reference (undeformed) configuration, B, to a point $x = \phi(\boldsymbol{X})$ in the new configuration B'.

The displacement $\boldsymbol{u}$ of each material particle from its initial location $\boldsymbol{X}$ to its final location $\boldsymbol{x}$ is given by

$$\boldsymbol{u}(\boldsymbol{X}) = \phi(\boldsymbol{X}) - \boldsymbol{X}. \tag{3.4}$$

Under a given deformation, a configuration can undergo shape changes (see Figure 3.6). Local shape changes around a given point X_0 (stretching) are referred as the *strain* at X_0. When a deformation is *rigid*, no strain is produced [Gonzalez and Stuart, 2008]. Such a deformation can be described as

$$\phi(\boldsymbol{X}) = \boldsymbol{c} + \boldsymbol{Q}\boldsymbol{X}, \tag{3.5}$$

where $\boldsymbol{c}$ defines a translation vector and $\boldsymbol{Q}$ describes a rotation tensor. Since the distance between material points remains constant, a rigid motion can be decomposed in a translation of a material point and a rotation around this point described by the vector $\boldsymbol{c}$ and the tensor

$\boldsymbol{Q}$ respectively (see Figure 3.7). This point can be any material point belonging to the body but usually, for simplification, the motion is described using as reference the body's center of mass.

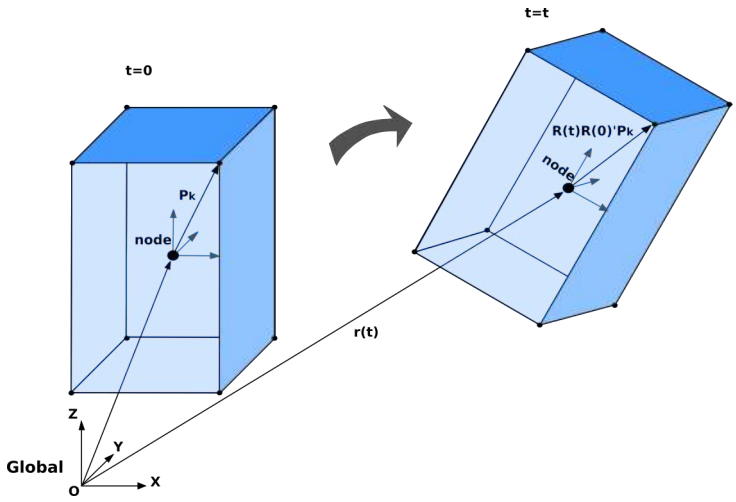

Figure 3.7 – Rigid motion. A motion is considered rigid when no stains are developing under any possible deformation. Such a deformation can be described in terms of pure rotations and translations.

3.3.2 Elastic body deformations

Elastic, is called a body which undergoes a deformation while is subjected to external forces and returns back to its initial shape and size when the forces stop to act. In contrast to rigid body deformation, strain is produced in elastic deformation. The strain can be quantified by introducing the deformation gradient, which is a second-order tensor $\boldsymbol{F} : B \rightarrow V^2$ defined by

$$\boldsymbol{F}(\boldsymbol{X}) = \nabla\phi(\boldsymbol{X}) = \begin{bmatrix} \phi(\boldsymbol{X})_{1,1} & \phi(\boldsymbol{X})_{1,2} & \phi(\boldsymbol{X})_{1,3} \\ \phi(\boldsymbol{X})_{2,1} & \phi(\boldsymbol{X})_{2,2} & \phi(\boldsymbol{X})_{2,3} \\ \phi(\boldsymbol{X})_{3,1} & \phi(\boldsymbol{X})_{3,2} & \phi(\boldsymbol{X})_{3,3} \end{bmatrix}, \tag{3.6}$$

where the notation $\phi(\boldsymbol{X})_{i,j}$ stands for $\partial\phi(X)_i \big/ \partial X_j$. The deformation gradient F provides information on the local behavior of a deformation ϕ. Applying polar decomposition, the deformation gradient can be written $F = RU = VR$, where RU and VR are the right and left polar decomposition respectively. F contains information on both rotations and stretches, however a more useful strain quantifier can be derived which contain information only for stretches. This is the so-called right Cauchy-Green strain tensor, $\boldsymbol{C} : B \rightarrow V^2$, given by

$$C = F^T F = (RU)^T RU = U^2, \tag{3.7}$$

where the rotational information R is extinguished. Additionally, C is symmetric and positive-definite. As a consequence of the existence of strain, an internal elastic stress is generated.

Stress expresses the internal forces arising inside a body between its particles which tend to resist to any deformation of the body when it is subjected to external forces. In any internal

point P of a body in static equilibrium we can define a small surface ΔA on an imaginary plane cutting the body at the point P with outward surface normal $\boldsymbol{n}$ (see Figure 3.8).

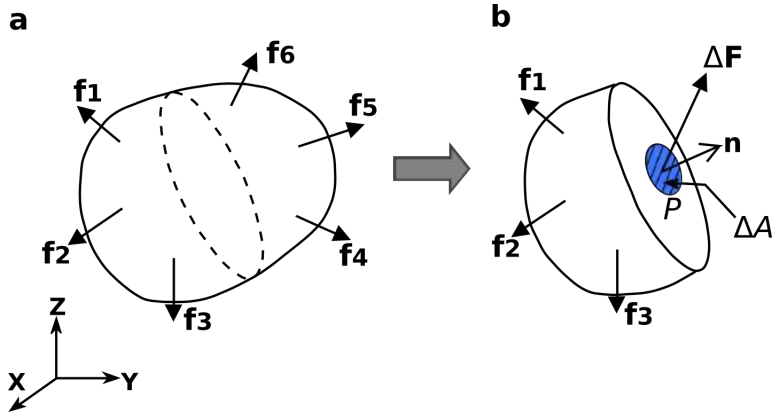

Figure 3.8 – Internal body forces. At any point P inside a body, subjected to external forces, opposite internal forces arising to maintain equilibrium.

The surface traction $\boldsymbol{t}^{(\boldsymbol{n})}$ acting at the point P can be defined as

$$\boldsymbol{t}^{(\boldsymbol{n})} = \lim_{\Delta A \to 0} \frac{\Delta F}{\Delta A}, \tag{3.8}$$

where the superscript $\boldsymbol{n}$ denotes that $\boldsymbol{t}^{(\boldsymbol{n})}$ is the traction applied on the surface with outward normal $\boldsymbol{n}$. If $\boldsymbol{x}$ is the position vector of a point P, then for the traction function $\boldsymbol{t}(\boldsymbol{n}, \boldsymbol{x})$ a second-order tensor exists, such that

$$\boldsymbol{t}(\boldsymbol{n}, \boldsymbol{x}) = \boldsymbol{\sigma}(\boldsymbol{x}) \cdot \boldsymbol{n} = \boldsymbol{\sigma}_{ij} \boldsymbol{n}_i. \tag{3.9}$$

The tensor $\boldsymbol{\sigma} : B \to V^2$ is called the *Cauchy stress tensor* for the body B. Considering an infinitesimal cubic fragment of the body, the components of the Cauchy stress tensor describe the state of stress on the perpendicular directions (*normal stress*) and the parallel directions (*shear stress*) on the surfaces of the infinitesimal cube (see Figure 3.9).

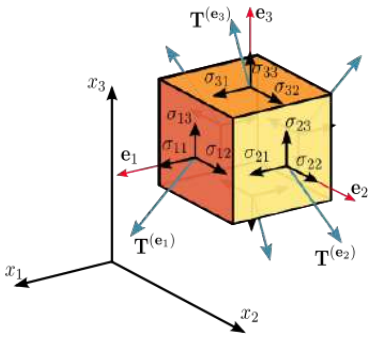

Figure 3.9 – Cauchy stress tensor. For any given point P of a body, the stress acting on the point can be analyzed in perpendicular (normal) and parallel (shear) contributions on the surfaces of an infinitesimal cube enclosing P which are the components of the Cauchy stress tensor.

The equation describing the elastic motion (*elastodynamics equation*) can be derived from the law of linear momentum conservation, hence the deformation of an elastic body B can be described from the elastodynamics initial-boundary value problem

$$\begin{aligned}
\rho_0 \ddot{\boldsymbol{u}} &= \nabla \cdot \boldsymbol{\sigma} + \rho_0 \boldsymbol{b} && \text{in } B && (3.10a)\\
\boldsymbol{u} &= \boldsymbol{f} && \text{on } B^{\partial D} && (3.10b)\\
\boldsymbol{\sigma} \cdot \boldsymbol{n} &= \boldsymbol{t} && \text{on } B^{\partial N} && (3.10c)\\
\boldsymbol{u}(\cdot, 0) &= \boldsymbol{U_0} && \text{in } B && (3.10d)\\
\dot{\boldsymbol{u}}(\cdot, 0) &= \boldsymbol{V_0} && \text{in } B && (3.10e)
\end{aligned}$$

where $B^{\partial D}$ defines the part of the boundary surface of the body B where displacement is fixed to $\boldsymbol{f}$ (*Dirichlet condition*), $B^{\partial N}$ corresponds to the boundary surface where traction $\boldsymbol{t}$ is known (*Neumann condition*), $B^{\partial D} \cup B^{\partial N} = B^{\partial}$ (the total boundary surface), and $B^{\partial D} \cap B^{\partial N} = \varnothing$. In addition $\boldsymbol{U_0}$ and $\boldsymbol{V_0}$ express the initial values (for $t = 0$) of the displacement $\boldsymbol{u}(\boldsymbol{x}, t)$ and the velocity $\dot{\boldsymbol{u}}(\boldsymbol{x}, t)$ field respectively.

The elastodynamics initial-boundary value problem (see Equation 3.10) is completed by introducing a constitutive equation which describes the stress-strain relationship of the elastic material. For an isotropic linear elastic material, the constitutive relation is given by

$$\sigma_{ij} = \lambda \varepsilon_{kk} \delta_{ij} + 2\mu \varepsilon_{ij}, \tag{3.11}$$

where σ_{ij} is the Cauchy stress tensor components, $\varepsilon_{ij} = 0.5(u_{i,j} + u_{j,i})$ is the infinitesimal strain tensor components, and the parameters λ, μ are elastic parameters known as Lamé parameters [Lamé, 1866].

The above constitutive relation can describe the motion of an elastic material undergoing small deformations. In the study of biological tissues where large deformations are common, more complex (non-linear) constitutive equations should be used instead.

3.3.3 Biphasic mixture theory

Soft human tissues demonstrate elastic properties and elastodynamics can be used to describe various phenomena and interactions of the human body. However, in some cases, the elastic properties of the soft tissues may not be sufficient to describe complicate phenomena. The majority of biological tissues are porous and permeable hence, in some cases the contribution of interstitial fluid pressurization and flow in the mechanical properties of the tissue can not be neglected.

In these cases, *biphasic mixture theory* can be used to describe soft tissues as a porous permeable deformable medium. Biphasic mixture theory is a special case of mixture theory, where the mixture consists of two compartments, a solid and a fluid compartment coupled to each other. Mixture theory was first introduced by Truesdell and Toupin [1960] and since then have been used in studies of soft tissues, such as articular cartilage [Mow, 1984, Mow and Roth, 1981, and Mow et al., 1989].

In biphasic mixture theory, both the solid and fluid compartment are assumed to be intrinsically incompressible, such as there is no reaction between the solid and fluid. While the incompressible fluid assumption is reasonable since water is nearly incompressible under

physiological stress magnitudes, the incompressible assumption for the solid must be verified experimentally.

In this theory, each constituent α of the mixture (α = s for solid and α = w for fluid) has a separate motion $\phi^\alpha(\boldsymbol{X}^\alpha, t)$ that deforms particles of each mixture compartment from the reference position $\boldsymbol{X}^\alpha$ to the deformed configuration $\boldsymbol{x}$

$$\boldsymbol{x} = \phi^\alpha(\boldsymbol{X}^\alpha, t). \tag{3.12}$$

In the governing equations, as described in Maas et al. [2011], the mixture is treated as a whole and under quasi-static conditions the conservation of linear momentum is expressed as

$$\nabla \cdot \boldsymbol{\sigma} + \rho \boldsymbol{b} = \boldsymbol{0}, \tag{3.13}$$

where $\boldsymbol{\sigma}$ defines the Cauchy stress mixture, ρ is the mixture density, and $\boldsymbol{b}$ is the external force per mass. The mixture is porous and the stress tensor can be described as

$$\boldsymbol{\sigma} = -p\boldsymbol{I} + \boldsymbol{\sigma}^e, \tag{3.14}$$

where p is the fluid pressure, $\boldsymbol{\sigma}^e$ is the effective stress resulting from the solid compartment's deformation and $\boldsymbol{I}$ is the *identity tensor*. In addition, the conservation of mass for the mixture requires that

$$\nabla \cdot (\boldsymbol{v}^s + \boldsymbol{w}) = 0, \tag{3.15}$$

where $\boldsymbol{v}^s = \dot{\boldsymbol{u}}$ is the solid matrix velocity –$\boldsymbol{u}$ is the solid component's displacement field– and $\boldsymbol{w}$ the fluid flux relative to the solid compartment. The relative fluid flux $\boldsymbol{w}$ is related to the fluid pressure and the solid deformation. The equation of linear momentum conservation for the fluid compartment is derived as

$$-\phi^w \nabla p + \rho^w \boldsymbol{b}^w + \hat{\boldsymbol{p}}_d^w = \boldsymbol{0}, \tag{3.16}$$

where ϕ^w defines the solid matrix porosity, $\rho^w = \phi^w \rho_T^w$ describes the apparent fluid density and ρ_T^w is the true fluid velocity, b^w expresses the external body force per mass acting on the fluid, and $\hat{\boldsymbol{p}}_d^w$ is the momentum exchange between the solid and fluid compartments which represents the frictional interaction between these constituents. The most commonly used constitutive relation is $\hat{\boldsymbol{p}}_d^w = -\phi^w \boldsymbol{k}^{-1} \cdot \boldsymbol{w}$, where the second order, symmetric tensor k refers to the hydraulic permeability of the mixture. In combination with Equation 3.16, it produces

$$\boldsymbol{w} = -\boldsymbol{k} \cdot (\nabla p - \rho_T^w \boldsymbol{b}^w), \tag{3.17}$$

which is equivalent to Darcy's law. In general, $\boldsymbol{k}$ can be a function of the deformation.

3.4 Modeling techniques

Soft tissues can be modeled completely by solving the initial-boundary value problem considering various boundary conditions for the description of interactions with their environment. The smoothness of the solution depends on the order of the employed differential equation. In elastic and biphasic models the governing differential equation requires solutions with C^2

continuity. In other words, second-order derivatives of the solution, arising from the combination of stress divergence (see Equation 3.10a) with the stress-strain relationship (see Equation 3.11), must be continuous.

However, it is possible to relax the solution's continuity requirement by using the variational approach, which can be related to the *virtual work principle* [Bathe, 2006]. When a force is applied to a particle, work is generated. The generated work will be different for different displacements of the point. All these possible displacements are called *virtual displacements* and among them one will require the least action and will be the one that the point will follow according to the principle of least action. Virtual work is the work of a force acting on a particle along a virtual displacement and is expressed as

$$\delta W = \iint_{\Omega} \bar{\boldsymbol{u}} \cdot \boldsymbol{f}^b d\Omega + \int_{\Gamma} \bar{\boldsymbol{u}} \cdot \boldsymbol{t} d\Gamma, \tag{3.18}$$

where $\bar{\boldsymbol{u}}$ is a virtual displacement, $\boldsymbol{f}^b$ body forces acting on the body domain Ω, and $\boldsymbol{t}$ tractions acting on the body boundary Γ.

Finding the analytical solution of the variational equation deriving from the principle of virtual work is arduous especially in complex geometry problems like the one arising in tissue modeling and hence, numerical approximation techniques are used to find a proximal approximate solution.

3.4.1 Finite elements method

Among numerical approximation techniques, the finite elements (FE) method is one of the most well known techniques for solving complex engineering problems. The main characteristic of this technique is that the domain of interest is discretized into a set of simple interconnected sub-domains (finite elements). The solution of the variational equation (see Equation 3.18) can then be approximated in a simple polynomial form within each finite element.

The solution $u(x)$ to the variational equation can be described by a sum of a number of trial functions such as

$$u(x) = \sum_{i=1}^{n} c_i \phi_i(x), \tag{3.19}$$

where n is the number of terms used, $\phi_i(x)$ are known trial functions, and c_i are coefficients to be determined by minimizing the error between the exact and the approximate solution. The accuracy of the approximation depends on the employed trial functions. The trial functions and coefficients must be chosen such as they satisfy the essential boundary conditions of the problem.

Under such a requirement, it is difficult to obtain the trial functions if the solution is approximated on the whole domain. Dividing the domain into simple elements and approximating the solution individually in these elements allows to construct trial functions for internal elements without considering the essential boundary conditions and only treating differently those elements that include the essential boundary conditions. Then, the solution within each finite element can be approximated with a simple polynomial form.

The simplest trial functions that can be employed are piecewise continuous linear polynomials

$$u(x) = \alpha_0 + \alpha_1 x, \;\; x_i \leq x \leq x_{i+1} \tag{3.20}$$

where x_i, x_{i+1} denotes the two nodes of a one-dimensional element and α_0, α_1 are unknown coefficients. With this type of trial functions, the exact solution is linearly approximated within the elements (see Figure 3.10).

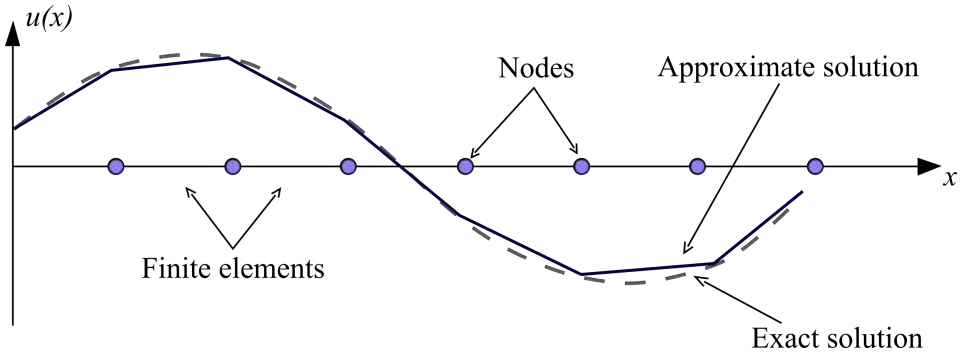

Figure 3.10 – Finite elements approximation. The domain of a function can be discretized in a finite number of elements in which the solution can be approximated numerically with trial functions, such as the piecewise continuous linear polynomials.

The unknowns α_0 and α_1 can be expressed in terms of the nodal solutions $u(x_i)$ and $u(x_{i+1})$. In order for the approximate solution to converge to the exact one, a more dense discretization of the domain, or the use of high-order polynomial trial functions is necessary. In terms of practical implementation a dense discretization requires more computer resources and therefore usage of high-order polynomial trial functions is more appealing. However, producing high-order polynomial trial functions for 2-/3-dimensional domains is a complicated task. Algorithms able to produce automatically 3D discretizations of high-order elements are not currently available and manual or semi-automatic methods, requiring significant time and effort, must be used.

In medical applications, where intra-operative time limitations have to be met, a trade-off between discretization speed and accuracy must be made.

3.4.2 Mesh generation

The subdivision process of a domain into simple elements is essential for the approximation of differential equations using the method of FE. Techniques for discretization of arbitrary geometries, known as *mesh generation*, are hence, of great interest. A *mesh* is a collection of connected discrete geometric objects that approximate the geometry of a given domain. Expanding the intuitive discretization of 1-dimensional geometries in linear components, higher dimensional geometries can be discretized in triangles or quadrangles, in 2D, and in tetrahedra or hexahedra in 3D, respectively (see Figure 3.11).

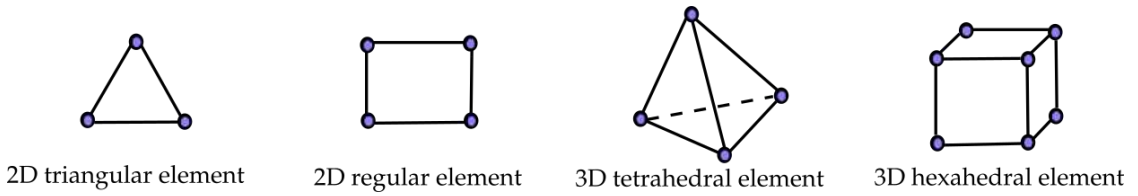

Figure 3.11 – Mesh elements. Any given domain can be descretized in a number of simple mesh elements. In 2D or 3D domains common elements are triangles or quadrilaterals and tetrahedra or hexahedra, respectively.

In the case of a 3D hexahedral mesh, the domain is discretized in small brick elements. Each brick element consists of 8 *vertices*. Two sequential vertices form a line segment, leading to 12 *edges* and four sequential vertices construct a surface, forming 6 *faces*. A mesh can be structured, unstructured, or hybrid (see Figure 3.12). In a structured mesh topology, all vertices follow a regular pattern, while in an unstructured mesh vertices are irregularly distributed in the discretized domain. Structured meshes offer regularly shaped elements and present easy data access, however it is difficult to describe complex curved geometries. On the contrary, unstructured meshes can approximate more accurately complex geometries and offer more convenient adaptivity. Furthermore, a geometric domain can be discretized using fewer vertices when an unstructured mesh is used rather than a structured. On the other hand, irregular elements are presented in unstructured meshes and care should be taken to avoid extremely distorted elements. Such elements can cause numerical instabilities and even failure of a FE simulation. The benefits of both structured and unstructured meshes are exploited in hybrid meshes which are composed of irregularly distributed blocks of structured meshes and are able to adapt to complex geometries maintaining good shape elements.

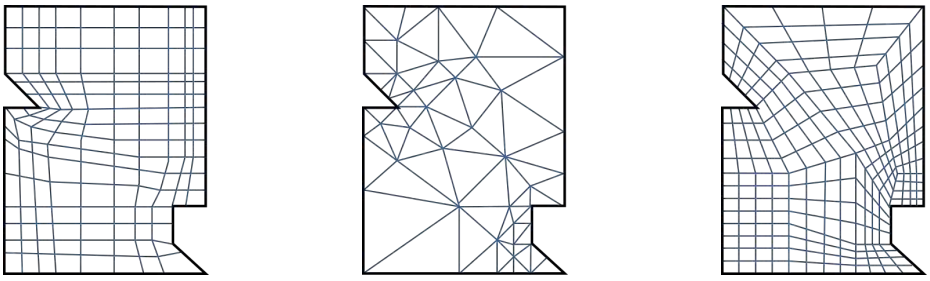

(a) Structured mesh (b) Unstructured mesh (c) Hybrid mesh

Figure 3.12 – Mesh type. According the distribution and connectivity of vertices different types of meshes can be generated. A mesh can be structured, unstructured, or a combination of both.

The shape of elements of a mesh topology is essential for the FE result quality. Distorted elements can lead to analysis errors or inability to construct trial functions and therefore abortion of the simulation. A quality measure of the shape element is the *aspect ratio*, defined as the ratio of the radius of the largest sphere containing the element over the radius of the smallest sphere contained by the element [Rice, 1985]. Elements with big aspect ratio lead to poorly conditioned matrices and should be avoided to maintain speed and accuracy in the solution.

Other than the shape, the type of the underlying elements of a mesh affects the accuracy of the FE method. Simplices (triangle, tetrahedron) are linear elements and therefore only linear

trial functions can be constructed using these types of elements. Similarly to the 1D case (see Equation 3.20, Figure 3.10), in 2- and 3- dimensional geometries the displacements solution will be approximated linearly when simplices are used. Strains and stresses in these types of elements will be approximated as constants since strain is measured by the deformation gradient (see Equation 3.6). Therefore, near the locations where stress/strain gradients are present the mesh should be extremely fine in order to approach accurately these gradients. A higher quality solution is expected when quadrilateral or hexahedral elements are used due to the bilinear or trilinear form of the trial functions, respectively.

Despite the better quality of quadrilateral and hexahedral elements, the generation of a mesh containing exclusively these types of elements is not easy especially in the 3D case. Fully automated algorithms for hexahedral mesh generation are not available and manual input from the user is required [Grosland et al., 2009]. The process of a mesh representing accurately a complex geometry can be a challenging task even for the high-experienced analyst and can require a lot of time. On the contrary, fast generation of simplicial meshes either in 2D or 3D, based on mature triangulation methods such as Delaunay triangulation [Cohen-Steiner, De Verdiere, and Yvinec, 2002], is much easier and fully automated algorithms exist, provided in various libraries [Fabri and Pion, 2009, Si and TetGen, 2006].

In medical intra-operative applications, applied biomechanical models based on FE analysis are constrained to use simplicial meshes in order to meet the time limitations of the operation if aiming to be of any practical use. It is possible to improve the solution accuracy of simplicial meshes by introducing additional nodes in the underlying elements, allowing for higher-order trial functions, at the expense of computational cost. The choice of the mesh generation method is highly dependent on the respective medical procedure.

3.5 Proposed model development

Aiming to improve LDR brachytherapy treatment planning, we propose a biomechanical model based on the FE method in order to account for the impact of edema in dosimetry. Continuum mechanics formulation is used to describe the elastic properties of the prostate and the neighbor organs of the pelvic region. Edema is described using the biphasic theory to simulate prostate tissue and edema fluid interactions.

3.5.1 Patient database

The proposed biomechanical model aims in providing a patient-specific scheme for the estimation of the edema resorption pattern and its impact on dosimetric calculations. In order to account for anatomical differences among patients and their effect on the model's output a database of 15 patients' datasets who underwent LDR brachytherapy in the radiotherapy department of the CHRU Brest was established.

A pre-implant CT acquisition was acquired for each of the 15 patients. An experienced clinician outlined the prostate, rectum, and bladder contours in each CT image acquisition. Even if not clearly visible in CT images, a contour was approximately delineated for the urethra at the central area of the prostate. Following, the same clinician constructed 15 brachytherapy treatment plans manually with respect to the dose restrictions on the CTV, rectum, and urethra as they were delineated during the contouring process. The contouring of the organs of interest

and the treatment planning were executed using the VariSeed™ v9.0 LDR treatment planning system (Varian, Charlottesville, VA). After anonymising, the CT images, the contours, and the seeds' positions were stored in the database.

3.5.2 Male pelvic region mesh

The male pelvic region is characterized by a large number of organs of different tissue composition and functionality (pelvic bones, bladder, prostate, rectum, seminal vesicles, etc.) in near proximity (see Figure 1.1). Additionally, anatomic differences among patients in this region are significant and they can affect the extent of interaction between the pubic organs under various circumstances. To account for this variation the whole pelvic region has to be represented geometrically in a complete biomechanical model.

In the proposed model of the prostate edema, a 3D tetrahedral mesh representation of the patient-specific pubic anatomy is employed. Using the ISO2MESH toolkit [Fang and Boas, 2010], a multi-domain tetrahedral mesh is derived directly from the segmentation image of the patient (see Figure 3.13).

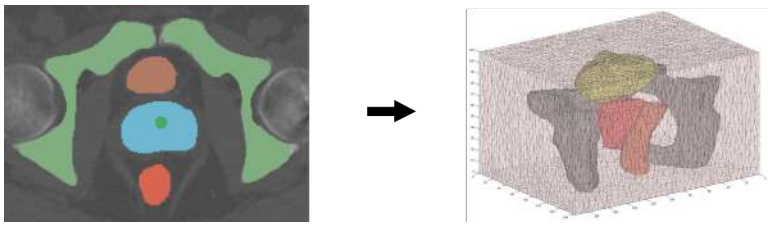

Figure 3.13 – Male pelvic region mesh. The organs of interest (prostate, urethra, bladder, rectum, and pubic arch) are represented explicitly within a soft tissue block mesh consisted of tetrahedral linear elements.

The resulting mesh is conforming on the geometrical features of the patient and consists of domains representing regions as they were denoted in the segmentation process, while the surrounding, unsegmented, structures are included in an homogeneous tetrahedral block with size equal to this of the segmented image. Prior to mesh generation, the provided segmentation images were manually updated to include the pubic arch bones. As a result, tetrahedral block meshes were generated, for the 15 patients dataset, where the prostate, the urethra, the rectum, the bladder and the pubic arch bones were considered as significant structures and were explictly represented. Furthermore, the rest proximal structures (seminal vesicles, pubic muscles, etc.) and the surrounding tissues were represented as a homogeneous tissue block.

The mean values of several mesh quality criteria for the generated meshes of the given dataset are demonstrated in Table 3.1.

Table 3.1 – Average mesh quality criteria for the given patients dataset.

Mesh quality criterion	Value
Elements number	139212
Aspect ratio	1.52
Min. dihedral angle (°)	35.65
Max. dihedral angle (°)	115.33
Jacobian	203.68

3.5.3 Edema evolution modeling

Edema, as shown in Subsection 3.2.1, is a result of the complicated mechanism of inflammation. More extensively, it results from the accumulation of excessive fluid, originated from the vascular system, in the interstitial matrix in order to suppress pathogenic agents and repair tissue damage. Swelling effects in the prostate due to brachytherapy, described as edema, are the product of a bidirectional interaction between the fluid build-up due to tissue damage, originated from needle gestures and radiation-induced cellular death, and the prostate interstitial matrix. Obviously, it is straightforward to model the phenomenon of brachytherapy-induced edema using the biphasic material assumption for the prostate (see Section 3.3.3).

Using the tetrahedral mesh representation of the patient's anatomy, a FE model was developed using the FeBIO software suite [Maas et al., 2012] in order to predict the evolution of edema over time, for the period that its presence is significant.

Prostate modeling

The biphasic mixture theory implementation of FeBIO as described by Maas et al. [2011] was used for the modeling of the prostate as a biphasic material. Additionally, excessive fluid accumulation was modeled incorporating a source term S_w in Eq. 3.15 and deriving

$$\nabla \cdot (\boldsymbol{v}^s + \boldsymbol{w}) = S_w, \tag{3.21}$$

where S_w is described by a simplified version of the Starling equation available in FeBio

$$S_w = k(p_v - p), \tag{3.22}$$

where k is a filtration coefficient, p_v defines the pressure due to the excessive fluid accumulation, and p is the biphasic mixture's (prostate) fluid compartment pressure. Recalling that edema magnitude Δ is the maximum relative prostate volume increase (see Equation 1.4), we can assume additionally that is equal to the total accumulated excessive fluid, such that

$$\int_0^{t_{max}} S_w dt = \Delta, \tag{3.23}$$

where the upper limit of the integration (t_{max}) is the time corresponding to the occurrence of the maximum prostate volume. Furthermore, the accumulation of excessive fluid was assumed to depend linearly on time and hence, by substituting a linear model of the form $p_v(t) = at + b$

in Equation 3.23, the excessive fluid pressure at any given time $t \in [0, t_{max}]$ can be expressed as

$$p_v(t) = \frac{2\Delta}{kt_{max}^2}t + p. \tag{3.24}$$

In order to close the equations system of the biphasic model, constitutive relations must be set for both the solid and fluid compartment. For the prostate solid compartment, the neo-Hookean hyperelastic material was assigned accounting for nonlinear effects of large deformations similar to previous work [Wang et al., 2016]. As for the fluid compartment of the saturated biphasic continuum, the permeability was modeled with the Holmes-Mow strain-dependent permeability model [Mow, Holmes, and Lai, 1984].

Neighbor tissues modeling

Since edema evolves in the prostate, the porous nature of the neighbor tissues can be omitted. However, significant displacements and deformations are expected depending on the edema magnitude, therefore, a biomechanical model should account for the elastic properties of these tissues.

The proposed model accounts for these properties considering the neighbor tissues as non-linear elastic materials [Fu and Ogden, 2001]. In more detail, the filling organs (rectum, urethra, bladder) were modeled using the near-incompressible Mooney-Rivlin material. The Mooney-Rivlin material was chosen similarly to previous studies [Haridas et al., 2006] in order to account for the incompressible behavior of filling organs which are undergoing large shape changes rather than volumetric increase (e.g filling/emptying process, external pressure reaction).

Considering the rest tissues of the pubic region which are not considered as of primary significance, by the proposed model, the compressible neo-Hookean constitutive relation was employed similarly to the solid compartment of the prostate for the whole pubic tissue block. The Exception were the pubic arch bones where the rigid body assumption was used, imposing zero deformation constrains in these structures.

Mechanical parameters & constraints

The range of deformation of an elastic or biphasic material (elastic solid compartment) depends on the elastic parameters of the material. These parameters control the stress-strain response of the material and can be measured experimentally. Unfortunately, the measurement of soft tissue mechanical properties is challenging. Usually, *ex vivo* measured parameter values differ from *in vivo* actual values and the assessment of the latter demands the use of techniques and equipment not widely available. Considering the mechanical parameters of the prostate and neighbor organs, knowledge is limited. Even though the advancements in ultrasound 3D elastography allow for *in vivo* evaluation of the elastic parameters of the prostate and its surroundings, available sources of data are few [Barr, Memo, and Schaub, 2012]. Even more, there is not available insight on the permeability of the prostatic tissue.

The basic parameters to describe an elastic material are the *Young modulus (YM)* and *Poisson's ratio (ν)*. The Young modulus defines the relationship between stress and strain of a material and is given by the slope of the linear part of the stress-strain diagram of the material (see Figure 3.14).

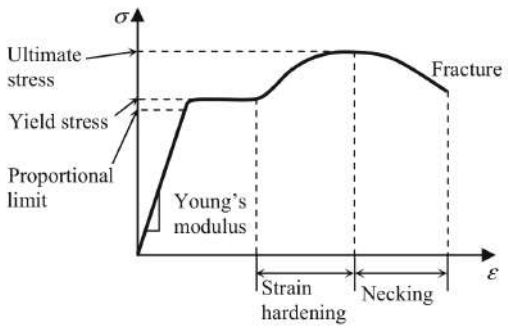

Figure 3.14 – Stress-strain diagram. The development of strains in a material depends on the amount of stress acting on it and is described by its characteristic stress-stain diagram. Under different amounts of stress the material can express different stress-strain relation (linear relation, strain hardening, necking).

The slope of the linear part of the stress-strain diagram is given by the ratio of stress over the strain of the material, and therefore the YM has measure units of pressure. YM is a stiffness measurement, where high YM values correspond to stiff solids. The second elastic parameter, Poisson's ratio, is a dimensionless parameter describing the ratio of the amount of transversal expansion over the amount of axial compression. It is a measure of the Poisson's effect, where a material subjected to a compression tends to expand in the perpendicular directions of the expansion (see Figure 3.15).

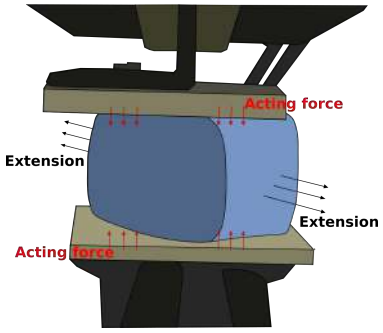

Figure 3.15 – Poisson effect. A material undergoing compression/extension tends to expand/shrink in the perpendicular directions to the compression/extension direction.

Most common materials have Poisson's ratio ranging from 0 to 0.5, where a completely incompressible material has $\nu = 0.5$. On the other hand, compressible materials, like most steel materials, demonstrate $\nu \approx 0.3$.

In our proposed model, the YM and ν mechanical parameters were assigned accordingly to previously used values for pubic region organs description in several related studies [Ahn et al., 2010, Hu et al., 2008, Barr, Memo, and Schaub, 2012, Lee, Lin, and Foskey, 2008, Li et al., 2014, and Yan et al., 2012]. Additionally, the elastic parameters of the prostate were variated between the accepted ranges in a series of experimental tests, described later, in order to investigate the effect of the prostatic elastic parameters on the edema parameters. The assigned mechanical parameters on the prostate and the neighbor organs, used in the proposed biomechanical model, are summarized in Table 3.2.

Table 3.2 – Material properties assigned on the pubic organs of interest.

Domain	Young modulus (MPa)	Poisson's ratio	Porosity	Permeability ($mm^4N^{-1}s^{-1}$)
Prostate	0.01 – 0.1[a]	0.1 – 0.45[a]	0.5	3.177E−05
Bladder & Rectum[b]	0.015 MPa	0.49	–	–
Soft Tissue	0.001 MPa	0.35	–	–

[a] Prostate drained porous solid compartment.
[b] The Young modulus and Poisson's ratio of the rectum and the bladder were converted to the c1, c2 Mooney Rivlin parameters and bulk modulus.

Having set the mathematical models of biphasic mixture theory and elasticity and having assigned the corresponding material properties to the model's domains, the proposed biomechanical model of brachytherapy-induced edema resorption pattern is completed by setting geometric and physiological constraints (boundary conditions) in the different domains. In more detail, edema was constrained in the prostate prescribing the fluid pressure on the prostatic surface to zero and pubic arch bones were constrained to zero displacements in all directions, similarly to all the surfaces of the soft tissue block (see Figure 3.13). The boundary conditions are summarized below:

- Prostate: Prescribed zero fluid pressure on prostate surface
- Pubic arch bones Prescribed zero displacement (only rotations possible)
- Soft tissue block Prescribed zero displacement of block surfaces (patient's body constrain)

3.5.4 Model validation

A very important step of the biomechanical modeling process is the validation phase. During the modeling procedure, the variation of the model's simulated results from the expected results is evaluated and improvements are introduced in the model in order to minimize the observed divergence.

In the case of modeling a physical phenomenon with a large time-span, such as edema ($t \approx 30$ days) the actual response of the phenomenon must be experimentally recorded in many time intervals in order to validate accurately the model's response. Modeling the edema resorption pattern, it would mean that a statistically sufficient number of patients should undergo several image acquisition sessions in order to monitor the edema evolution over time and furthermore, the mechanical parameters, that are expected to vary significantly among patients, should be measured. A procedure like that is not easily feasible due to the elevated financial cost, the risk of unnecessary radiation exposure (CT imaging) and the discomfort of the patients. This is one of the principle reasons that little have been done so far in the accurate modeling of brachytherapy-induced edema. However, few clinical studies are present in the bibliography and can be used for the biomechanical model validation [Sloboda et al., 2009 and

Tejwani et al., 2012]. A clinical trial to collect MRI imaging data (no radiation exposure) from 25 patients for the evaluation of edema evolution is set in our establishment, however will not be available before the end of 2017.

Therefore, the proposed model is currently validated based on the statistical results of the work of Tejwani et al. [2012] due to the demonstration of an average exponential decaying pattern of the edema similarly to other studies [Waterman et al., 1997 and Waterman et al., 1998]. Tejwani et al. measured the prostate volume using CT images of 29 patients, who have undergone LDR brachytherapy, acquired in several time intervals: 1, 9, 30, and 60 days after the operation, demonstrating a mean edema magnitude $\Delta = 0.38$ and a complete swelling resorption at Day 30.

For the validation of the proposed model, the mean values of edema magnitude at the time intervals as presented by Tejwani et al. are used as control points. The prostate fluid compartment pressure p_v is set accordingly using Equation 3.24 with $k = 1$, $t_{max} = 1$, and $\Delta = 0.38$. The mechanical parameters of the prostate and neighbor organs were not measured by Tejwani et al., therefore the mechanical properties of the neighbor organs shown in Table 3.2 were used and the prostate parameters were assessed manually to ensure $\Delta = 0.38$ at Day 1. The prostate mechanical parameters after the model assessment are given in Table 3.3 below.

Table 3.3 – Prostate elastic properties after model assessment.

Domain	Young modulus (MPa)	Poisson's ratio	Porosity	Permeability ($mm^4 N^{-1} s^{-1}$)
Prostate	0.05	0.4	0.5	3.177E−05

[a] These mechanical properties were shown to have the optimal fitting with the reference ground truth measurements of Tejwani et al., 2012 used in this study.

The excessive fluid accumulation was "*switched off*" after Day 1 by setting $p_v = 0 \ \forall t \in (1 - 30]$ and the resorption of the edema was therefore controlled exclusively by the associated mechanical parameters of the prostate and the surrounding organs. Fitting manually the model's response at Day 1 with the reference data of Tejwani et al., the validity of the model was evaluated by its ability to approximate the edema magnitude values at the rest control points: 9, 30 days. The control point Day 60 was discarded since edema was resolving by Day 30 in the clinical case study of Tejwani et al.

The proposed biomechanical model was simulated on the 15 patients dataset available and the mean edema magnitude values at time intervals: 1, 9, 30 days produced by the model were compared with the corresponding reference values, considering the standard deviation of the given dataset. The biomechanical model was able to successfully approximate the reference edema magnitude values at the given control points with a maximum uncertainty of 1.3%. Additionally, the exponentially decaying resorption pattern described in previous studies was produced (see Figure 3.16).

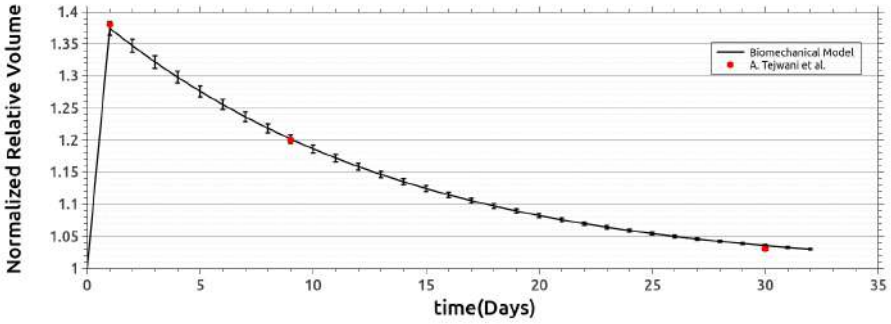

Figure 3.16 – Edema mean resorption pattern. The edema resorption pattern of the proposed model was validated with the finding of Tejwani et al. [Tejwani et al.] demonstrating maximum uncertainty of 1.3%

Describing the edema resorption pattern by the proposed biomechanical model we are able to investigate the effect of the tissue mechanical properties on the evolution of the edema aiming to extend the insight on the edema characteristics in such ways that, was not feasible with the previous existing approaches based on macroscopic observations.

3.6 Prostate mechanical parameters effect on edema

Edema resorption pattern shows significant variations among patients, both in terms of edema magnitude and edema half-life. Until now, a clear correlation between the observed variations and clinical variables, such as age, hormonal therapy uptake, needles gestures, seed activity, etc. is not available (see Section 3.1). The difficulty defining the significant edema parameters underlies in the anatomical and physiological variations among patients and in the difficulty quantifying these variations.

In order to investigate the effect of these variations on the edema parameters (magnitude, half-life) we consider two theoretical scenarios. Recalling the biphasic nature of the prostate, it is natural to assume that the edema characteristics will depend both on the initial cause (excessive fluid accumulation) and the resulting tissue response (elastic deformation) of the prostate. Considering the two elastic parameters used in the biomechanical model (YM, ν) a *preliminary test* was first done to evaluate the dependence of both edema magnitude and half-life on these values. After this preliminary evaluation, the first scenario, *Young modulus effect test*, was executed in order to investigate the effect of the prostate elastic properties on the edema resorption pattern. Subsequently, the second scenario, *Excessive fluid pressure effect test*, was performed where the effect of the extent of fluid accumulation on the edema resorption pattern was investigated.

Simplifying the investigation process, only the parameter of interest was considered variable while keeping the rest parameters constant in the corresponding tests. In more detail, in the *Young modulus effect test* the YM of the prostate was considered variable in the interval of [0.01MPa, 0.1MPa] while the rest parameters of the prostate were considered as given in Table 3.3 and the mechanical parameters of the rest organs as described in Table 3.2. In *Excessive fluid pressure effect test*, where the excessive fluid accumulation effect was investigated, all the elastic parameters were held constant as given in Tables 3.2, 3.3 and only the excessive fluid pressure p_v was considered variable in such a way so the resulting edema magnitudes under

examination were: $0.1, 0.2, 0.38, 0.65$. The configuration of the preliminary, *Young modulus effect*, and *Excessive fluid pressure effect* tests are summarized below:

- Preliminary — Parameters as in Tables 3.2, 3.3. Variable prostate YM (0.01 - 0.1 MPa), or prostate v (0.1 - 0.45)
- Young modulus effect test — Parameters as in Tables 3.2, 3.3. Variable only prostate YM (0.01 - 0.1 MPa)
- Excessive fluid pressure effect test — Parameters as in Tables 3.2, 3.3. Variable p_v ($\Delta = 0.1, 0.2, 0.38, 0.65$)

3.6.1 Preliminary test

Before testing the effect of edema magnitude and elastic parameters variability in the edema resorption pattern, a preliminary test on the significance of elastic parameters was performed. The aim of this test was to discriminate the most significant prostate elastic parameter (YM, v) in the variation of edema parameters (magnitude, half life).

The edema magnitude and half-life parameters were measured on the given patient dataset in two experimental setups. In the first setup, the edema parameters were measured for a range of Poisson's ratio from 0.1 to 0.45 with the rest parameters fixed, while in the latter setup the varying parameter was the prostate Young modulus in a range from 0.01 MPa to 0.1 MPa (see Figures 3.17 and 3.18).

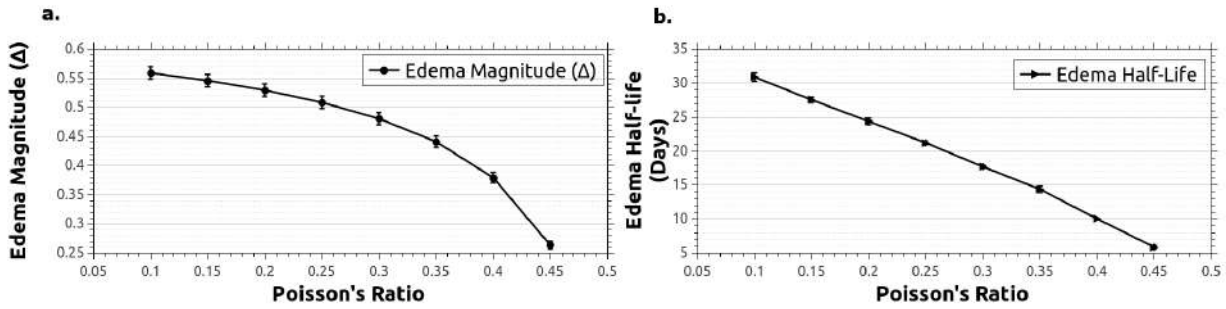

Figure 3.17 – Poisson's ratio effect. The effect of variations of the Poisson's ratio of the prostate on the edema characteristics (magnitude, half-life) is demonstrated.

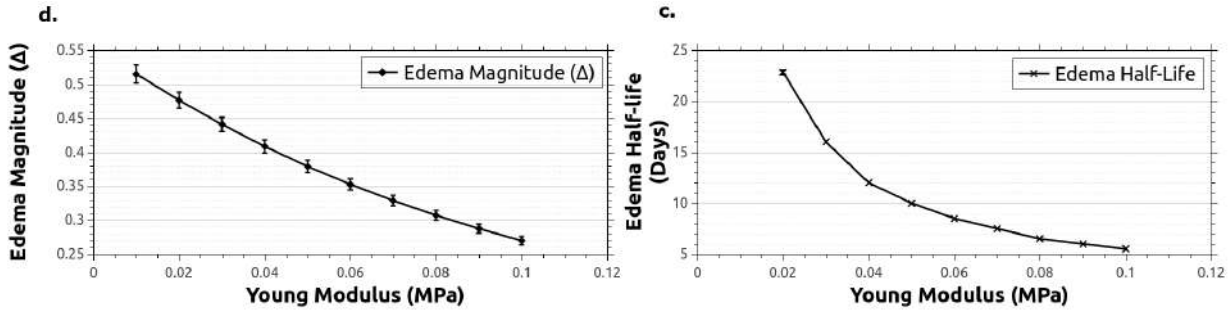

Figure 3.18 – Young modulus effect. The effect of variations of the Young modulus of the prostate on the edema characteristics (magnitude, half-life) is demonstrated.

As a result of this experiment, a stronger dependence of the edema parameters on the prostate YM was found. The increase of stiffness (higher YM), as demonstrated by the proposed model, leads to a faster decrease of both edema magnitude and half-life than the increase of incompressibility (higher v). Considering the variations of patient anatomy and tissue composition (e.g cancer extent, inflammation) a high variability of prostate YM among patients is observed, as measured by *in-vivo* shear wave elastography [Barr, Memo, and Schaub, 2012]. For this reason, the effect of prostate YM on the edema parameters is investigated in *Young modulus effect test*.

3.6.2 Young modulus effect test

In this experimental setup, the edema resorption patterns for the extreme YM values used in the Preliminary test (0.01 MPa, 0.1 MPa) were calculated. The resulting patterns were evaluated comparing them with the resorption pattern calculated during the validation process of the model (Subsection 3.5.4), in which we will refer from now on as the *"mean edema resorption pattern"*. As demonstrated in the Preliminary test, the edema magnitude at Day 1 for the YM = 0.01 MPa setup was superior (0.5 ± 0.013) than the edema magnitude in the mean edema resorption pattern setup (0.38 ± 0.011), while in the YM = 0.1 MPa setup the edema magnitude was inferior (0.27 ± 0.006). Moreover, more interestingly, large differences in the overall pattern of edema resorption were observed in the three compared setups (see Figure 3.19).

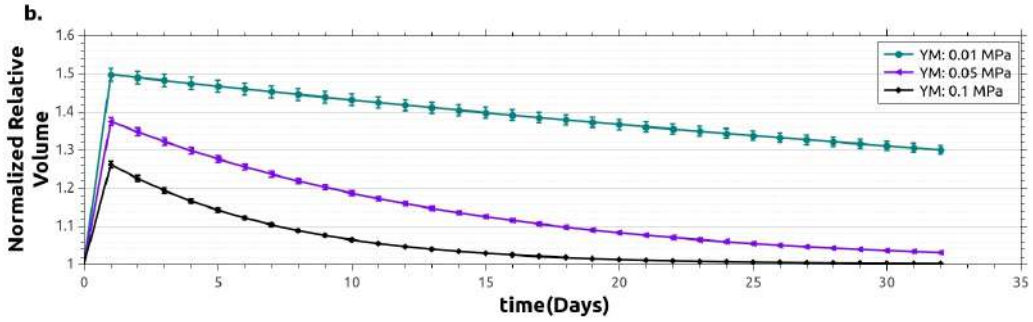

Figure 3.19 – Prostate stiffness effect. The stiffness variations of the prostate expressed in terms of Young modulus affect the edema magnitude and half-life. For high stiffness exponential resorption pattern is demonstrated while for low stiffness the resorption pattern becomes linear.

As demonstrated, both the edema magnitude and the overall edema resorption pattern depend on the prostate stiffness. A stiff prostate (high YM) will constrain the tissue expansion (swelling) caused by a given excessive fluid pressure and internal forces will support the edema resorption resulting in a fast (exponential) edema decrease. On the contrast, in a less stiff prostate (low YM) the resisting forces to the excessive fluid build-up will be smaller leading to increased swelling for a given excessive fluid pressure and persisting edema with longer half-life.

This finding is considered of great importance since the observed extended variation in edema half-life [Waterman et al., 1998, Chira et al., 2013, and Sloboda et al., 2012] can be associated with the extended YM variability among patients [Barr, Memo, and Schaub, 2012]. Moreover, the linear edema resorption pattern in the YM = 0.01 MPa is in agreement with the linear edema resolution observed by Sloboda et al. in their study [2009].

3.6.3 Excessive fluid pressure effect test

In this experimental setup, the variable of interest was the excessive fluid pressure. While maintainig all the mechanical parameters of the model constant (see Tables 3.2, 3.3) different excessive pressure values were chosen, setting four different cases with edema magnitude: 0.1, 0.2, 0.38, 0.65 respectively. In all the four cases, as calculated from the proposed model, no significant effect of the excessive fluid pressure was observed on the edema resorption pattern (see Figure 3.20). This finding in combination with the findings of *Young modulus effect test* (subsection 3.6.2) demonstrates that the excessive fluid pressure controls the extent of the edema (excessive fluid accumulation), while the overall response of the prostate to the phenomenon is attributed to its elastic parameters which also constrain the magnitude of edema due to internal resisting forces building in the solid compartment of the gland.

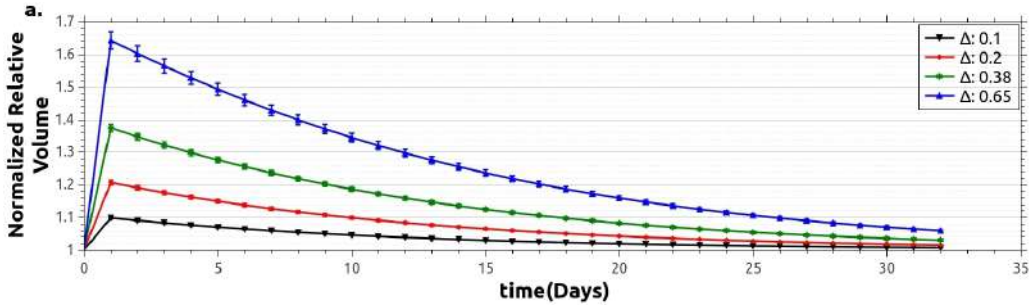

Figure 3.20 – Excessive fluid pressure effect. The amount of excessive fluid pressure applied on the prostate tissue affects the total edema magnitude Δ, while no significant differences are shown in the resorption pattern in the given experimental setups ($\Delta = 0.1, \Delta = 0.2, \Delta = 0.38, \Delta = 0.65$).

3.7 Edema biomechanical model summary

The proposed biomechanical model based on the method of finite elements demonstrated the ability to take into consideration previously non-investigated parameters in the approximation of the edema resorption pattern. Elastic parameters of the prostate and neighbor organs in combination with the excessive fluid pressure build-up due to inflammation were shown to be key components of the evolution of the edema. In contrast with previous models, the proposed model considered the effect of the tissue elastic properties on the edema evolution pattern. Therefore, the edema pattern of a patient could be predicted if elastic properties information were available.

The variations of edema extent among patients were shown to be controlled by differences that can be observed in the amount of accumulated fluid and elastic parameters of the tissue, such as the Young modulus. In addition, the Young modulus was shown to be the most significant parameter in the observed variation of edema half-life and edema resorption pattern among patients. The controversial exponential and linear patterns demonstrated in other studies can be attributed, correspondingly to the presented model, to variations in the Young modulus of the prostate among patients.

Having developed a patient-specific biomechanical model, it is of great interest to investigate its impact on the dosimetry. By simulating the expected edema resorption pattern during the

operation, dosimetric corrections could be imposed to the treatment plan leading to an improved outcome of the procedure with lower risk of complications.

CHAPTER

4

DYNAMIC MONTE CARLO DOSIMETRY

In order to account for volumetric changes in the patient's anatomy, a biomechanical FE model was proposed in the previous chapter. Here, this information is used to update the intra-operative dosimetry. Principles of 3D rasterization are briefly reviewed and a volumetric resampling algorithm based on these principles is introduced. Using this algorithm the computed deformation of the tetrahedral mesh is mapped on the initial CT image of the patient. Deforming the patient's CT image at different time intervals during the edema evolution, dynamic Monte Carlo dosimetry is introduced. Our purpose is to account for the effect of edema on dosimetry. Then, the post-operative dosimetry can be accounted during treatment planning.

Afin de tenir compte des changements volumétriques de la prostate du patient en fonction du modèle biomécanique des méthodes de rééchantillonnage sont présentés dans ce chaptire. Le but est de pouvoir mettre à jour la dosimétrie intra-opératoire. Les principes du tramage 3D sont brièvement expliqués et un algorithme de rééchantillonnage volumétrique est proposé. En utilisant cet algorithme, la déformation calculée du maillage tétraédrique est cartographiée sur l'image CT initiale du patient. En déformant l'image CT du patient à différents intervalles de temps pendant l'évolution de l'œdème, on peut introduire la dosimétrie Monte Carlo dynamique. Ensuite, la dosimétrie post-opératoire peut être prise en compte lors de la planification du traitement.

"Progress lies not in enhancing what is, but in advancing toward what will be."

— Gibran Khalil Gibran

4.1 Voxelized image deformation

In Chapter 3, a biomechanical model for the simulation of the brachytherapy-induced edema resorption pattern was proposed. The time evolution of the edema was associated with the mechanical characteristics of the prostate and the proximal organs. Based on the finite elements (FE) method and using a tetrahedral mesh discretization of the patient's pubic anatomy the deformation of the prostate and near proximity organs can be calculated for different time intervals during the resorption time of the edema. This information can be exploited to improve dosimetry calculations, considering volumetric changes of the prostate and movement of the seeds from the planned locations during the time span of the edema.

However, the application of this information is not straight forward. Medical image data representation is generated and stored following a voxelized data structure. Moreover, most of the Monte Carlo (MC) dosimetry algorithms, such as the one employed in our developments (see Chapter 2), are based on this voxelized representation of the medical image to estimate the dose deposition accounting for voxel-level tissue heterogeneities. Consequently, the deformation information of the patient's anatomy tetrahedral representation, as generated by the biomechanical model, should be mapped to the initial voxelized image representation in order to be exploited in the dosimetric calculation.

The mapping of a geometrical object (tetrahedron) to a voxelized structure is similar to the common task of modern 3D graphics were primitives (triangles) in 3D space are mapped to a pixelized structure (screen) for realistic visualization. Based on rasterization, a 3D computer graphics technique, a resampling method for deformation of voxelized images was developed recently by Aguilera et al. [2015]. Exploiting GPU computing, this algorithm applies the deformation of a tetrahedral model on its respective volumetric representation in interactive time.

This algorithm was employed in our development to apply the calculated deformation from the biomechanical model of the patient's anatomy to the initial voxelized image at several time intervals during the simulated edema resorption period. In this way, dynamic volumetric changes during dosimetry calculations are considered. Furthermore, seeds' displacements that follow the prostate deformation during the edema resorption period were considered based on the principles of the applied resampling method.

4.1.1 Rasterization

Rasterization is currently the most popular rendering technique of 3D scenes. It involves the conversion of vectors and geometrical shapes into pixels for display on the computer screen. The rasterization method has low computational cost and can rapidly produce real-time 3D graphics. Additionally, it allows for high parallelism, therefore, it is the base of GPU rendering [Owens, 2007].

During rasterization, a polygonal shape (eg. triangle) is projected onto the screen using perspective projection [Novins, Sillion, and Greenberg, 1990]. The coordinates of the triangle's vertices are, therefore, converted in raster (pixel) coordinates. Subsequently, the pixels that are included in the projected triangle are identified and the color properties of the triangle are assigned to them. The most common method to identify the pixels included in a given triangle is using the edge function as introduced by Pineda [1988].

Considering two points on a plane with coordinates (X, Y) and (X+dX, Y+dY) respectively, an edge is described by a vector defined by these two points. A coincident line to this edge divides the plane into two regions (left, right). Points lying on this plane can be classified as points belonging to the left or the right side of the line or as points belonging on the line (see Figure 4.1a).

The position of a point in this plane in respect with the edge can be characterized by the edge function

$$E(x, y) = (x - X)dY - (y - Y)dX, \tag{4.1}$$

where the under examination point will lie on the right side of the line if $E(x, y) > 0$, on the left side if $E(x, y) < 0$, and exactly on the line if $E(x, y) = 0$. Now, for any convex polygon described by N vertices with coordinates (X_i, Y_i), where $0 < i < N$ and $(X_0, Y_0) = (X_N, Y_N)$, the edge function between two adjacent vertices can be computed incrementally. Considering points that lie on an edge of the convex polygon as internal points of the polygon, an inclusion test can be executed for each given point of the plane (see Figure 4.1b).

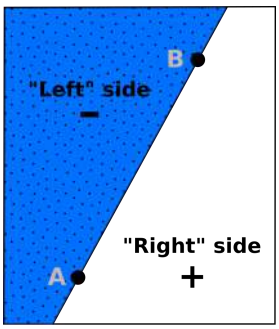

(a) Two points 2D space division in left(−) and right(+) areas

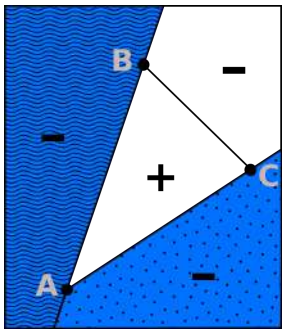

(b) Polygon 2D space division in external and internal areas

Figure 4.1 – Edge function division. Any two given points divide the plane into two regions, left and right from the edge. Introducing the edge function 4.1, the position of each point of the plane with respect to the edge can be computed.

The edge function test is employed in the rasterization process to discriminate pixels that are interior to the convex polygon defined by the projected vertices of the geometrical shape to be rendered. On these pixels, the color properties of the shape will be assigned according to the values stored in the projected vertices (see Figure 4.2). Usually, the vertices will not have the same color values and therefore the color of the shape's pixels will have to be acquired by an interpolation of the color values stored in its vertices. The pixels' color value computation inside a triangle can be performed conveniently by introducing the barycentric coordinates system.

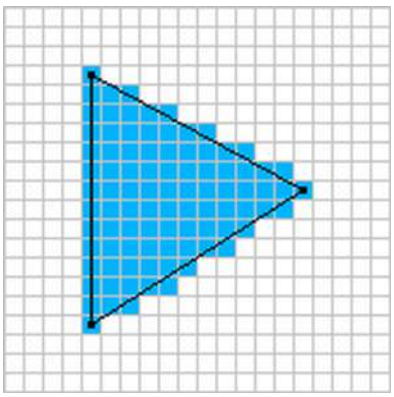

Figure 4.2 – Polygon rasterization. An arbitrary polygon can be represented as a union of triangles. Projecting the vertices of these triangles on the screen and interpolating the color values stored in the triangle vertices on the bounded pixels, the triangles and eventually the polygon can be rasterized on the screen.

4.1.2 Barycentric interpolation

The rasterization task described in Subsection 4.1.1 can be divided into two steps; projection and color properties assignment. *Barycentric interpolation* is an efficient method to interpolate the color values of the projected polygon's vertices in its interior pixels by mapping the coordinates of the vertices in a barycentric coordinates system. The idea of barycentric interpolation is based on the work of Möbius [1827].

The principle of barycentric interpolation lies in finding a point x, such that for a fixed set of points x_i, where $i = 0, \ldots, n$, and weights w_i associated with these points, the point x is the barycenter of the point-set given as

$$\boldsymbol{x} = \frac{\sum_i^n w_i \boldsymbol{x_i}}{\sum_i^n w_i}. \tag{4.2}$$

The weights w_i can be expressed as a function of the point $\boldsymbol{x}$, and they represent the barycentric coordinates of $\boldsymbol{x}$ with respect to the $\boldsymbol{x}_i$ points. The barycentric coordinates are homogeneous, hence they can be normalized, such that

$$\sum_i^n b_i(\boldsymbol{x}) = 1, \tag{4.3}$$

where b_i are the barycentric basis functions (normalized weights). Additionally, each point $\boldsymbol{x}$ can be expressed as the linear combination

$$\boldsymbol{x} = \sum_i^n b_i \boldsymbol{x_i}. \tag{4.4}$$

Moreover, the barycentric basis functions b_i satisfy the Lagrange property, $b_i(\boldsymbol{x}_j) = \delta_{ij}$, such that the barycentric basis function $b_i(x_i) = 1$ at the corresponding point i and zero on the rest $n - 1$ points of the point-set.

Returning to the rasterization of a polygon, for simplicity consider a triangle T of area A, the b_i barycentric basis functions, with $i = 1 \ldots 3$, are associated with the vertices of the

triangle T. Considering now a point P inside the triangle T, it can be expressed as a linear combination of the three barycentric basis functions, b_1, b_2, b_3. The point P divides the given triangle into three sub-triangles with areas A_1, A_2, A_3, such as $A = A_1 + A_2 + A_3$ (see Figure 4.3). Assuming that the point P approaches one of the three vertices, e.g x_1, then $A_1 \rightarrow A$ and $A_2, A_3 \rightarrow 0$. It follows that, the barycentric basis functions b_i can be expressed as the ratio of the corresponding sub-area A_i over the total area A. It is straightforward to prove that the Lagrange property

$$b_i = \frac{A_i}{A} = \begin{cases} 1, & \text{if } x = x_i \\ 0, & \text{if } x = x_j \end{cases}, \tag{4.5}$$

and the partition of unity property (see Equation 4.3)

$$\sum_i^n b_i = \sum_i^n \frac{A_i}{A} = 1 \tag{4.6}$$

are satisfied. Subsequently, employing the barycentric property (see Equation 4.4), any point P inside the triangle T can be expressed as a linear combination of the given basis function

$$\boldsymbol{P} = \frac{A1}{A}\boldsymbol{x}_1 + \frac{A2}{A}\boldsymbol{x}_2 + \frac{A3}{A}\boldsymbol{x}_3. \tag{4.7}$$

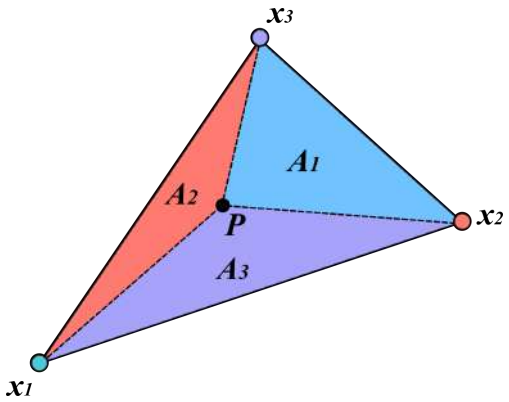

Figure 4.3 – Barycentric coordinates. Any point internal in a triangle can divide the triangle in three areas by connecting it with the vertices of the triangle. The barycentric coordinates of this point can be given in terms of ratios of the sub-areas with the total area.

The barycentric interpolation in a triangle can be generalized in 3D introducing the tetrahedral barycentric interpolation, where any given internal point P' subdivides a given tetrahedron T' into four sub-tetrahedra with volumes V_1, V_2, V_3, V_4 respectively and the point P' can be expressed in tetrahedral barycentric coordinates as

$$P' = \frac{V1}{V}\boldsymbol{x}_1 + \frac{V2}{V}\boldsymbol{x}_2 + \frac{V3}{V}\boldsymbol{x}_3 + \frac{V4}{V}\boldsymbol{x}_4, \tag{4.8}$$

where $\boldsymbol{x}_1, \boldsymbol{x}_2, \boldsymbol{x}_3, \boldsymbol{x}_4$ are the vertices of the tetrahedron T' and V is its volume. Applying the method of rasterization using 3D barycentric interpolation, the deformation field described by

a tetrahedral mesh can be rasterized into a volumetric model. A volumetric model resampling algorithm based on this technique is employed in our implementation for the application of the proposed biomechanical model's deformation to the original patient's CT image. Implementation details of this algorithm as it was presented by Aguilera et al. [2015] are described in the following.

4.1.3 Volumetric model resampling

The principal uncertainty-inducing factors in LDR brachytherapy dosimetry are prostate volumetric changes and associated seeds' movement resulting from the formation and resorption of prostatic edema. Introducing the previously proposed biomechanical model (see Chapter 3), prostate volumetric changes can be predicted considering patient-specific anatomical and elastomechanical variations based on the finite elements (FE) method. These volumetric changes are interpreted in terms of a displacements field calculated on the tetrahedral mesh representation of the patient's anatomy and therefore they can not be incorporated directly into the dosimetric calculation. Dosimetric calculations, such as the calculations performed by the Monte Carlo (MC) dosimetry algorithm used in our development, are usually performed on the voxelized representation of the patient's anatomy provided from CT acquisitions. In order to incorporate the information produced by the biomechanical model in the dosimetry calculation, a mapping of the deformation field from the tetrahedral mesh representation back to the initial voxelized volume representation is required.

With regard to this mapping, a fast *volumetric model resampling* (VMR) algorithm proposed by Aguilera et al. [2015] was employed. Exploiting GPU parallelization the VMR algorithm was able to perform a deformation mapping from a tetrahedral representation consisting of 128×10^3 tetrahedra to a voxelized volume of 13×10^6 voxels in ≈ 30 ms. The deformation mapping is based on 3D rasterization, however, a preprocessing step is performed to decouple the deformation process from the rasterization, therefore deformation fields calculated on high-resolution meshes can be handled without decreasing the performance of the algorithm.

Preprocessing step

In more detail, in the preprocessing step, the voxelized volumetric model is treated as a regular 3D grid, where each voxel's value is assigned to a vertex located in the center of the voxel, where 8 adjacent nodes form a regular 8-node hexahedron. Subsequently, each hexahedron is decomposed in five adjacent tetrahedra (5-T decomposition) constructing an implicit continuous tetrahedral mesh (sampling mesh, see Figure 4.4a). In each deformation step, the deformation field, stored on the vertices of the biomechanical model's tetrahedral mesh is mapped statically on the vertices of the sampling mesh.

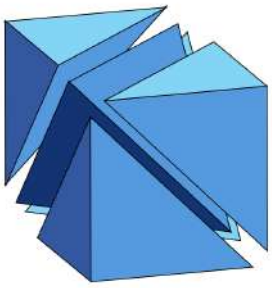

(a) Regular hexahedron 5T decomposition

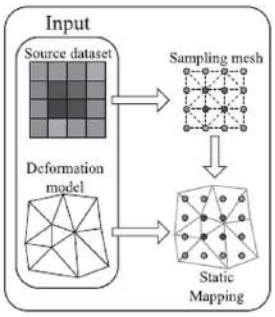

(b) Resampling algorithm pipeline

Figure 4.4 – VMR algorithm preprocessing pipeline. A preprocessing step in the VMR algorithm consists of a 5T decompsition of the initial regular mesh of the volume model in a tetrahedral sampling mesh where the deformation field of the deformation model is statically mapped on the vertices of the sampling mesh.

3D Rasterization

Following the deformation, the sampling mesh is rasterized in a target 3D regular grid. For each tetrahedron of the sampling mesh, its axis-aligned bounding box is computed and an inclusion test is performed on the content voxels to outline voxels which are bounded from the current tetrahedron. The inclusion test is performed calculating the barycentric coordinates of the voxels and the values stored in the tetrahedron's vertices are interpolated through the bounded voxels (see Figure 4.5). As a result, the deformation field, as calculated from the biomechanical model, is integrated in the medical image of the patient (volumetric model) which is resampled interactively for each deformation state (edema resorption state).

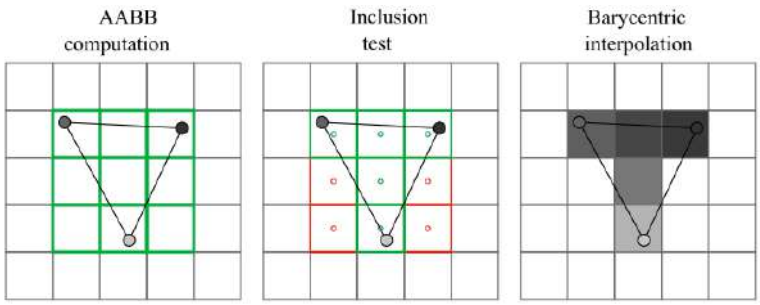

Figure 4.5 – VMR algorithm 3D rasterization. In the 3D rasterization process, voxel values of the initial volumetric model stored in the vertices of the sampling mesh are interpolated using tetrahedral barycentric interpolation to the bounded voxel of the target 3D regular grid.

4.1.4 CT image resampling

Applying the deformation field of the biomechanical model on the patient's CT image, using the presented VMR algorithm, we are able to incorporate shape and volume changes on the CT image and eventually in the dosimetry. This permits to propose a dynamic dosimetry scheme based on deformed CT images, of a given patient, in different chosen time intervals.

Considering a given prediction of the edema resorption pattern, the patient's image datasets can be resampled according to the expected deformation in the different time intervals. In this way, dosimetry can be performed on deformed images approaching more accurately the current anatomical state of the patient, rather than on the initial images which correspond to a previous state.

In order to perform dynamic MC dosimetry, both the CT and the segmentation images of the patient must be deformed appropriately. While the former image can be used in MC simulations for particle tracking and dose deposition calculation, the latter is used for volumetric information extraction from the regions of interest (ROI), useful for the measurement of various dose metrics. Furthermore, the segmentation image can be used as a computational phantom, substituting the CT image in MC simulations.

The employed VMR algorithm utilizes barycentric interpolation for the resampling of the image from the initial state to the deformed. Obviously, due to the interpolation error, the resampled values of some voxels are expected to differ from the actual ones. In the CT image deformation, where Hounsfield unit (HU) values are stored in the voxels, erroneous HU values are expected in some voxels. However, the observed error is significantly smaller than the range of HU values in any given organ, hence interpolation errors do not pose any complications in material definition during the MC dosimetry. Furthermore, no deformation artifacts are observed in rigid structures, such as the pubic arch bones. Additionally, sharp features, such as calcifications are preserved during the resampling process, allowing for MC dosimetric simulations of similar accuracy through all the deformation states under consideration (see Figure 4.6).

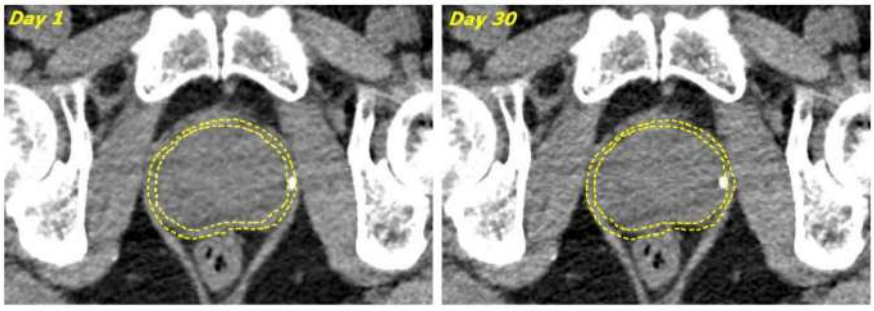

Figure 4.6 – VMR sharp features preservation. The volumetric resampling of the gray-scale volume model (CT image) is free from artifacts during the deformation application. Rigid structures, such as pubic arch bones are not deforming and sharp features such as calcifications are maintained in the resulting image.

On the contrary, even small interpolation errors even are significant during the deformation of the patient's segmentation image where specific discrete integer values are assigned to the voxels of the underlying ROIs. All the voxels associated with a specific ROI (e.g prostate) are assigned a unique value (label) which should be maintained under any deformation. If this restriction is not respected, erroneous dose metrics will be measured if dosimetry is performed on the deformed images. To avoid this complication, special processing is required. Fortunately, the interpolation error is present only in a small number of voxels and the deformed segmentation images can be corrected by treating the voxels containing erroneous values as holes in the labeled ROIs and applying a standard hole filling filter.

4.1.5 Seeds displacement

In a dynamic LDR brachytherapy dosimetry scheme, additionally to the prostate volumetric changes, the displacement of brachytherapy seeds during the edema resorption period has to be considered. While edema resorbs, the seeds are displaced from their implantation positions following the volumetric change of the prostate. This displacement results in a different final dose distribution than the one estimated during the implantation, as shown comparing intra-operative and post-implant dosimetry. Taking into consideration the displacement of the seeds during the treatment planning could reduce significantly the variation between intra-operative and post-implant dosimetry (actual dose deposition). In order to take into account the seeds' displacements in the dosimetry, we propose a dynamic dosimetry scheme based on the previously developed biomechanical model (see Chapter 3).

In real conditions, the seeds are expected to contribute in the overall deformation of the prostate rather than follow it, due to their different material properties (stiffness, density), and are expected to undergo a rigid motion (translation, rotation) during the deformation period. In favor of accounting for the complete rigid motion of dozens of seeds, implanted in a usual standard treatment plan, an extremely locally refined mesh is required to establish the biomechanical FE model. Such a complicated mesh is cumbersome to be generated in intra-operative time and increases greatly the computational cost, therefore, for this reason, no seeds contribution in the prostate was considered in our development.

The seeds are assumed to follow the deformation of the prostate linearly, rather than contributing to it. In order to update the seeds locations, in each time interval of the dynamic dosimetry simulation, the displacement field calculated by the biomechanical model is mapped on the initial seeds locations using the VMR algorithm in a similar manner as was used in the volumetric model resampling.

In more detail, an inclusion test is performed on the seeds to the initial (undeformed) tetrahedral mesh representation by firstly expressing the centroids of the respective seeds in barycentric coordinates. In each time interval, the deformation field stored in the vertices of the bounding tetrahedra is interpolated by means of barycentric interpolation on the centroid positions of the seeds, updating their locations in respect to the undergoing deformation (see Figure 4.7).

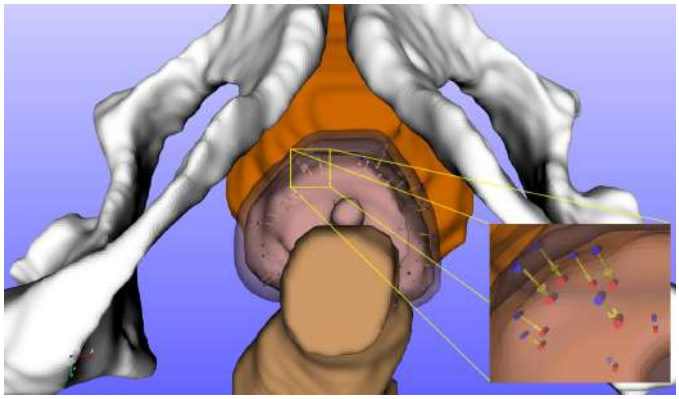

Figure 4.7 – Seeds movement during deformation. The displacements of seeds following the volumetric changes of the prostate can be estimated assuming translational moves (no rotations) and linear relation to the volumetric change using the VMR algorithm.

By mapping the deformation field, calculated by the biomechanical model, to the original patient image datasets (CT and segmentation) and the initial seeds positions, it is possible to consider volumetric changes and seeds' movement associated with the edema in different time intervals. This development enables the establishment of a dynamic MC dosimetry scheme in LDR brachytherapy that could eventually improve the outcome of the treatment by improving the treatment planning quality.

4.2 Dynamic dosimetry scheme

In LDR brachytherapy, the quality of the treatment's outcome depends strongly on the accurate implantation of the seeds at the selected locations during the treatment planning procedure. Volumetric changes and seeds movement associated with the formation of edema can lead to a significantly different dose distribution as observed in post-implant dosimetry, leading often to increased toxicity.

Following the developments of the edema biomechanical model and the incorporation of the resulting deformation in the patient's image data sets and initial seeds positions, our objective is to account during the operation for post-implant dose variations. In order to achieve that, a dynamic dosimetry scheme is proposed to take into consideration edema-associated dose deviations between intra-operative and post-implant dosimetry. The objective is to modify the treatment plan according to a prediction of the volumetric changes and seed displacements, linked to the edema resorption pattern, in order to minimize the observed difference between the intra-operative and post-implant dosimetry.

Instead of calculating the dose to be deposited considering the intra-operative prostatic volume and the planned seed positions, the edema resorption pattern is incorporated to estimate the prostate volumetric changes and the associated seed displacements in different time intervals during the resorption period. The dose to be deposited during each time interval is calculated and accumulated to the total deposited dose.

4.2.1 MC dose to real dose conversion

In MC dosimetry simulations the dose deposited in a voxel i is given by

$$D_{(i)MC} = \frac{E_i}{m_i}, \tag{4.9}$$

where E_i is the energy deposited in the voxel i for the total number of simulated particles (P_{MC}) and $m_i = v \times \rho_i$, is the voxel's mass, given as the product of the voxel volume v and the density ρ_i of the underlying material in voxel i. Then, the actual deposited dose is easily calculated by

$$D_{Real} = D_{MC} \times \frac{P_{Real}}{P_{MC}}, \tag{4.10}$$

where P_{Real} is the real number of emitted particles. The number of emitted particles from a given radiation source can be expressed as the product of its radioactivity $A(t)$ (disintegrations per second) and the exposure time t (seconds). In LDR brachytherapy interventions a number N_s of sealed radioactive sources (seeds) are implanted permanently in the prostate, therefore,

the exposure time is theoretically infinite (total decay time). The number of real particles hence can be calculated from

$$P_{Real} = N_s \kappa \int_0^{\infty} A(t) dt, \tag{4.11}$$

where κ is the average number of photons emitted per disintegration and depends on the used radionuclide (e.g $\kappa = 1.476$ for ^{125}I seeds [Rivard et al., 2004]). Incorporating the radioactive decay formula in Equation 4.11 we derive

$$P_{Real} = N_s \kappa \int_0^{\infty} A_0 e^{-\lambda t} dt \tag{4.12a}$$

$$P_{Real} = N_s \kappa \int_0^{\infty} A_0 e^{-\lambda t} dt \tag{4.12b}$$

$$P_{Real} = N_s \kappa A_0 \left[-\frac{1}{\lambda} e^{-\lambda t} \right]_0^{\infty} \tag{4.12c}$$

$$P_{Real} = N_s \kappa \frac{A_0}{\lambda} \tag{4.12d}$$

where A_0 is the initial radioactivity and λ the decay constant. The result of Equation 4.12 can be incorporated in Equation 4.10 in a conventional dosimetry simulation scheme, where no volumetric changes or seeds' movement is considered, to convert the simulated dose in the actual deposited dose. However, in the dynamic dosimetry scheme where volumetric changes and seeds' movements are considered the Equations 4.12c and 4.12d are no more valid.

In the proposed dynamic dosimetry scheme the exposure time is partitioned in two time periods, the edema resorption period (first 30 days after operation) and the after-edema period where no volumetric changes or seed movements are present. Furthermore, the edema resorption period is discretized in n time intervals assuming zero volumetric changes and seed movements during the time span of each interval. Then, the dose deposited during the total exposure time can be described, in a dynamic manner, as the sum of the dose fractions calculated during each time interval, expressed by

$$D_{Real} = D_{MC} \times \frac{N_s \kappa A_0}{P_{MC}} \times \left\{ \sum_{j=0}^{n-1} \left[-\frac{1}{\lambda} e^{-\lambda t} \right]_j^{j+1} + \left[-\frac{1}{\lambda} e^{-\lambda t} \right]_n^{\infty} \right\}. \tag{4.13}$$

The accuracy of the dynamic dosimetry calculation, as given by Equation 4.13, depends on the discretization level of the edema resorption period. In the lower limit where $n = 1$ the result will be equivalent to the conventional dosimetry, while for $n \to \infty$ the dynamic dose calculation will be continuous. The choice of the number of time intervals n will be, therefore, a trade-off between accuracy and computational time. Additionally, the dose-rate of the seeds should be considered during the choice of the time intervals since higher dose-rate will require shorter time intervals for a realistic result. In our development, where ^{125}I seeds were used in the simulations (STM125I, Bard Medical Division, Covington, GA, USA [Kirov and Williamson, 2001]), the edema resorption period was discretized in 30 time intervals of 1 Day duration similar to the time step of the biomechanical model calculation. However, no significant dosimetric difference was found when the time interval was relaxed in 2 Days duration (15 intervals).

4.2.2 Dynamic vs Conventional dosimetry

In order to investigate the capability of the proposed dynamic dosimetry scheme to improve intraoperative dosimetry, a MC dosimetry study was performed. Using the deformation fields computed in the *Young modulus effect* and *Excessive fluid pressure effect* experiments, presented in Chapter 3, the 15 patients dataset was extended in order to account for the effect of various edema characteristics as well as various prostate elastic properties. Deformed images were generated and seed positions were updated for each experimental setup using the VMR algorithm.

A dynamic dosimetry was performed for each case discretizing the edema resorption period in 30 intervals of 1 Day duration during the edema resorption period. Additionally, two static dosimetry simulations were performed for each case. In the first, the Day 1 (maximum edema volume) CT image and corresponding seed positions were used while in the latter, the Day 30 CT image and seed positions were used. The two static dosimetry simulations were considered as intraoperative and post-implant dosimetry, respectively. Dose metrics for the evaluation of the dosimetry were calculated for the dynamic, intraoperative, and post-implant dosimetry simulations.

The relative difference between dynamic and intraoperative dosimetry (*Day30 dynamic relative difference*) and the relative difference between post-implant and intraoperative dosimetry (*Day30 conventional relative difference*) are summarized below in Tables 4.1 and 4.2 for all the cases of the *Young modulus effect* and the *Excessive fluid pressure effect* experiments respectively.

The comparison of the intraoperative dosimetry simulation with both the dynamic and post-implant dosimetry simulations, for the various edema resorption cases considered, demonstrates the overall underestimation of the dose if the intraoperative dosimetry is performed without accounting for the edema resorption mechanism similarly to previous studies [Tejwani et al., 2012, Chira et al., 2013]. Furthermore, the dose difference is shown to increase proportionally with the edema magnitude and prostate stiffness increase. Higher edema magnitude leads to increased prostate volumetric changes, hence more extended seeds' movement that result in higher dose underestimation during the intraoperative dosimetry.

Moreover, the higher prostate stiffness cause more rapid volumetric changes and seed movements increasing, therefore, the edema-associated dosimetric difference between intraoperative and post-implant dosimetry. On the other hand, for prostate with lower stiffness (lower Young modulus) due to the linear edema resorption and the higher edema half-life, the negative effect of edema on the intra-operative dosimetry is lower.

Table 4.1 – Mean relative difference for the dose metrics of interest for the 15 patients dataset between Day1 and conventional/dynamic Day30 dosimetry for the different cases of the Young modulus effect experiment.

Young modulus effect case	Dose metric	Day30 dynamic relative difference (%)	Day30 conventional relative difference (%)
YM: 0.01	Prostate V_{90}	20.8 ± (5.5)	26.1 ± (6.4)
	Prostate D_{90}	10.2 ± (1.7)	10.4 ± (2.1)
	Urethra D_{10}	7.6 ± (1.4)	9.3 ± (1.6)
	Rectum D_{2cc}	6.2 ± (1.0)	6.3 ± (1.4)
	P. Arch D_{10}	−1.8 ± (0.3)	−2.2 ± (0.5)
YM: 0.05	Prostate V_{90}	44.8 ± (6.0)	50.5 ± (6.1)
	Prostate D_{90}	22.0 ± (1.9)	22.2 ± (2.6)
	Urethra D_{10}	19.2 ± (2.1)	21.8 ± (2.1)
	Rectum D_{2cc}	9.3 ± (2.5)	9.4 ± (3.1)
	P. Arch D_{10}	−4.4 ± (0.4)	−4.8 ± (0.6)
YM: 0.001	Prostate V_{90}	31.4 ± (3.5)	34.3 ± (4.7)
	Prostate D_{90}	19.2 ± (0.6)	19.0 ± (0.5)
	Urethra D_{10}	18.9 ± (6.2)	20.6 ± (6.1)
	Rectum D_{2cc}	4.2 ± (2.5)	4.3 ± (2.8)
	P. Arch D_{10}	−4.2 ± (0.3)	−4.2 ± (0.4)

Table 4.2 – Mean relative difference for the dose metrics of interest for the 15 patients dataset between Day1 and conventional/dynamic Day30 dosimetry for the different cases of the Excessive fluid pressure effect experiment.

Excessive fluid pressure case	Dose metric	Day30 dynamic relative difference (%)	Day30 conventional relative difference (%)
$\Delta : 0.10$	Prostate V_{90}	7.7 ± (3.7)	8.9 ± (4.6)
	Prostate D_{90}	6.2 ± (1.1)	5.9 ± (1.4)
	Urethra D_{10}	4.2 ± (1.5)	4.9 ± (1.5)
	Rectum D_{2cc}	−1.0 ± (0.7)	−0.6 ± (0.8)
	P. Arch D_{10}	−1.3 ± (0.3)	−1.2 ± (0.4)
$\Delta : 0.20$	Prostate V_{90}	19.0 ± (3.4)	21.9 ± (4.7)
	Prostate D_{90}	13.6 ± (1.5)	13.4 ± (4.1)
	Urethra D_{10}	10.5 ± (3.4)	12.2 ± (4.2)
	Rectum D_{2cc}	4.1 ± (1.5)	4.4 ± (3.8)
	P. Arch D_{10}	−2.7 ± (0.3)	−2.9 ± (0.8)
$\Delta : 0.38$	Prostate V_{90}	44.8 ± (6.0)	50.5 ± (6.1)
	Prostate D_{90}	22.0 ± (1.9)	22.2 ± (2.6)
	Urethra D_{10}	19.2 ± (2.1)	21.8 ± (2.1)
	Rectum D_{2cc}	9.3 ± (2.5)	9.4 ± (3.1)
	P. Arch D_{10}	−4.4 ± (0.4)	−4.8 ± (0.6)
$\Delta : 0.65$	Prostate V_{90}	80.1 ± (18.4)	96.7 ± (20.9)
	Prostate D_{90}	35.9 ± (5.0)	37.3 ± (6.6)
	Urethra D_{10}	31.2 ± (1.9)	36.3 ± (5.6)
	Rectum D_{2cc}	20.4 ± (2.9)	20.0 ± (4.1)
	P. Arch D_{10}	−6.2 ± (0.6)	−7.0 ± (1.1)

4.2.3 Dynamic dosimetry improvements

The introduced dynamic dosimetry scheme, as shown in Tables 4.1 and 4.2, is capable of incorporating edema associated volumetric changes and seed migration in intraoperative dosimetry. In this way, it is possible during the treatment planning to account for significant dose modifications that will eventually occur during the edema resorption period.

In the performed simulation experiments, relative dose differences in the prostate, between dynamic and conventional intraoperative dosimetry, were found in a range between 6.2% and 35.9% with the minimum value occurring in the case of the minimum edema magnitude (0.1) and the maximum value in the case of the maximum edema magnitude (0.6) respectively. Similarly, the relative dose difference was found more significant for increasing prostate stiffness, where for prostate with a Young modulus (YM) of 0.01 MPa (linear resorption) the dose difference was 10.2% while in the case of YM equal to 0.1 MPa (exponential resorption) was up to 19.6%.

The increased relative dose differences for high edema magnitude and high prostate YM can be correlated with the extent of volumetric changes, the associated seeds migration, and the time that the phenomenon endures. Indeed, when the treatment planning is performed on a significantly edematous prostate it is expected to observe increased prostate dose coverage after edema resorption. Then, the prostate volume is reduced and the associated movement of the seeds leads to a more compact implant than the one planned. The dose alteration is more significant when the prostate YM is higher due to the resulting shorter edema resorption period. In contrast, when the edema resorption period is long, the volumetric changes and the seeds' migration are slow and the effect in dosimetry is lower due to the radioactive decay of the seeds.

A side-effect of the seeds migration during the edema resorption is the increase of the dose delivered on the urethra and hence the increase of the toxicity of the procedure. In the presented experimental setup, significant relative dose differences were found when dynamic dosimetry was considered, ranging between 4.2% and 31.2% and demonstrating the hot-spots occurrence in the central area of the prostate (see Figure 4.8)

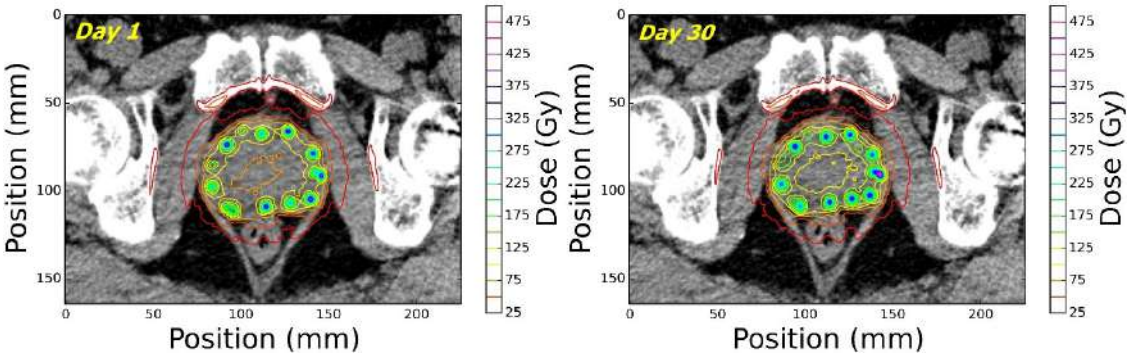

Figure 4.8 – Isodoses distribution in conventional and dynamic dosimetry. The dynamic dosimetry simulation is able to demonstrate significant dose increase in the central prostate region considering the displacements of the seeds after the edema resorption, while this information is not present in the conventional intraoperative dosimetry where edema is not considered.

The results of our experiments are in accordance with results from previously published

studies. Precisely, the prostate D_{90} increase of ≈11.7% for an edema magnitude of 10% ($\Delta = 0.1$) demonstrated by Chira et al. [2013] is within the D_{90} increase range for $\Delta = 0.1 - 0.2$ as it was estimated by the proposed dynamic dosimetry scheme. The prostate dose uncertainty of 2% of our Monte Carlo simulations and the low resolution image quality of the US modality used in the study of Chira et al. should be taken into account in the comparison of our results. Moreover, our dynamic dosimetry scheme demonstrated an increase of D_{90} of 22% for an average edema magnitude ($\Delta = 0.38$) similarly to the 20 Gy increase of D_{90}, demonstrated by the dynamic dosimetry scheme proposed by Leclerc et al. [2006].

In accordance to results demonstrated here and in Section 3.6, our proposed methodology enables to perform dynamic dosimetry calculation during the operation accounting for the edema resorption pattern of the patient, given the patient-specific mechanical parameters of the prostate and neighbor organs. The effect of the expected edema resorption pattern can be investigated in terms of isodoses distribution (see Figure 4.8) and dose-volume histogram (DVH) plots (see Figure 4.9) during the operation. This could improve the decision-making during the seeds' implantation procedure, leading to a lower chance of complications and improved outcome quality.

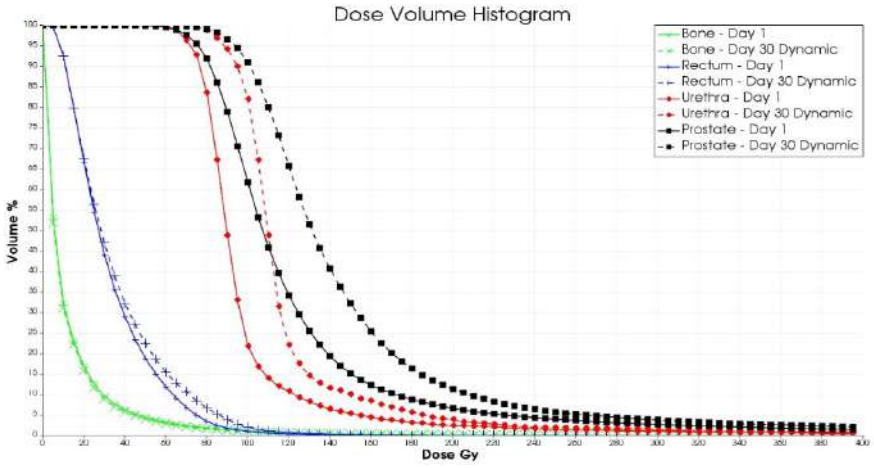

Figure 4.9 – DVH conventional and dynamic dosimetry. Dynamic dosimetry enables to improve the treatment planning procedure by estimating the impact of the edema resorption on the overall dose distribution in terms of dose-volume-histograms (DVH).

An interesting remark on the presented results can be done comparing the relative dose differences of the dynamic and post-implant dosimetry simulation with the intra-operative one. For all the edema magnitude and YM scenarios, an overall dose overestimation is demonstrated in post-implant dosimetry simulations when compared to the dynamic dosimetry scheme. This finding is attributed to the consideration of static volume and seeds' positions during the edema resorption period in the former case. Instead of considering the continuous displacements of the seeds from the implantation to the final positions and accounting for the gradual volumetric changes, in the post-implant simulation the CT image and the seeds' positions used are the ones acquired after the edema resorption.

The higher dose differences observed in our experiments between dynamic and conventional post-implant dosimetry were for the higher edema magnitude scenario ($\Delta = 0.65$) tested. The prostate D_{90} and the urethra D_{10} differences in this scenario were 1.4% and 5.1% respec-

tively with dose over-estimation in post-implant dosimetry simulation for both dose metrics. Nevertheless, the differences demonstrated in our experiment should be considered indicative rather than representative due to the small size of the employed patients' dataset. However, despite the demonstrated differences, correcting the intra-operative dosimetry based on the conventional post-implant scheme can improve significantly the quality of treatment planning with the minimum extra computational cost. This could enable the intraoperative adaptation of the treatment planning to edema-related seeds' migration.

4.3 Adaptive treatment planning

As shown in this Chapter, edema and the associated seeds' migration can have a significant effect in dosimetry. This effect is proportional to the magnitude of the edema. High edema magnitude leads to larger seeds' displacement from the planned positions, resulting in higher dosimetric differences.

By introducing the methodology that was developed in this chapter in the treatment planning procedure, the edema can be considered and the planned implantation sites can be modified in order to account for the calculated edema-related migration of the seeds. Therefore, here we present a strategy for adaptive treatment planning by combining the dynamic dosimetry methodology with the MC-ITPA that was presented in Chapter 2.

In the proposed strategy, right after the calculation of all the possible needle trajectories, the edema biomechanical model, presented in Chapter 3, is applied on the patient's medical image using the VMR algorithm (see Subsection 4.1.3). This allows to estimate the volumetric change of the prostate and the associated seeds migration on all the possible seed locations (see Figure 4.10).

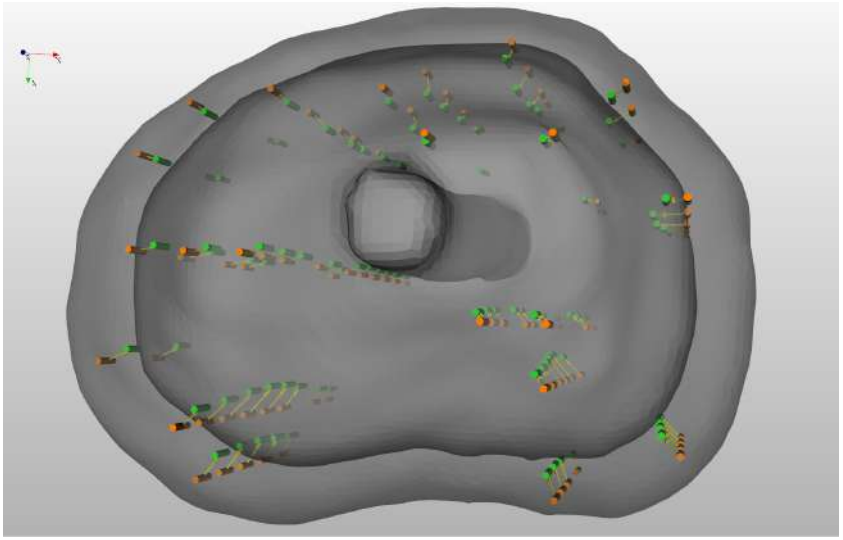

Figure 4.10 – Edema prediction in treatment planning. Applying the edema biomechanical model using the VMR algorithm on the patient's medical image during the treatment planning, volumetric changes and seeds' migration can be estimated.

With this information, the single-seeds dose maps are generated considering the post-operative geometry (reduced prostate volume after edema resorption) and the updated possible

seed positions, after applying the edema-related seed migration. In this way, MC-ITPA will produce the optimal implant with respect to the post-operative prostate volume and the seeds' migration.

The ability of MC-ITPA to adapt the treatment plan to edema resorption was evaluated for the scenario of maximum edema magnitude ($\Delta = 0.65$). The DVH-MC-ITPA was used due to its superior planning quality. A DVH-MC-ITPA optimized treatment plan was generated without considering the edema resorption (prostate volume = 70.8cc) and no seeds' migration (no-edema-correction plan). The resulting optimal implant's dosimetry was also evaluated using the post-operative prostate volume (42.9cc at Day30) to simulate the postoperative dosimetry (no-edema-correction post). Finally, a DVH-MC-ITPA optimized treatment plan was generated but this time after considering the edema resorption (prostate volume = 42.9cc) and the edema-related seeds' migration (edema-correction plan). The dose metrics for the prostate and OARs (urethra, rectum) for the three different scenarios (no-edema-correction plan, no-edema-correction post, edema-correction plan) are summarized in Table 4.3.

Table 4.3 – Adaptation of treatment planning to edema. The dosimetric results of a standard treatment plan without considering the edema (no-edema-correction plan), its post-operative dosimetry (no-edema-correction post), and a treatment plan with intra-operative consideration of edema (edema-correction plan) are demonstrated. The desired planning requirements are achieved by implants of less seeds using fewer needles when edema is accounted in the treatment planning.

Organ	Dose Metric	no-edema-correction plan	no-edema-correction post	edema-correction plan
Prostate	V_{100} (%)	95.5	99.9	96.1
	V_{150} (%)	47.4	86.6	45.8
	V_{200} (%)	19.3	40.6	19.8
	D_{90} (Gy)	159.5	209.5	160.4
Urethra	D_{10} (Gy)	187.3	241.2	197.9
	D_{30} (Gy)	177.1	228.4	176.1
Rectum	D_{2cc} (Gy)	119.5	153.5	111.5
	$D_{0.1cc}$ (Gy)	171.2	211.2	177.9
Seeds		91	91	55
Needles		25	25	16
Prostate Volume (cc)		70.8	42.9	42.9

As shown in Table 4.3, even if the no-edema-correction plan's implant respects all the `AAPM TG-137` planning criteria, it results in significant post-operative over-dosage of the OARs (28.8% higher urethra D_{10}, 28.5% higher D_{2cc}) and significant dose coverage heterogeneity in the prostate (82.7% increase of V_{150}) as shown in the no-edema-correction post. However, with the proposed strategy for adaptive treatment planning (edema-correction plan) these differences between intra-operative and post-operative dosimetry are alleviated. Furthermore, the resulting optimal implant is composed of fewer seeds delivered by fewer needles since the prostate volume considered during treatment planning is significantly lower after considering the edema resorption.

It should be noted that in cases of high edema magnitude, where edema-related seeds migration is higher, the dosimetric differences between dynamic and conventional post-operative dosimetry are more significant (see Table 4.2). In these cases, single-seed dose maps should be generated considering the prostate volume and the seeds migration at different time intervals during the first 30 days after the operation and be accumulated in the final cumulative single-seed dose maps (dynamic dosimetry) to be used during the DVH-MC-ITPA optimization.

As it is demonstrated, by integrating the VMR algorithm in the DVH-MC-ITPA we are able to provide treatment plans that conform to the planning requirements (even in extreme cases - $\Delta = 0.65$), taking into consideration the post-operative anatomic changes and edema-related seeds' migration. This experiment was considered a proof of concept and extended experimentation on patient-specific data is planned after completing the clinical trial, where MRI edema follow-up of 25 patients will be performed at CHRU Brest.

4.4 Dynamic Monte Carlo dosimetry summary

A methodology to account for the edema dynamics in intra-operative dosimetry has been presented. A volumetric model resampling algorithm, introduced by Aguilera et al. [2015], has been updated. The edema-induced deformation, as computed by the proposed biomechanical model (see Chapter 3), is mapped to the patient's CT image, the segmentation image, and the selected seeds' positions. MC dosimetry can then be performed considering the volume deformation of the organs of interest and the seed displacements. This dynamic MC dosimetry scheme has been shown adequate to compensate for observed dose differences, between intra-operative and post-operative dosimetry. Introducing the proposed methodology in the treatment planning, the outcome of the LDR brachytherapy procedure can be improved by considering dose differences between intra-operative and post-operative dosimetry during the planning. This capability was demonstrated for the extreme edema magnitude scenario of $\Delta = 0.65$. More extensive investigations based on real patient data are expected to be performed after creating a clinical database of edema follow-up MRI images from 25 patients in the CHRU of Brest.

Discussion

Despite the continuous advancements in cancer treatment the last decades, prostate cancer remains the second most common type of cancer amongst men. Throughout this manuscript, the focus was pointed on the LDR brachytherapy, between the various available treatment options for prostate cancer. This choice was supported by the wide clinical application of LDR brachytherapy nowadays. However, LDR brachytherapy treatment planning is based on rough approximations that result in significant side-effects. The aim of this thesis was to adress specific limitations (inverse planning quality, dosimetry approximations, edema) and propose methods and strategies to improve the current LDR brachytherapy procedure.

Inverse planning

In Chapter 2, a fast and efficient inverse treatment planning algorithm was presented, called MC-ITPA. Currently, the available inverse planning systems in clinical practice are based on FSA optimization. For a sufficiently high annealing temperature (T_{anneal}) and sufficiently slow cooling rate (CR), FSA provides implants of the desired quality. Recently, a new optimization method inspired by sparse signal reconstruction was proposed with the ability to achieve plans of sufficient quality in interactive time (0.03-0.23s) [Guthier et al., 2015]. However, the prostate V_{150} dose metric recommendations were not respected in these plans. Values ranging between 59% to 73% have been reported while the maximum limit is 50%, as given by the `AAPM TG137` recommendations. Higher values than 50% for the prostate V_{150} metric represent increased dose heterogeneity which is associated with under-treatment of the disease and increased possibility of recurrence.

Moreover, all these methods are based on the `AAPM TG43` dosimetric formalism where the patient is considered as an homogeneous infinite volume of water. Especially in LDR brachytherapy, where the photoelectric phenomenon is dominant, atomic number differences (tissue heterogeneity) affect notably the dosimetry. It is shown that the formalism of `TG43` overestimates the delivered dose with differences up to 7% in prostate D_{90} (3% due to tissue heterogeneity and 4% due to attenuation between seeds), compared to Monte Carlo (MC) simulations [Carrier et al., 2007].

The first improvement of the proposed MC-ITPA was the introduction of MC dosimetry in the optimization process, where MC single-seed dose maps were calculated for all the available seed positions, that could be occupied in an implant, during a pre-optimization step. This approach has been previously adopted in HDR brachytherapy [D'Amours et al., 2011], but not efficiently enough to be introduced in the intra-operative practice. The employment of GPU computation resources enabled us to render the MC simulation applicable in the operating room, where single-seed dose maps of $\approx 2\%$ statistical uncertainty in the prostate could be generated in $\approx 15-20$ for $\approx 400-600$ seeds using a `NVIDIA GTX Titan` GPU.

The second improvement of the MC-ITPA was the improvement of the FSA-based optimization, itself. In our development, an optimal implant was able to be delivered in $\approx 0.8-1$s for a setting of $T_{anneal} = 10^5$ and $CR = 0.2\%$. The quality of the planning results (implant dosimetry) was evaluated against the `TG137` planning recommendations. The resulting treatment plans had comparable quality to clinical treatment plans previously performed in CHRU Brest (following the `AAPM TG43` dose formalism) for the given dataset of 18 patients.

However, prostate dose homogeneity, as expressed by V_{150} and V_{200} was not always respected. The mean prostate V_{150} and V_{200} dose metrics were found 51.3 ± (3.0)% and 25.4 ± (4.0)% respectively, exceeding the `AAPM TG137` recommended limits (50% and 20%). This limitation is associated to the low number of dose optimization points in the interior of the prostate (located only between seeds). While a common solution would be to increase the number of the prostate internal dose points, another approach was preferred. Rather than using dose-based cost function, a DVH-based cost function was employed which enabled the direct control over all the desired dosimetric criteria. In this way, the optimization was performed in 15s, still ×4 times faster than state-of-the-art systems [D'Amours et al., 2011], but implants with improved prostate dose homogeneity could be generated (V_{150} = 46.0 ± (2.7)% and V_{200} = 19.6 ± (0.7)%). Furthermore, with this approach, the operator controls directly the treatment planning outcome by setting the desired DVH metrics. In this way, the inverse planning of the treatment is more natural and no learning curve is required.

In the simulations, computational phantoms considering 4 different materials for the 4 areas of interest (prostate, urethra, rectum, and surrounding tissues) were used, following the material composition recommendations of the ICRU report 46 and ICRP Publication 89, in order to account for tissue heterogeneity in dose calculations. The effect of the selected materials composition on dosimetry was evaluated with CT-derived phantoms. The dose calculation was found over-estimated when the computational phantoms were used instead of the CT-derived phantoms. However, it was found that a significant portion of the dosimetric difference between the two types of phantoms was associated with the statistical noise of CT images. After applying a Gaussian filter on the CT images, reported differences up to 8.1 ± (0.4)% in the prostate were reduced to 2.9 ± (0.7)%. In order to achieve the highest possible dosimetric accuracy during the operation, a CT image of the patient must be available. This image should be registered to the intra-operative US image and filtered accordingly to reduce the statistical noise. Otherwise, computational phantoms derived directly from the US image segmentation can be used with tolerable error.

Comparing Monte-Carlo dosimetry on the heterogeneous computational phantoms and on water-equivalent phantoms (`TG43` simulation), we found mean dosimetric differences in prostate D_{90} of 3.1% similarly to published studies [Carrier et al., 2007]. The validity of the simulated results was ensured by investigating the effect of the chosen MC statistical uncertainty (≈ 2%) on the DVH metrics which was found negligible. Therefore, in our methodology the `TG43` dose overestimation on prostate D_{90} is reduced by 3% on average. However, the use of the seed phasespace does not allow for reducing the dose overestimation related to particle interactions between seeds.

Introducing the DVH-MC-ITPA we were able to generate optimal treatment plans in less than 1 minute (15-20s for single-seed dose maps + 15s for DVH-based FSA optimization). Our next objective was to further improve the treatment planning procedure, trying to eliminate dosimetric uncertainties. An important factor that reduces the quality of the treatment plan is the operation-induced edema.

Edema biomechanical modeling

In Chapter 3, a biomechanical model to simulate the edema dynamics was proposed. Edema is formed fast during the operation and reaches its maximum magnitude shortly after its end. Moreover, it resorbs gradually and the resorption can last for several days. The magnitude

and the resorption time of edema can differ significantly amongst patients. Current models are based on macroscopic observations and are not able to account for this diversion. In our effort to develop a patient-specific model, we proposed a biomechanical model based on continuum mechanics principles. Using the Finite Element (FE) method, we simulated the edema dynamics by associating the phenomenon with the inflammation mechanism and the tissue mechanical properties.

A series of experiments revealed that between the Young modulus (stiffness) and the Poisson's ratio (compressibility), the former has a stronger effect on the edema. It was also shown that the prostate's stiffness affects the edema half-life, where edema demonstrated a linear resorption pattern for prostates with low stiffness. For increasing stiffness the edema resorption pattern gradient was increasing, until becoming exponential. This finding showed that prostate stiffness can be an indicator of the observed diversion in edema resorption which was shown in previous studies that can follow an exponential, or linear or even no specific pattern. Moreover, the edema magnitude was correlated with the increased excessive fluid accumulation in the interstitial matrix due to inflammation. Brachytherapy-induced edema mechanism has not been previously addressed.

Our study showed that a priori knowledge about the tissue mechanical properties and the underlying inflammation mechanism could provide a predictive insight to the evolution of the edema. Prostate's mechanical properties can be acquired by elastography measurements and inflammation can be accounted by modeling the responsible biological mechanism. This information can allow to adapt the treatment planning intra-operatively in order to reduce dosimetric uncertainties.

Dynamic Monte Carlo dosimetry

The adaptation of the treatment plan to volumetric and shape changes in the patient's anatomy due to edema was the objective of the developments of Chapter 4. In this chapter, a volumetric model resampling (VMR) algorithm was adapted to LDR brachytherapy. In the VMR method, the computed deformation field on the tetrahedral representation of the biomechanical model, was mapped to the medical image (voxelized volume) of the patient using barycentric interpolation. In this way, volumetric and shape changes due to edema in different time intervals were mapped to pre-operative CT images of 15 patients in order to investigate the effect of edema in dosimetry. In addition, the computed deformation field was applied to the initially selected seeds considering a linear relationship. In this way seeds migration due to edema dynamics was considered.

Considering anatomical changes and seeds migration, a dynamic Monte Carlo simulation scheme was proposed. The dynamic MC dosimetry revealed the dosimetric differences that arise between intra-operative and post-operative dosimetry. A proportional relationship between edema magnitude and intra-/post-operative dosimetric differences was shown. Even under the assumption of linear seed migration, dosimetric differences found in this study agree with findings of previous studies available in the literature. Introducing the developed methodology in the treatment planning procedure of the MC-ITPA, intra-operative and post-operative dosimetry differences were eliminated during treatment planning for the extreme value of the considered edema magnitude ($\Delta = 0.65$).

In order to transfer the developments described in this thesis in the clinical practice a treatment planning system named ORACLE was developed and is briefly described in the

Appendix A. ORACLE stands for `Optimized Brachytherapy planning system` and provides a user-friendly graphical interface for the use of the developments described in Chapters 2 and 4. A finite element solver was not incorporated in ORACLE. The biomechanical model of edema can be solved with any available FE solver (e.g `FeBio`) and be provided as input to ORACLE, in the current state of the program. This last development decision was motivated by the fact that edema dynamics are not yet fully explored and more research should be focused on this task. In addition, FE method demands the generation of a 3D mesh which can be an arduous task even for experienced engineers and is not attractive for intra-operative applications. On the other hand, these last modeling limitations create the perspective for future improvements of the proposed methods.

Table D.1 – Thesis contributions in LDR treatment planning summary.

Objective	Clinical method	Cons	Proposed method	Pros	Cons	Perspective
Inverse planning	- FSA - TG43	- Indirect planning (1min) - Overestes dose (few ms)	- DVH-based FSA - GPU MC	- Direct planning (15s) - Accurate Dose ($\approx 15-20$s)	- -No seeds interactions	- GPU acceleration - Correction Factor
Edema correction	- Analytical models	- No patient specific	- Biomechanical FE model	- Patient anatomy - Predictive	- Mesh distortion - Elasticity	- Meshless methods - Elastography
Adaptive planning	- None	- Static dosimetry	- 3D volume resampling ($\approx$ 2s)	- Dynamic dosimetry	- Linear seed migration	- Rigid body modeling

Perspective

Currently, our focus is on meshless methods that can be used as an alternative to the FE method for the biomechanical modeling of edema. The principal advantage of these methods is that the mesh requirement of FE method is eliminated and hence meshless methods could be introduced in intra-operative environment. In addition, the native parallelism of these methods renders them compatible with the time constraints of brachytherapy treatment.

The freedom offered by meshless methods in the construction of models with an arbitrary level of detail can enable the efficient modeling of more complicated mechanisms and could be essential for the improvement of the proposed edema model and the understanding of the edema mechanism. This edema mechanism is strongly related on patient-specific mechanical properties and insight that can be provided by elastography could be essential for the adaptation of the model to patient-specific biomechanics other than anatomy. Moreover, fine structures can be considered with less computational overhead and seeds migration could be introduced in the edema model, based on rigid body motions. Then, interactions between seeds could also be considered by introducing a hybrid navigation algorithm in the dosimetric calculation. Moreover, the implementation of FSA on GPU could accelerate the inverse planning procedure.

Conclusion

Concluding, the treatment planning optimization of LDR brachytherapy was addressed in several ways. Intra-operative dosimetry was improved introducing GPU-accelerated MC dosimetry. This in combination with the DVH-based optimization enabled the fast and efficient adaptive inverse treatment planning. The biomechanics of edema were explored and observed

diversity amongst patients was correlated with inflammation and tissue mechanical properties. Taking into consideration the edema biomechanics, we were able to provide a dynamic MC simulation scheme that can be used for the adaptation of the treatment planning in various edema conditions. This work created the perspective for future investigation of the edema mechanism focusing on meshless methods that will allow to develop more sophisticated biomechanical models that could be easily incorporated in the operational room. The contributions of this thesis to LDR treatment planning are summarized in the Table D.1.

Dissemination

Peer-reviewed Journals

Mountris, K.A., Bert, J., Noailly, J., Aguilera, A.R., Valeri, A., Pradier, O., Schick, U., Promayon, E., Ballester, M.G., Troccaz, J. and Visvikis, D., 2017. Modeling the impact of prostate edema on LDR brachytherapy: a Monte Carlo dosimetry study based on a 3D biphasic finite element biomechanical model. Physics in Medicine and Biology, 62(6), p.2087.

Invited Presentations

Oral presentation: "ORACLE: A DVH-based inverse planning system for LDR prostate brachytherapy using MC dosimetry". **Mountris, K.A.**, Bert, J., Boussion, N., Valeri, A., Schik, U. and Visvikis, D. International Conference on Monte Carlo Techniques for Medical Applications 2017, Naples Italy October 2017. (accepted)

Oral presentation: "Prostate Brachytherapy Optimization Using GPU Accelerated Simulated Annealing and Monte Carlo Dose Simulation". **Mountris, K.A.**, Bert, J. and Visvikis, D. 2016 IEEE Nuclear Science Symposium and Medical Imaging Conference, Strasbourg France November 2016.

Poster presentation: "Biomechanical Modeling of prostate brachytherapy-induced edema". **Mountris, K.A.**, Bert, J., Promayon, E., Troccaz, J. and Visvikis, D. 2016 French National Conference CAMI LabEx Days, Rennes France December 2016.

Funding

This work was partly supported by the French Brittany Region and by the French ANR within the Investissements d'Avenir program (Labex CAMI) under reference ANR-11-LABX-0004 (Integrated project CAPRI) and through the FOCUS project (ANR-16-CE19-0011).

This work is part of a project that has received funding from the European Union's Horizon 2020 research and innovation programme under the Marie Skłodowska-Curie grant agreement No 691203.

This page is intentionally left blank

APPENDIX

A

ORACLE

ORACLE (Optimized Brachytherapy planning system) is an easy-to-use treatment planning software for LDR brachytherapy. Currently it is in experimental state and its purpose is to transfer the developments presented in this manuscript in the clinical practice.

The software is written completely in C++ and depends on few well documented and stable C++ libraries to provide a friendly graphical user interface equipped with the appropriate visualization tools that can facilitate the operator to deliver improved LDR brachytherapy treatment plans.

ORACLE dependencies

- `QT`: Graphical user interface
- `VTK`: Visualization tasks
- `Boost`: Filesystem management
- `GGEMS`: GPU-accelerated dosimetry

The two versions of the MC-ITPA algorithm, presented in Chapter 2, are both available in ORACLE.

ORACLE planning pipeline

The generation of a treatment plan can be performed in a number of simple steps. In this experimental version of the software, once the patient's data are loaded, the operator must set the position of the template guide by selecting the location of the first hole of the grid (1A). After setting the template guide, the available needle trajectories and seeds positions can be calculated by ORACLE. The pipeline of the generation of a treatment plan consists of the following steps

- Load patient data [image format (.mhd), model format (.feb/.txt)]
- Set the position of the template grid
- Set the number of simulated particles for the single-seed dose maps generation
- Generate single-seed dose maps
- Perform standard or DVH-based optimization
- Evaluate resulting plan's quality (DVH, isodoses)

The individual steps of the planning pipeline are described in the following in more detail.

Load patient data

In the beginning of the planning schedule few patient data are required as input (see Figure A.1). The ultrasound image of the patient should be given together with the segmentation image and an image containing the contours of the organs. All three images should be in .mhd format (*metaimage*). The segmentation image is used to render a 3D model of the prostate, the urethra, and the rectum; calculate the available needle trajectories for the plan; extract organs' volumes for seeds' number calculation, DVH calculation. The contour image is necessary only for the construction of *dectors* during the standard version of the optimization. In order to consider the edema formation during dosimetry and optimization, the biomechanical model must be loaded. The initial state of the model is extracted by the model's file given in .feb format (`FeBio`). The final state of the model's mesh should be provided in a .txt file where the displaced positions of the mesh's vertices are given as coordinate triplets (X, Y, Z). Information about the patient (name, gender, age, height, weight) can be given in the data loading dialog too.

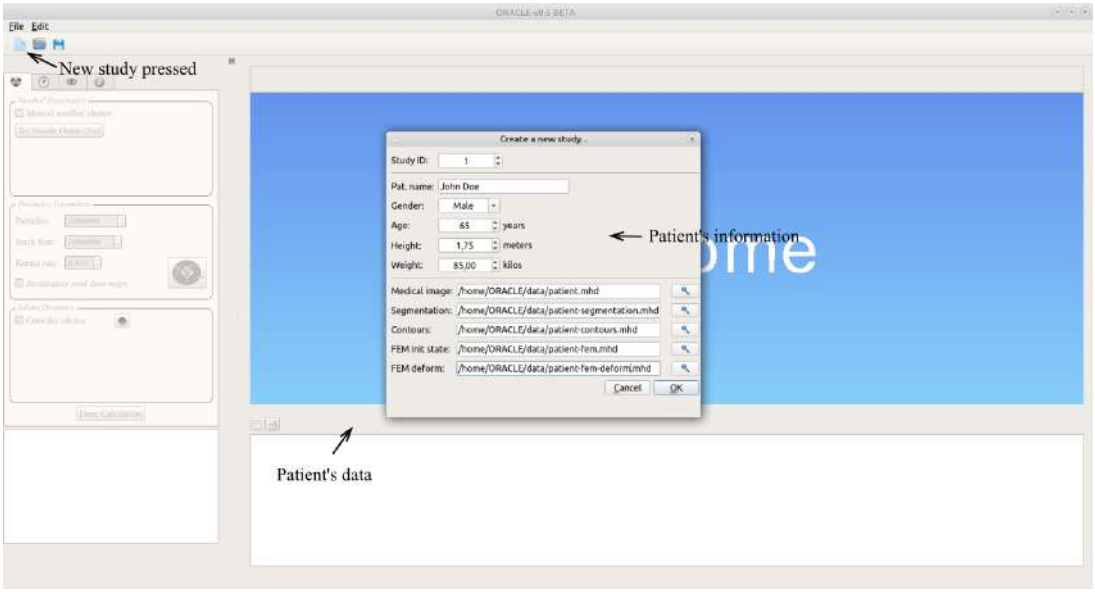

Figure A.1 – ORACLE data loading. Image and model datasets are loaded in the initial step of treatment planning with ORACLE by pressing the New Study icon.

Set the position of the template guide

The position of the template guide is set by providing the X, Y coordinates of the left corner hole (1A) of the grid (see Figure A.2). The template guide's grid holes are visualized as yellow dots superimposed on the ultrasound image visualization. To set the template guide, the button *Set Needle Guide Grid* which is located in the *Dosimetry* tab must be pressed.

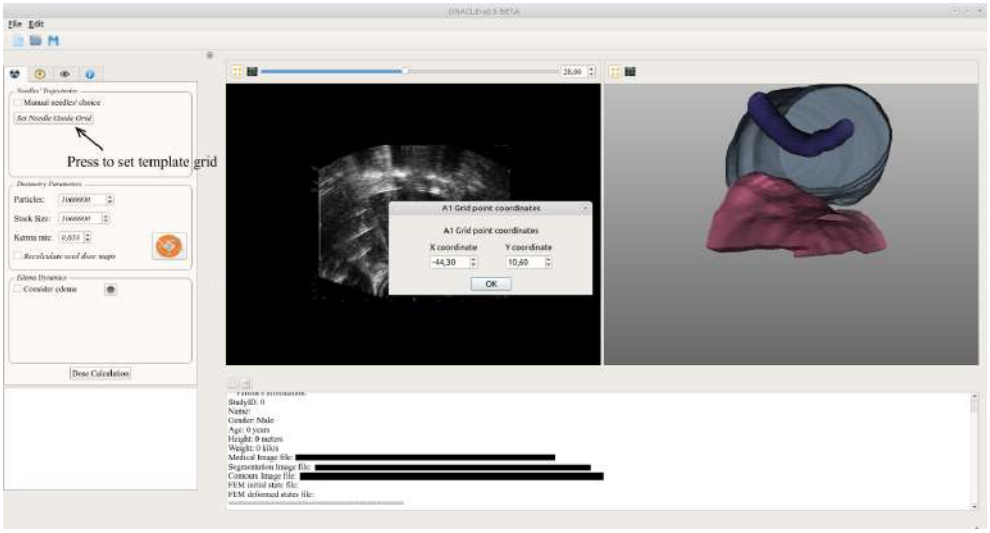

Figure A.2 – ORACLE template guide setting. The template guide must be set prior to dosimetry calculation in order to calculate the possible needle trajectories and the corresponding available seeds' positions.

Set the number of simulated particles for the single-seed dose maps generation

The number of particles for the generation of the single-seed dose maps is calculated automatically by ORACLE in order to provide a statistical uncertainty of $\approx 2\%$ in the final accumulated dose map. The calculation of the number of seeds and the number of simulated particles for the MC simulations is done by pressing the corresponding button (see Figure A.3).

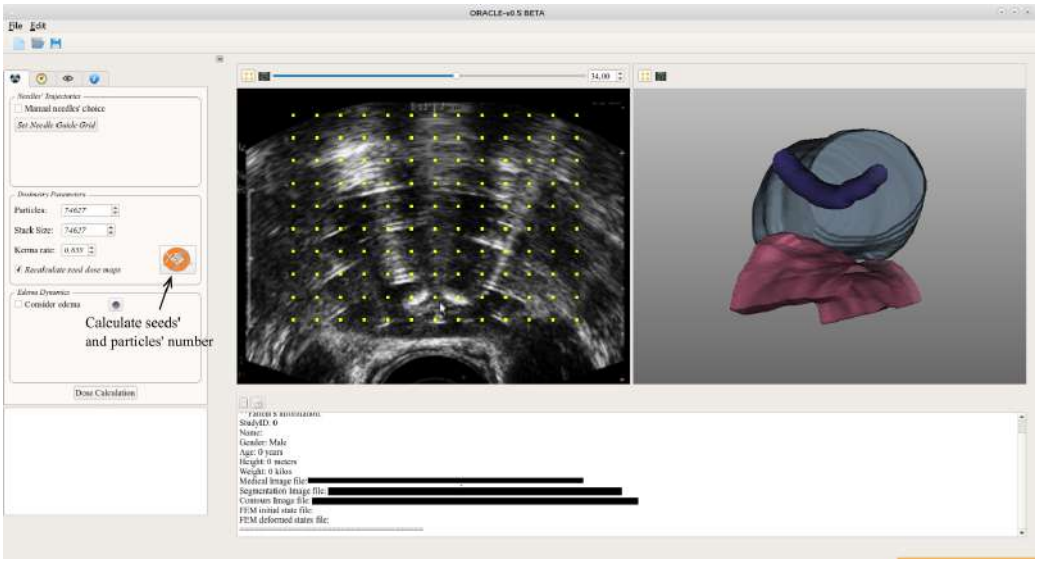

Figure A.3 – ORACLE seeds' and particles' number calculation. The number of the seeds' to be delivered in the plan is calculated according to the volume of the prostate and the activity of the seeds. The number of the simulated particles is then adjusted accordingly to achieve dose maps with the required statistical uncertainty

Generate single-seed dose maps

Single-seed dose maps are generated by pressing the *Dose Calculation* button once the number of seeds to be delivered and the number of simulated particles are calculated (see Figure A.4). In the end of the single-seed dose maps generation, *dectors* and *compressed dose maps* are extracted from the generated dose maps.

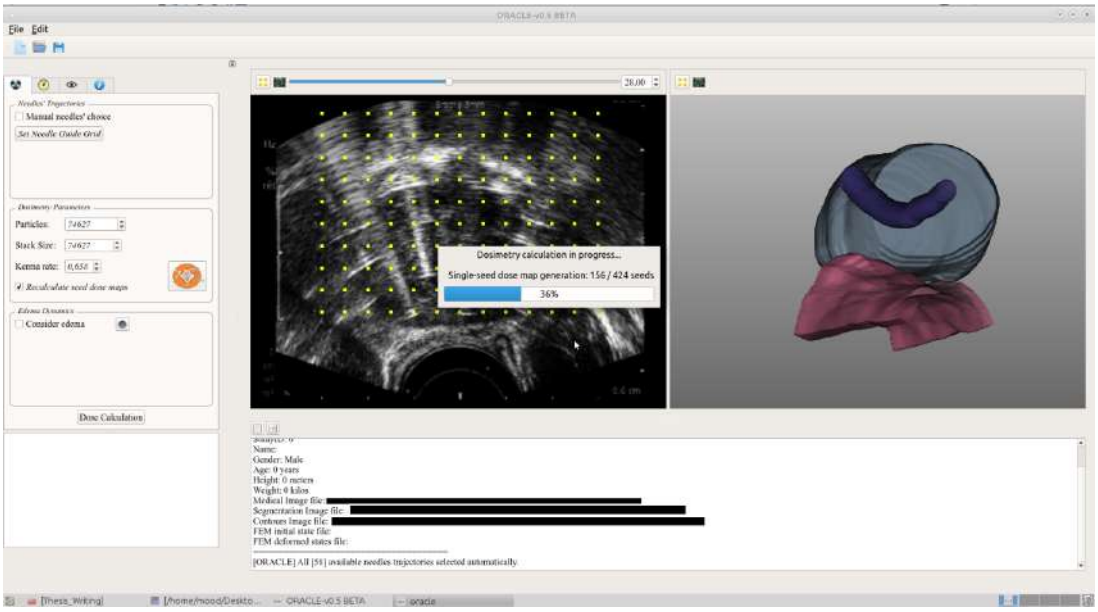

Figure A.4 – ORACLE single-seed dose maps generation. Single-seed dose maps are generated for all the available positions that a seed could occupy. Following, *dectors* and *compressed dose maps* are extracted from the generated dose maps.

Perform standard or DVH-based optimization

After the dosimetry calculations, the optimization can be performed either using the standard version (MC-ITPA) or the DVH-based version (DVH-MC-ITPA). Both are available in the *Optimization tab* and the corresponding planning criteria can be given for each organ otherwise the default values are used (see Figure A.5).

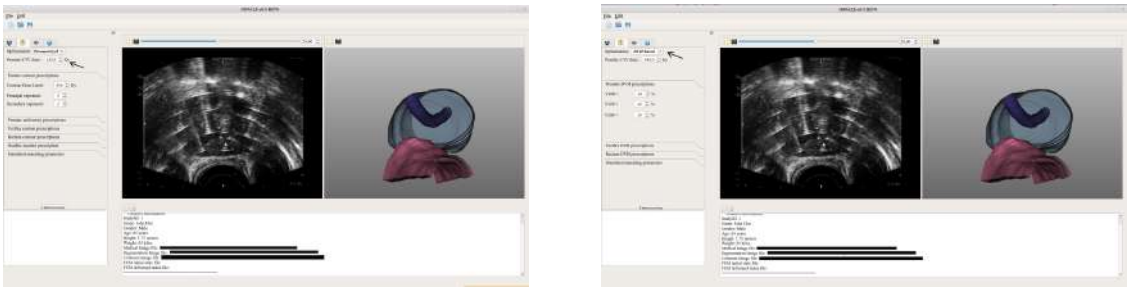

(a) Parametrized MC-ITPA (b) DVH-Based MC-ITPA

Figure A.5 – ORACLE Optimization. The operator can choose between the two versions of optimization to perform the inverse planning.

Evaluate resulting plan's quality (DVH, isodoses)

Finally, after the optimization of the treatment plan, the operator can evaluate qualitatively and quantitatively the generated plan. To do so a table with the different DVH dose metrics for the prostate, the urethra, and the rectum is given. Moreover, the DVH plot and the isodoses, both in 3D and in image-view, are available for visualization such as the selected seed positions (see Figure A.6).

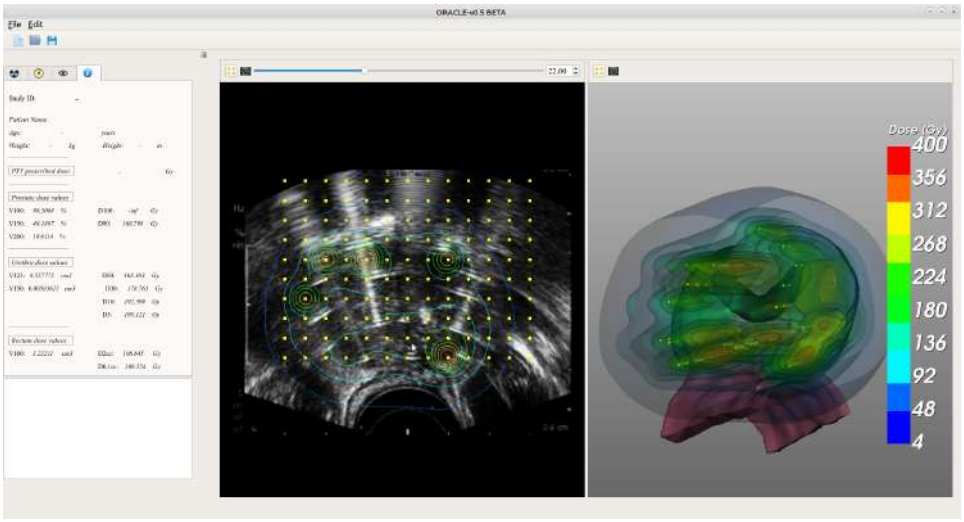

(a) Isodoses visualization

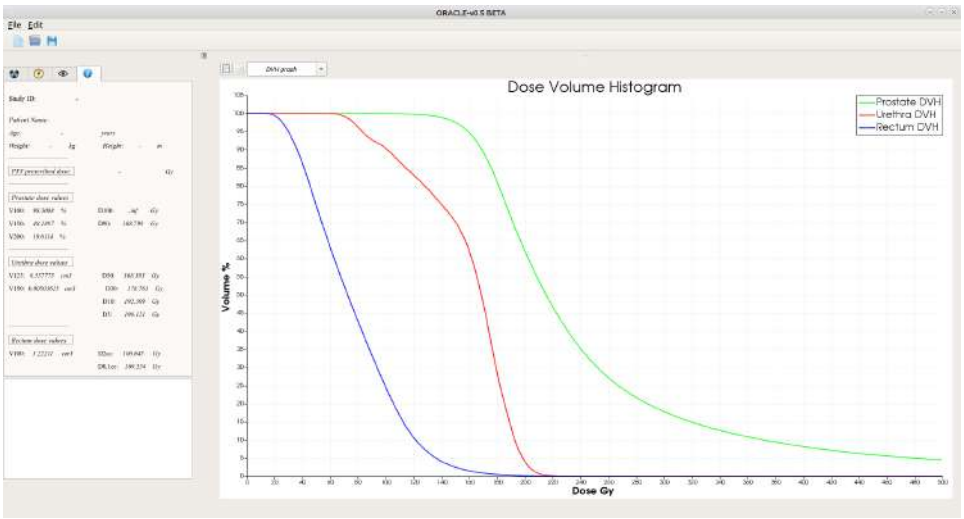

(b) DVH graph visualization

Figure A.6 – ORACLE Results evaluation. The generated plan can be evaluated by the various DVH metric available for the prostate OARS, their DVH graph and the isodoses distribution for the selected seeds' configuration.

APPENDIX

B

FSA OPTIMIZATION PSEUDO-CODE

Data: Initial temperature (T_0), cooling rate (CR), Dectors, dose prescriptions, possible seeds
Result: Optimized seeds' configuration
set initial random seeds configuration (initial_config);
extract dose values from dectors and construct accumulated dose vectors;
convert accumulated dose vectors to objective functions;
calculate cost function value E;
set current configuration: $current\_config = initial\_config$;
set current temperature: $T = T_0$;
$accepted\_update = false$;
while $T > 0$ **do**
    generate new_config by swapping two random seeds;
    update accumulated dose vectors;
    convert updated accumulated dose vectors to objective functions;
    calculate new cost function value E';
    if $E' < E$ **then**
        $accepted\_update = true$;
        $E = E'$;
        $current\_config = new\_config$;
    else
        calculate $P(\Delta E)$;
        select randomly from uniform distribution $P_{accept} \in [0, 1]$;
        if $P_{accept} > P(\Delta E)$ **then**
            $accepted\_update = true$;
            $E = E'$;
            $current\_config = new\_config$;
        end
    end
    $T* = (1 - CR)$;
end

Algorithm 1: MC-ITPA implementation of FSA algorithm

APPENDIX

C

INDIVIDUAL PATIENTS' DOSIMETRY REPORT

Table C.1 – Dose metrics for the individual plans generated by the standard MC-ITPA for the given patients dataset.

	Prostate				Urethra		Rectum			
Patient	$V_{100}(\%)$	$V_{150}(\%)$	$V_{200}(\%)$	$D_{90}(Gy)$	$D_{10}(Gy)$	$D_{30}(Gy)$	$D_{2cc}(Gy)$	$D_{0.1cc}(Gy)$	Seeds	Needles
P1	95.6	49.7	21.0	160.4	207.8	186.4	118.0	187.4	67	17
P2	95.4	49.9	20.2	159.6	191.8	171.0	109.8	172.8	71	17
P3	94.3	50.0	24.3	156.2	201.2	180.5	129.0	191.6	70	19
P4	94.1	52.4	22.9	158.4	192.4	173.8	107.6	165.7	62	18
P5	95.8	50.3	22.0	159.4	200.4	180.7	121.2	178.0	66	18
P6	95.9	50.7	26.5	158.9	165.4	156.1	96.5	134.7	63	19
P7	96.6	49.7	22.9	160.0	157.5	149.4	111.5	180.4	55	16
P8	97.0	60.2	32.8	168.7	170.3	150.8	107.8	147.4	63	16
P9	96.3	58.0	31.1	164.0	167.6	153.8	132.6	193.7	67	17
P10	95.2	54.9	26.0	160.0	166.2	155.2	101.1	152.8	72	18
P11	97.3	54.6	33.6	174.0	194.2	183.1	113.4	151.1	64	13
P12	96.7	53.2	30.3	163.0	164.3	155.7	119.1	173.0	65	15
P13	95.5	48.4	20.6	160.3	173.9	164.2	118.8	157.3	74	20
P14	96.0	48.1	24.1	156.3	157.3	147.7	102.3	137.3	63	21
P15	95.3	45.6	30.4	162.5	172.6	162.0	107.5	160.6	55	13
P16	95.3	49.8	25.6	159.2	170.6	159.5	118.5	176.3	60	17
P17	95.2	55.1	29.2	159.8	166.4	156.2	109.7	170.1	62	16
P18	95.1	49.0	27.5	156.9	161.5	152.1	113.3	154.1	62	15

In overall the dose homogeneity criteria is difficult to be respected. By fine tuning the optimization parameters (dose prescriptions, etc.), better homogeneity can be achieved in more loose-patterned plans (using more needles for plan delivery).

Table C.2 – Dose metrics for individual patient treatment plans, generated with the DVH-MC-ITPA.

	Prostate				Urethra		Rectum			
Patient	$V_{100}(\%)$	$V_{150}(\%)$	$V_{200}(\%)$	$D_{90}(Gy)$	$D_{10}(Gy)$	$D_{30}(Gy)$	$D_{2cc}(Gy)$	$D_{0.1cc}(Gy)$	Seeds	Needles
P1	95.2	40.2	19.4	154.9	156.6	148.4	104.3	179.0	67	18
P2	96.9	44.6	17.9	159.7	157.6	149.1	109.7	172.7	71	21
P3	95.0	41.2	19.7	156.9	168.9	158.8	110.8	190.1	70	19
P4	96.8	46.3	19.7	163.2	168.4	159.0	102.9	141.9	62	17
P5	97.1	42.4	19.6	162.7	167.8	158.7	116.4	197.8	66	20
P6	95.1	43.6	19.6	157.0	169.6	159.0	93.7	130.8	63	20
P7	98.1	48.0	19.7	168.8	191.0	175.8	108.1	154.7	55	16
P8	97.6	49.3	19.7	165.5	172.0	159.4	106.0	164.5	63	16
P9	96.0	46.2	19.8	161.3	170.5	159.2	127.1	195.1	67	19
P10	98.2	48.2	19.2	166.6	194.8	173.7	109.3	166.3	72	19
P11	95.4	47.7	20.2	161.0	185.4	174.2	101.3	143.3	64	14
P12	96.7	47.5	19.7	165.6	189.5	173.5	117.9	197.1	65	17
P13	95.7	47.7	19.8	160.0	185.3	172.3	114.6	184.4	74	19
P14	97.4	46.6	19.9	165.7	189.8	175.9	105.5	148.7	63	19
P15	96.6	47.1	19.8	165.1	187.4	170.1	98.5	147.35	55	15
P16	96.8	48.1	19.8	164.0	189.5	176.9	110.0	148.9	60	17
P17	97.6	48.0	19.9	164.8	193.1	172.1	116.3	175.6	62	16
P18	97.9	47.6	19.5	166.2	182.5	170.7	108.5	153.7	62	17

In all the cases all the planning criteria are efficiently achieved proving the treatment planning capabilities of the DVH-MC-ITPA.

BIBLIOGRAPHY

Agostinelli, Sea et al. (2003). "GEANT4—a simulation toolkit". *Nuclear instruments and methods in physics research section A: Accelerators, Spectrometers, Detectors and Associated Equipment* 506.3, pp. 250–303 (cit. on p. 33).

Aguilera, Alejandro Rodríguez et al. (2015). "A parallel resampling method for interactive deformation of volumetric models". *Computers & Graphics* 53, pp. 147–155 (cit. on pp. 94, 98, 111).

Ahmed, Afsar U. (2011). "An overview of inflammation: mechanism and consequences". *Frontiers in Biology* 6.4, p. 274 (cit. on p. 67).

Ahn, Bum-Mo et al. (2010). "Mechanical property characterization of prostate cancer using a minimally motorized indenter in an ex vivo indentation experiment". *Urology* 76.4, pp. 1007–1011 (cit. on p. 85).

Alcouffe, Ray E. et al. (1995). "DANTSYS: a diffusion accelerated neutral particle transport code system". *Los Alamos National Laboratory Manual LA-12969-M* (cit. on p. 20).

Andriole, Gerald L. et al. (2009). "Mortality results from a randomized prostate-cancer screening trial". *New England Journal of Medicine* 360.13, pp. 1310–1319 (cit. on p. 11).

Ateshian, Gerard A. (2017). "Mixture Theory for Modeling Biological Tissues: Illustrations from Articular Cartilage". *Biomechanics: Trends in Modeling and Simulation*. Springer, pp. 1–51 (cit. on p. 73).

Badiozamani, Kas Ray et al. (1999a). "Anticipating prostatic volume changes due to prostate brachytherapy". *Radiation oncology investigations* 7.6, pp. 360–364 (cit. on p. 21).

— (1999b). "Anticipating prostatic volume changes due to prostate brachytherapy". *Radiation oncology investigations* 7.6, pp. 360–364 (cit. on p. 66).

Barr, Richard G., Richard Memo, and Carl R. Schaub (2012). "Shear wave ultrasound elastography of the prostate: initial results". *Ultrasound quarterly* 28.1, pp. 13–20 (cit. on pp. 84, 85, 90).

Bathe, Klaus-Jürgen (2006). *Finite element procedures*. Klaus-Jurgen Bathe (cit. on p. 78).

Beaulieu, Luc et al. (2012). "Report of the Task Group 186 on model-based dose calculation methods in brachytherapy beyond the TG-43 formalism: current status and recommenda-

tions for clinical implementation". *Medical physics* 39.10, pp. 6208–6236 (cit. on pp. 20, 38, 58).

Bert, Julien (2016). "GGEMS: GPU GEant4-based Monte Carlo Simulation platform". *IEEE NSS-MIC 2016* (cit. on p. 33).

Bert, Julien et al. (2013). "Geant4-based Monte Carlo simulations on GPU for medical applications". *Physics in medicine and biology* 58.16, p. 5593 (cit. on pp. 31, 33).

Bethesda, MD (1992). "Proton and neutron interaction data for body tissues". *ICRU report* 46, p. 13 (cit. on pp. 21, 38, 39).

Briganti, Alberto et al. (2006). "Validation of a nomogram predicting the probability of lymph node invasion based on the extent of pelvic lymphadenectomy in patients with clinically localized prostate cancer". *BJU international* 98.4, pp. 788–793 (cit. on p. 13).

Brooks, Rodney A. (1977). "A quantitative theory of the Hounsfield unit and its application to dual energy scanning." *Journal of computer assisted tomography* 1.4, pp. 487–493 (cit. on p. 41).

Butler, Wayne M. et al. (2000). "Isotope choice and the effect of edema on prostate brachytherapy dosimetry". *Medical physics* 27.5, pp. 1067–1075 (cit. on p. 21).

Carlsson, AAsa K. and Anders Ahnesjo (2000). "The collapsed cone superposition algorithm applied to scatter dose calculations in brachytherapy". *Medical physics* 27.10, pp. 2320–2332 (cit. on p. 20).

Carrier, Jean-Francois et al. (2006). "Impact of interseed attenuation and tissue composition for permanent prostate implants". *Medical physics* 33.3, pp. 595–604 (cit. on p. 20).

Carrier, Jean-François et al. (2007). "Postimplant dosimetry using a Monte Carlo dose calculation engine: a new clinical standard". *International Journal of Radiation Oncology* Biology* Physics* 68.4, pp. 1190–1198 (cit. on pp. 20, 112, 113).

Challapalli, A. et al. (2014). "High dose rate prostate brachytherapy: an overview of the rationale, experience and emerging applications in the treatment of prostate cancer". *The British journal of radiology* (cit. on p. 17).

Chen, Yan, Arthur L. Boyer, and Lei Xing (2000). "A dose-volume histogram based optimization algorithm for ultrasound guided prostate implants". *Medical physics* 27.10, pp. 2286–2292 (cit. on p. 60).

Chen, Yan et al. (1997). "Treatment planning for prostate implant with loose seeds". *Medical physics* 24.7, pp. 1141–1145 (cit. on p. 23).

Chibani, Omar, Jeffrey F. Williamson, and Dorin Todor (2005). "Dosimetric effects of seed anisotropy and interseed attenuation for Pd103 and I125 prostate implants". *Medical physics* 32.8, pp. 2557–2566 (cit. on p. 20).

Chira, Ciprian et al. (2013). "Prostate volume changes during permanent seed brachytherapy: an analysis of intra-operative variations, predictive factors and clinical implication". *Radiation Oncology* 8.1, p. 177 (cit. on pp. 66, 90, 104, 108).

Chou, Roger et al. (2011). "Screening for prostate cancer: a review of the evidence for the US Preventive Services Task Force". *Annals of internal medicine* 155.11, pp. 762–771 (cit. on p. 11).

Cohen-Steiner, David, Eric Colin De Verdiere, and Mariette Yvinec (2002). "Conforming Delaunay triangulations in 3D". *Proceedings of the eighteenth annual symposium on Computational geometry*. ACM, pp. 199–208 (cit. on p. 81).

Dai Kubicky, Charlotte et al. (2008). "Inverse planning simulated annealing for magnetic resonance imaging-based intracavitary high-dose-rate brachytherapy for cervical cancer". *Brachytherapy* 7.3, pp. 242–247 (cit. on p. 30).

Dayan, Colin M. and Gilbert H. Daniels (1996). "Chronic autoimmune thyroiditis". *New England journal of medicine* 335.2, pp. 99–107 (cit. on p. 70).

Deb, Kalyanmoy (2001). *Multi-objective optimization using evolutionary algorithms*. Vol. 16. John Wiley & Sons (cit. on p. 24).

DeMarco, J. J., T. D. Solberg, and J. Bl Smathers (1998). "A CT-based Monte Carlo simulation tool for dosimetry planning and analysis". *Medical physics* 25.1, pp. 1–11 (cit. on p. 32).

Donoho, David L. (2006). "Compressed sensing". *IEEE Transactions on information theory* 52.4, pp. 1289–1306 (cit. on p. 31).

D'Amours, Michel et al. (2011). "Patient-specific Monte Carlo-based dose-kernel approach for inverse planning in afterloading brachytherapy". *International Journal of Radiation Oncology* Biology* Physics* 81.5, pp. 1582–1589 (cit. on pp. 31, 37, 59, 112, 113).

Epstein, Jonathan I. et al. (2016). "The 2014 International Society of Urological Pathology (ISUP) Consensus Conference on Gleason Grading of Prostatic Carcinoma: definition of grading patterns and proposal for a new grading system". *The American journal of surgical pathology* 40.2, pp. 244–252 (cit. on p. 10).

Fabri, Andreas and Sylvain Pion (2009). "CGAL: The computational geometry algorithms library". *Proceedings of the 17th ACM SIGSPATIAL international conference on advances in geographic information systems*. ACM, pp. 538–539 (cit. on p. 81).

Fang, Q. and D. A. Boas (2010). *iso2mesh: a 3D surface and volumetric mesh generator for MATLAB/Octave* (cit. on p. 82).

Flampouri, Stella et al. (2006). "Estimation of the delivered patient dose in lung IMRT treatment based on deformable registration of 4D-CT data and Monte Carlo simulations". *Physics in medicine and biology* 51.11, p. 2763 (cit. on p. 32).

Fu, Yibin B. and Raymond W. Ogden (2001). *Nonlinear elasticity: theory and applications*. Vol. 283. Cambridge University Press (cit. on p. 84).

Gerbaulet, Alain (2002). "The GEC ESTRO handbook of brachytherapy" (cit. on p. 15).

Gibbons, Robert P. (1987). "Prostate cancer. Chemotherapy". *Cancer* 60 (S3), pp. 586–588 (cit. on p. 13).

Gonzalez, Oscar and Andrew M. Stuart (2008). *A first course in continuum mechanics*. Cambridge University Press (cit. on p. 73).

Gorissen, Bram L., Dick Den Hertog, and Aswin L. Hoffmann (2013). "Mixed integer programming improves comprehensibility and plan quality in inverse optimization of prostate HDR brachytherapy". *Physics in medicine and biology* 58.4, p. 1041 (cit. on p. 60).

Grosland, Nicole M. et al. (2009). "IA-FEMesh: An open-source, interactive, multiblock approach to anatomic finite element model development". *Computer methods and programs in biomedicine* 94.1, pp. 96–107 (cit. on p. 81).

Guthier, C. et al. (2015). "A new optimization method using a compressed sensing inspired solver for real-time LDR-brachytherapy treatment planning". *Physics in medicine and biology* 60.6, p. 2179 (cit. on pp. 24, 30, 31, 112).

Hammerich, Kai H., Gustavo E. Ayala, and Thomas M. Wheeler (2009). "Anatomy of the prostate gland and surgical pathology of prostate cancer". *Cambridge University, Cambridge*, pp. 1–10 (cit. on p. 9).

Haridas, Balakrishna et al. (2006). "PelvicSim—A computational-experimental system for biomechanical evaluation of female pelvic floor organ disorders and associated minimally invasive interventions". *Stud. Health Technol. Inf* 119, pp. 182–187 (cit. on p. 84).

Heidenreich, Axel et al. (2011). "Percentage of positive biopsies predicts lymph node involvement in men with low-risk prostate cancer undergoing radical prostatectomy and extended pelvic lymphadenectomy". *BJU international* 107.2, pp. 220–225 (cit. on p. 13).

Heidenreich, Axel et al. (2014a). "EAU guidelines on prostate cancer. Part 1: screening, diagnosis, and local treatment with curative intent—update 2013". *European urology* 65.1, pp. 124–137 (cit. on p. 13).

Heidenreich, Axel et al. (2014b). "EAU Guidelines on Prostate Cancer. Part II: Treatment of Advanced, Relapsing, and Castration-Resistant Prostate Cancer". *European Urology* 65.2, pp. 467–479 (cit. on p. 13).

Hissoiny, Sami et al. (2011). "GPUMCD: A new GPU-oriented Monte Carlo dose calculation platform". *Medical physics* 38.2, pp. 754–764 (cit. on p. 32).

Hu, Yipeng et al. (2008). "Modelling prostate gland motion for image-guided interventions". *International Symposium on Biomedical Simulation*. Springer, pp. 79–88 (cit. on p. 85).

INCF (2016). *Epidémiologie des cancers - Les chiffres du cancer en France | Institut National Du Cancer*. URL: http://www.e-cancer.fr/Professionnels-de-sante/Les-chiffres-du-cancer-en-France/Epidemiologie-des-cancers (visited on 11/30/2016) (cit. on p. 10).

Jan, S. et al. (2011). "GATE V6: a major enhancement of the GATE simulation platform enabling modelling of CT and radiotherapy". *Physics in medicine and biology* 56.4, p. 881 (cit. on p. 33).

Jia, Xun et al. (2011). "GPU-based fast Monte Carlo simulation for radiotherapy dose calculation". *Physics in medicine and biology* 56.22, p. 7017 (cit. on p. 32).

Kirov, Assen S. and Jeffrey F. Williamson (2001). "Monte Carlo-aided dosimetry of the Source Tech Medical Model STM1251 I-125 interstitial brachytherapy source". *Medical physics* 28.5, pp. 764–772 (cit. on pp. 34, 103).

Klotz, Laurence et al. (2008). "The efficacy and safety of degarelix: a 12-month, comparative, randomized, open-label, parallel-group phase III study in patients with prostate cancer". *BJU international* 102.11, pp. 1531–1538 (cit. on p. 13).

Klotz, Laurence et al. (2010). "Clinical results of long-term follow-up of a large, active surveillance cohort with localized prostate cancer". *Journal of Clinical Oncology: Official Journal of the American Society of Clinical Oncology* 28.1, pp. 126–131 (cit. on p. 13).

Kovács, György and Peter Hoskin (2013). *Interstitial Prostate Brachytherapy: LDR-PDR-HDR*. Springer Science & Business Media (cit. on pp. 17, 18).

Kumar, Rukmini et al. (2004). "The dynamics of acute inflammation". *Journal of theoretical biology* 230.2, pp. 145–155 (cit. on p. 67).

Kumar, Vinay, Abul K. Abbas, and Jon C. Aster (2013). *Robbins basic pathology*. Elsevier Health Sciences (cit. on pp. 67, 68).

Lahanas, Michael, Eduard Schreibmann, and Dimos Baltas (2003). "Multiobjective inverse planning for intensity modulated radiotherapy with constraint-free gradient-based optimization algorithms". *Physics in Medicine and Biology* 48.17, p. 2843 (cit. on pp. 35, 47).

Lahanas, Michael et al. (2004). "Inverse planning in brachytherapy: Radium to high dose rate 192 iridium afterloading". *Nowotwory Journal of Oncology* 54.6, pp. 547–554 (cit. on p. 22).

Lamé, Gabriel (1866). *Leçons sur la théorie mathématique de l'elasticité des corps solides par G. Lamé*. Gauthier-Villars (cit. on p. 76).

Leclerc, Ghyslain et al. (2006). "Prostatic edema in I125 permanent prostate implants: Dynamical dosimetry taking volume changes into account". *Medical physics* 33.3, pp. 574–583 (cit. on pp. 66, 108).

Lee, Huai-Ping, Ming C. Lin, and Mark Foskey (2008). "Physically-based validation of deformable medical image registration". *International Conference on Medical Image Computing and Computer-Assisted Intervention*. Springer, pp. 830–838 (cit. on p. 85).

Lee, J. Joy et al. (2015). "Biologic differences between peripheral and transition zone prostate cancer". *The Prostate* 75.2, pp. 183–190 (cit. on p. 9).

Lemaréchal, Yannick et al. (2015). "GGEMS-Brachy: GPU GEant4-based Monte Carlo simulation for brachytherapy applications". *Physics in medicine and biology* 60.13, p. 4987 (cit. on pp. 35, 38).

Lessard, Etienne and Jean Pouliot (2001). "Inverse planning anatomy-based dose optimization for HDR-brachytherapy of the prostate using fast simulated annealing algorithm and dedicated objective function". *Medical physics* 28.5, pp. 773–779 (cit. on p. 30).

Li, Chunhui et al. (2014). "Quantitative elasticity measurement of urinary bladder wall using laser-induced surface acoustic waves". *Biomedical optics express* 5.12, pp. 4313–4328 (cit. on p. 85).

Lippuner, Jonas and Idris A. Elbakri (2011). "A GPU implementation of EGSnrc's Monte Carlo photon transport for imaging applications". *Physics in medicine and biology* 56.22, p. 7145 (cit. on p. 32).

Luke, Hans D. (1999). "The origins of the sampling theorem". *IEEE Communications Magazine* 37.4, pp. 106–108 (cit. on p. 24).

Maas, S. et al. (2011). "FEBio theory manual". *Musculoskeletal Research Laboratories, University of Utah, Salt Lake City, UT* (cit. on pp. 77, 83).

Maas, Steve A. et al. (2012). "FEBio: finite elements for biomechanics". *Journal of biomechanical engineering* 134.1, p. 011005 (cit. on p. 83).

Martin, André-Guy et al. (2007). "Permanent prostate implant using high activity seeds and inverse planning with fast simulated annealing algorithm: A 12-year Canadian experience". *International Journal of Radiation Oncology* Biology* Physics* 67.2, pp. 334–341 (cit. on p. 30).

Masko, Elizabeth M., Emma H. Allott, and Stephen J. Freedland (2013). "The relationship between nutrition and prostate cancer: is more always better?" *European urology* 63.5, pp. 810–820 (cit. on p. 10).

McNeal, John E. (1981). "The zonal anatomy of the prostate". *The Prostate* 2.1, pp. 35–49 (cit. on p. 8).

Meigooni, Ali S. (1995). "Dosimetry of interstitial brachytherapy sources: Recommendations of the AAPM Radiation Therapy Committee Task Group No. 43". *Medical physics* 22.2, p. 2 (cit. on p. 19).

Monajemi, T. T., Charles M. Clements, and Ron S. Sloboda (2011). "Dose calculation for permanent prostate implants incorporating spatially anisotropic linearly time-resolving edema". *Medical physics* 38.4, pp. 2289–2298 (cit. on p. 22).

Mottet, Nicolas et al. (2016). "EAU–ESTRO–SIOG Guidelines on Prostate Cancer. Part 1: Screening, Diagnosis, and Local Treatment with Curative Intent". *European Urology* (cit. on p. 11).

Mow, V. C. (1984). "An analysis of the unconfined compression of articular cartilage". *Journal of biomechanical engineering* 106, p. 165 (cit. on p. 76).

Mow, Van C., Mark H. Holmes, and W. Michael Lai (1984). "Fluid transport and mechanical properties of articular cartilage: a review". *Journal of biomechanics* 17.5, pp. 377–394 (cit. on p. 84).

Mow, Van C. et al. (1989). "Biphasic indentation of articular cartilage—II. A numerical algorithm and an experimental study". *Journal of biomechanics* 22.8, pp. 853–861 (cit. on p. 76).

Mow, VanC and V. Roth (1981). "Effects of nonlinear strain-dependent permeability and rate of compression on the stress behavior of articular cartilage". *Journal of biomechanical engineering* 103, p. 61 (cit. on p. 76).

Möbius, August Ferdinand (1827). *Der barycentrische calcul* (cit. on p. 96).

Nath, Ravinder et al. (2009). "AAPM recommendations on dose prescription and reporting methods for permanent interstitial brachytherapy for prostate cancer: Report of Task Group 137". *Medical physics* 36.11, pp. 5310–5322 (cit. on pp. 16, 46, 49, 50).

Nathan, Carl F. (1987). "Secretory products of macrophages." *Journal of Clinical Investigation* 79.2, p. 319 (cit. on p. 69).

Nickolls, John and William J. Dally (2010). "The GPU computing era". *IEEE micro* 30.2 (cit. on p. 32).

Novins, Kevin L., Francois X. Sillion, and Donald P. Greenberg (1990). "An efficient method for volume rendering using perspective projection". *ACM SIGGRAPH Computer Graphics*. Vol. 24. ACM, pp. 95–102 (cit. on p. 94).

Oh, William K. et al. (2003). "Biology of Prostate Cancer" (cit. on p. 9).

Ohori, Makoto, Thomas M. Wheeler, and Peter T. Scardino (1994). "The new American joint committee on cancer and international union against cancer TNM classification of prostate cancer". *Cancer* 74.1, pp. 104–114 (cit. on p. 12).

Oldham, M. and S. Webb (1995). "The optimization and inherent limitations of 3D conformal radiotherapy treatment plans of the prostate". *The British journal of radiology* 68.812, pp. 882–893 (cit. on pp. 35, 47).

Oliveira, Susana Maria et al. (2014). "Dosimetric effect of tissue heterogeneity for 125 I prostate implants". *Reports of Practical Oncology & Radiotherapy* 19.6, pp. 392–398 (cit. on p. 39).

Owens, John (2007). "GPU architecture overview." *SIGGRAPH Courses*, p. 2 (cit. on p. 94).

Peach, M. Sean, Daniel M. Trifiletti, and Bruce Libby (2016). "Systematic review of focal prostate brachytherapy and the future implementation of image-guided prostate HDR brachytherapy using MR-ultrasound fusion". *Prostate cancer* 2016 (cit. on p. 18).

Peppa, V. et al. (2016). "Dosimetric and radiobiological comparison of TG-43 and Monte Carlo calculations in 192 Ir breast brachytherapy applications". *Physica Medica* 32.10, pp. 1245–1251 (cit. on p. 58).

Petrylak, Daniel P. (1999). "Chemotherapy for advanced hormone refractory prostate cancer". *Urology* 54.6, pp. 30–35 (cit. on p. 14).

Pineda, Juan (1988). "A parallel algorithm for polygon rasterization". *ACM SIGGRAPH Computer Graphics*. Vol. 22. ACM, pp. 17–20 (cit. on p. 94).

Pouliot, Jean et al. (1996). "Optimization of permanent 125 I prostate implants using fast simulated annealing". *International Journal of Radiation Oncology* Biology* Physics* 36.3, pp. 711–720 (cit. on pp. 23, 24, 30, 31, 35, 36, 47, 59).

Rice, John R. (1985). "The Aspect Ratio Significant for Finite Element Problems" (cit. on p. 80).

Rivard, Mark J. et al. (2004). "Update of AAPM Task Group No. 43 Report: A revised AAPM protocol for brachytherapy dose calculations". *Medical physics* 31.3, pp. 633–674 (cit. on pp. 19, 103).

Rivard, Mark J. et al. (2007). "Supplement to the 2004 update of the AAPM Task Group No. 43 Report". *Medical physics* 34.6, pp. 2187–2205 (cit. on p. 19).

Rowbottom, Carl Graham, Christopher Martin Nutting, and Steve Webb (2001). "Beam-orientation optimization of intensity-modulated radiotherapy: clinical application to parotid gland tumours". *Radiotherapy and Oncology* 59.2, pp. 169–177 (cit. on pp. 35, 47).

Salembier, Carl et al. (2007). "Tumour and target volumes in permanent prostate brachytherapy: a supplement to the ESTRO/EAU/EORTC recommendations on prostate brachytherapy". *Radiotherapy and Oncology* 83.1, pp. 3–10 (cit. on p. 50).

Sarrut, David et al. (2014). "A review of the use and potential of the GATE Monte Carlo simulation code for radiation therapy and dosimetry applications". *Medical physics* 41.6 (cit. on p. 33).

Scallan, Joshua, Virginia H. Huxley, and Ronald J. Korthuis (2010). "Capillary fluid exchange: regulation, functions, and pathology". *Colloquium Lectures on Integrated Systems Physiology-From Molecules to Function*. Vol. 2. Morgan & Claypool Publishers, pp. 1–94 (cit. on p. 71).

Schroder, Fritz H. et al. (2009). "Screening and prostate-cancer mortality in a randomized European study". *New England Journal of Medicine* 360.13, pp. 1320–1328 (cit. on p. 11).

Shacter, Emily and Sigmund A. Weitzman (2002). "Chronic inflammation and cancer." *Oncology (Williston Park, NY)* 16.2, pp. 217–26 (cit. on p. 69).

Shaffer, R. et al. (2009). "Volumetric modulated Arc therapy and conventional intensity-modulated radiotherapy for simultaneous maximal intraprostatic boost: a planning comparison study". *Clinical oncology* 21.5, pp. 401–407 (cit. on p. 14).

Sharifi, Nima, James L. Gulley, and William L. Dahut (2005). "Androgen deprivation therapy for prostate cancer". *Jama* 294.2, pp. 238–244 (cit. on p. 13).

Si, Hang and A. TetGen (2006). "A quality tetrahedral mesh generator and three-dimensional delaunay triangulator". *Weierstrass Institute for Applied Analysis and Stochastic, Berlin, Germany* (cit. on p. 81).

Sinnatamby, Mourougan et al. (2015). "Dosimetric comparison of AcurosTM BV with AAPM TG43 dose calculation formalism in breast interstitial high-dose-rate brachytherapy with the use of metal catheters". *Journal of contemporary brachytherapy* 7.4, pp. 273–279 (cit. on p. 58).

Skowronek, Janusz (2013). "Low-dose-rate or high-dose-rate brachytherapy in treatment of prostate cancer–between options". *Journal of contemporary brachytherapy* 5.1, p. 33 (cit. on p. 18).

Sloboda, Ron et al. (2009). "Time course of prostatic edema post permanent seed implant determined by magnetic resonance imaging". *Brachytherapy* 8.2, p. 126 (cit. on pp. 22, 86, 90).

Sloboda, Ron S. (1992). "Optimization of brachytherapy dose distributions by simulated annealing". *Medical physics* 19.4, pp. 955–964 (cit. on p. 23).

Sloboda, Ron S., Robert G. Pearcey, and Sandra J. Gillan (1993). "Optimized low dose rate pellet configurations for intravaginal brachytherapy". *International Journal of Radiation Oncology* Biology* Physics* 26.3, pp. 499–511 (cit. on p. 23).

Sloboda, Ron S. et al. (2012). "Impact of edema and seed movement on the dosimetry of prostate seed implants". *Journal of medical physics/Association of Medical Physicists of India* 37.2, p. 81 (cit. on pp. 22, 66, 90).

Speight, Joycelyn L. et al. (2000). "Prostate volume change after radioactive seed implantation: Possible benefit of improved dose volume histogram with perioperative steroid". *International Journal of Radiation Oncology* Biology* Physics* 48.5, pp. 1461–1467 (cit. on p. 21).

Spirou, Spiridon V. and Chen-Shou Chui (1998). "A gradient inverse planning algorithm with dose-volume constraints". *Medical Physics* 25.3, pp. 321–333 (cit. on p. 60).

Starling, Ernest H. (1896). "On the absorption of fluids from the connective tissue spaces". *Classic Papers in Critical Care* 19, p. 303 (cit. on p. 71).

Tannock, Ian F. et al. (2004). "Docetaxel plus prednisone or mitoxantrone plus prednisone for advanced prostate cancer". *New England Journal of Medicine* 351.15, pp. 1502–1512 (cit. on p. 14).

Taussky, Daniel et al. (2005a). "Sequential evaluation of prostate edema after permanent seed prostate brachytherapy using CT-MRI fusion". *International Journal of Radiation Oncology* Biology* Physics* 62.4, pp. 974–980 (cit. on p. 21).

— (2005b). "Sequential evaluation of prostate edema after permanent seed prostate brachytherapy using CT-MRI fusion". *International Journal of Radiation Oncology* Biology* Physics* 62.4, pp. 974–980 (cit. on p. 66).

Taylor, Randle EP (2006). "Monte Carlo calculations for brachytherapy". PhD thesis. Institute of Physics (cit. on p. 20).

Tejwani, Ajay et al. (2012). "Case series analysis of post-brachytherapy prostate edema and its relevance to post-implant dosimetry. Post-implant prostate edema and dosimetry". *Journal of contemporary brachytherapy* 4.2, p. 75 (cit. on pp. 21, 66, 87, 88, 104).

Tombal, Bertrand et al. (2010). "Additional analysis of the secondary end point of biochemical recurrence rate in a phase 3 trial (CS21) comparing degarelix 80mg versus leuprolide in prostate cancer patients segmented by baseline characteristics". *European urology* 57.5, pp. 836–842 (cit. on p. 13).

Truesdell, Clifford and Richard Toupin (1960). "The classical field theories". *Principles of Classical Mechanics and Field Theory/Prinzipien der Klassischen Mechanik und Feldtheorie*. Springer, pp. 226–858 (cit. on p. 76).

Valentin, Jack (2002). "Basic anatomical and physiological data for use in radiological protection: reference values: ICRP Publication 89". *Annals of the ICRP* 32.3, pp. 1–277 (cit. on p. 39).

Van De Graaff, Kent Marshall (1995). *Human anatomy*. Wm. C. Brown (cit. on p. 8).

Vandenbroucke, Emily et al. (2008). "Regulation of endothelial junctional permeability". *Annals of the New York Academy of Sciences* 1123.1, pp. 134–145 (cit. on p. 69).

Vasconcelos, J. A. et al. (2001). "Improvements in genetic algorithms". *IEEE Transactions on magnetics* 37.5, pp. 3414–3417 (cit. on p. 24).

Verhaegen, Frank and Slobodan Devic (2005). "Sensitivity study for CT image use in Monte Carlo treatment planning". *Physics in medicine and biology* 50.5, p. 937 (cit. on p. 21).

Verhaegen, Frank and Jan Seuntjens (2003). "Monte Carlo modelling of external radiotherapy photon beams". *Physics in medicine and biology* 48.21, R107 (cit. on p. 32).

Villeneuve, Maxime et al. (2008). "Relationship between isotope half-life and prostatic edema for optimal prostate dose coverage in permanent seed implants". *Medical physics* 35.5, pp. 1970–1977 (cit. on p. 66).

Wang, Yi et al. (2016). "Patient-specific Deformation Modelling via Elastography: Application to Image-guided Prostate Interventions". *Scientific reports* 6 (cit. on p. 84).

Waterman, Frank M. et al. (1997). "Effect of edema on the post-implant dosimetry of an I-125 prostate implant: A case study". *International Journal of Radiation Oncology* Biology* Physics* 38.2, pp. 335–339 (cit. on pp. 66, 87).

Waterman, Frank M. et al. (1998). "Edema associated with I-125 or Pd-103 prostate brachytherapy and its impact on post-implant dosimetry: an analysis based on serial CT acquisition". *International Journal of Radiation Oncology* Biology* Physics* 41.5, pp. 1069–1077 (cit. on pp. 21, 66, 87, 90).

Webb, S. (1991). "Optimization by simulated annealing of three-dimensional conformal treatment planning for radiation fields defined by a multileaf collimator". *Physics in medicine and biology* 36.9, p. 1201 (cit. on p. 30).

White, D. R. et al. (1989). "Tissue substitutes in radiation dosimetry and measurement". *ICRU Report* 44 (cit. on p. 20).

Whittington, Richard et al. (1999). "The effect of androgen deprivation on the early changes in prostate volume following transperineal ultrasound guided interstitial therapy for localized carcinoma of the prostate". *International Journal of Radiation Oncology* Biology* Physics* 44.5, pp. 1107–1110 (cit. on p. 21).

Williamson, Jeffrey F. (1987). "Monte Carlo evaluation of kerma at a point for photon transport problems". *Medical physics* 14.4, pp. 567–576 (cit. on p. 34).

Williamson, Jeffrey F. et al. (2006). "On two-parameter models of photon cross sections: application to dual-energy CT imaging". *Medical physics* 33.11, pp. 4115–4129 (cit. on p. 21).

Woodard, H. Q. and D. R. White (1986). "The composition of body tissues". *The British journal of radiology* 59.708, pp. 1209–1218 (cit. on pp. 21, 38).

Xu, Y. et al. (2015). "SU-E-T-401: Evaluation of TG-43 Dose Calculation Accuracy for SAVI-Based Accelerated Partial Breast Irradiation (APBI) Via Monte Carlo Simulations". *Medical physics* 42.6, pp. 3426–3426 (cit. on p. 58).

Yamada, Yoshiya et al. (2003a). "Impact of intraoperative edema during transperineal permanent prostate brachytherapy on computer-optimized and preimplant planning techniques." *American journal of clinical oncology* 26.5, e130–e135 (cit. on p. 21).

— (2003b). "Impact of intraoperative edema during transperineal permanent prostate brachytherapy on computer-optimized and preimplant planning techniques." *American journal of clinical oncology* 26.5, e130–e135 (cit. on p. 66).

Yan, Zhennan et al. (2012). "Modulus reconstruction from prostate ultrasound images using finite element modeling". *SPIE Medical Imaging*. International Society for Optics and Photonics, pp. 832016–832016 (cit. on p. 85).

Yang, Guozhen et al. (1998). "A new genetic algorithm technique in optimization of permanent 125I prostate implants". *Medical Physics* 25.12, pp. 2308–2315 (cit. on pp. 24, 30).

Yu, Yan and M. C. Schell (1996). "A genetic algorithm for the optimization of prostate implants". *Medical Physics* 23.12, pp. 2085–2091 (cit. on p. 24).

Yu, Yan et al. (1999). "Automated treatment planning engine for prostate seed implant brachytherapy". *International Journal of Radiation Oncology* Biology* Physics* 43.3, pp. 647–652 (cit. on p. 24).

Zhou, Chuanyu and Feyzi Inanc (2002). "Integral-transport-based deterministic brachytherapy dose calculations". *Physics in medicine and biology* 48.1, p. 73 (cit. on p. 20).

INDEX

GGEMS library, 33
STM1251 seed model, 34

Active surveillance, 12
Acute inflammation, 68
Androgen deprivation therapy, 13
Anterior fibromuscular stroma, 9

Barycentric interpolation, 96
Biphasic mixture theory, 76

Central zone, 9
Chemotherapy, 13
Chronic inflammation, 69
Continuum body configuration, 73
Continuum mechanics, 72

Edema effect on dosimetry, 66
Edema evolution modeling, 83
Elastic body deformations, 74
External beam radiotherapy, 14

Finite elements method, 78

High-dose-rate (HDR) brachytherapy, 17
Homeostasis, 67

Inflammation, 67
Intensity-modulated radiotherapy, 14

LDR brachytherapy limitations, 18
Low-dose-rate (LDR) brachytherapy, 15

Male pelvic region mesh, 82
Mechanical parameters & constraints, 84
Mesh generation, 79
Model validation, 86
Modeling techniques, 77

Neighbor tissues modeling, 84

Patient database, 81
Peripheral zone, 9
Proposed model development, 81
Prostate mechanical parameters effect on edema, 88
Prostate modeling, 83

Radical prostatectomy, 13
Rasterization, 94
Rigid body deformations, 73

Starling equation, 70

TG-43 dose calculation formalism, 19
TNM staging system, 11
Transition zone, 8
Transperineal brachytherapy, 15

Underlying inflammation mechanism, 67

Volumetric Modulated Radiotherapy, 14

ACRONYMS

^{103}**Pd** palladium-103.

^{103}**Rh** Rhodium-103.

^{125}**I** iodine-125.

^{125}**Te** tellurium-125.

^{192}**Ir** iridium-192.

v Poisson's ratio.

3D-CRT three-dimensional conformal radiotherapy.

AcI acute inflammation.

ADT androgen deprivation therapy.

AJCC American Joint Committee on Cancer.

AS active surveillance.

BC boundary condition.

BPH benign prostatic hyperplasia.

ChI chronic inflammation.

CT computed tomography.

DVH dose-volume histogram.

EBRT external beam radiotherapy.

FE finite elements.

FSA fast simulated annealing.

GA genetic algorithm.

GBBS grid-based Boltzmann equation solvers.

GPU graphical process unit.

GS modified Gleason score.

HDR high-dose-rate.

HU Hounsfield unit.

IMRT intensity-modulated radiotherapy.

ISUP International Society of Urological Pathology.

LDR low-dose-rate.

LHRH luteinising hormone-releasing hormone.

MBDCA model-based dose calculation.

MC Monte Carlo.

MC-ITPA MC-based inverse treatment planning algorithm.

OAR organ at risk.

PCa prostate cancer.

PDE partial differential equation.

PSA prostate-specific antigen.

PTV planning target volume.

RP radical prostatectomy.

SA simulated annealing.

TG-186 AAPM Task Group No. 186.

TG-43 AAPM Task Group No. 43.

TRUS transrectal ultrasound.

US ultrasound.

VMAT volumetric modulated arc therapy.

VMR volumetric model resampling.

YM Young modulus.